UNIVERSITY OF CALIFORNIA

Los Angeles

Propagation Phasor Approach in Holographic Image Reconstruction

A dissertation submitted in partial satisfaction of the requirements for the degree Doctor of Philosophy in Electrical Engineering

by

Wei Luo

2016

ABSTRACT OF THE DISSERTATION

Propagation Phasor Approach in Holographic

Image Reconstruction

by

Wei Luo

Doctor of Philosophy in Electrical Engineering

University of California, Los Angeles, 2016

Professor Aydogan Ozcan, Chair

High-resolution and wide-field imaging is of great value for various scientific disciplines; such tasks demand the imaging modalities to possess large space-bandwidth products. The rapid evolutions of modern image sensor technologies and computing power have provided tremendous opportunities for development of new imaging systems with significantly larger space-bandwidth products than conventional lens-based systems. This dissertation introduces the latest advance in lensfree holographic microscopy, a computational imaging technique that serves as a potent solution for high-resolution, wide-field microscopy. By placing the specimen at a close proximity to the image sensor (e.g., ~100 μm - 1 mm), lensfree microscopy runs at unit magnification and possesses significantly larger field-of-view (FOV) than conventional lens-

based systems. There are two major challenges in lensfree holographic microscopy: (1) undersampling by the image sensor; and (2) phase retrieval of the light field. This work first shows that, by using the two-dimensional pixel function of an image sensor-array as an input to lensfree holographic image reconstruction, pixel super-resolution can improve the numerical aperture (NA) of the reconstructed image by a factor of ~3 compared to a raw lensfree image. This pixel super-resolution-based lensfree microscope, when combined with an ultra-violet (UV) light emitting diode (LED), is capable of resolving 225 nm line-width gratings and is useful for wide-field on-chip imaging of nano-scale objects such as helical multi-walled carbon nanotubes. To further increase the bandwidth of this imaging modality, I developed lensfree imaging using synthetic aperture (LISA), which delivers an effective numerical aperture of ~1.4 across a wide FOV of ~20 mm^2. LISA utilizes multiple angles of illumination to holographically synthesize the largest numerical aperture for an on-chip microscope and enables color imaging of tissue samples, including pathology slides, using complex wave retrieval.

In the pursuit of more efficient pixel super-resolution techniques, I developed a fundamentally new resolution enhancement technique, namely wavelength scanning pixel super-resolution. It relies on an iterative algorithm to generate high-resolution reconstructions of the specimen using undersampled diffraction patterns recorded at a few wavelengths, covering a narrow spectrum (~10-30 nm). When combined with synthetic aperture technique, this wavelength scanning super-resolution approach can achieve a resolution of ~250 nm, corresponding to a numerical aperture of ~1.0 across a wide field-of-view (>20 mm^2). Compared to lateral displacement-based super-resolution, wavelength scanning brings uniform resolution improvement in all directions across the sensor array and requires significantly less number of measurements.

The development of wavelength scanning pixel super-resolution eventually led to a new computational framework, termed as propagation phasor approach, which for the first-time combines pixel super-resolution and phase retrieval techniques into a unified mathematical framework. In contrast to previous holographic reconstruction algorithms, my new algorithm reduces the number of raw measurements by five to seven folds, while at the same time achieving a competitive resolution across a large field-of-view. These technological advances could greatly benefit the development of high-resolution, wide-field computational imaging modalities with compactness, cost-effectiveness and superior data efficiency.

The dissertation of Wei Luo is approved.

Oscar M. Stafsudd

Dino Di Carlo

Aydogan Ozcan, Committee Chair

University of California, Los Angeles

2016

Table of Contents

Acknowledgements

I would like to express my sincere gratitude to Prof. Aydogan Ozcan, for his tremendous support and guidance he has provided throughout my research and life at UCLA. It has been a true blessing to work under a brilliant scholar with his dedication to innovation and excellence. Prof. Ozcan's insights into research and his great enthusiasm has always inspired me. With no doubt, the years I spent at Ozcan Research Group have been the most productive time in my life. I sincerely thank my doctoral committee members, Prof. Dino Di Carlo, Prof. Benjamin Williams, and Prof. Oscar Stafsudd for kindly taking part in my thesis committee and their support during my research.

I would like to thank my comrades at Ozcan Lab: Alon Greenbaum, Zoltán Göröcs, Qingshan Wei, Euan McLeod, Derek Tseng, Onur Mudanyali, Serhan O. Isikman, Mustafa Uğur Daloğlu, Ting-Wei Su, Bahar Khademhosseini, Ikbal Sencan, Hatice C. Koydemir, Shouyu Wang, Alborz Feizi, Yibo Zhang, Ping-Luen Chung, Steve Feng, Jose C. Contreras-Naranjo, Aniruddha Ray, Yair Rivenson. The support I have received and friendship I made at Ozcan Lab will remain forever memorable.

Last but not least, I would like to thank my family for giving me the opportunity to follow my dreams and their unconditional support. Your love always has been everything and always will be everything.

Vita

Wei Luo received his BS and MS degrees in Electrical Engineering (EE) from Tsinghua University, China. In 2011 he joined Professor Aydogan Ozcan's Bio-Nanophotonics Lab in Electrical Engineering Department at UCLA to pursue his PhD degree. His research focuses on high-resolution, wide-field holographic microscopes. Wei Luo has received fellowships including the Chancellor's Award at UCLA and SPIE Optics and Photonics Education Scholarship. During his research at UCLA, Wei has authored or co-authored more than 35 peer reviewed research articles in major journals and conferences.

Selected Publications

1 Luo W, Zhang Y, Zoltan G, Feizi A, Ozcan A. Propagation phasor approach for holographic image reconstruction. Sci Rep 2016. Accepted.

2 Luo W, Greenbaum A, Zhang Y, Ozcan A. Synthetic aperture-based on-chip microscopy. Light Sci Appl 2015; 4: e261.

3 Luo W, Zhang Y, Feizi A, Gorocs Z, Greenbaum A, Ozcan A. Pixel super-resolution using wavelength scanning. Light Sci Appl 2015. doi:10.1038/lsa.2016.60.

4 Greenbaum A, Luo W, Su T-W, Göröcs Z, Xue L, Isikman SO et al. Imaging without lenses: achievements and remaining challenges of wide-field on-chip microscopy. Nat Methods 2012; 9: 889–895.

5 Mudanyali O, McLeod E, Luo W, Greenbaum A, Coskun AF, Hennequin Y et al. Wide-field optical detection of nanoparticles using on-chip microscopy and self-assembled nanolenses. Nat Photonics 2013; 7: 254–254.

6 Luo W, Shabbir F, Gong C, Gulec C, Pigeon J, Shaw J et al. High throughput on-chip analysis of high-energy charged particle tracks using lensfree imaging. Appl Phys Lett 2015; 106: 151107.

Chapter 1 Introduction to lensfree holographic imaging

Parts of this chapter have previously been published in A. Greenbaum, W. Luo, TW Su, Z. Göröcs, L. Xue, S. O Isikman, A. F Coskun, O. Mudanyali & A. Ozcan. Imaging without lenses: achievements and remaining challenges of wide-field on-chip microscopy. *Nat Meth* **9,** 889–895 (2012).

Lensfree on-chip imaging refers to using a digital opto-electronic sensor-array, such as a CCD or CMOS imaging chip to directly sample the light transmitted through a specimen without the use of any lenses between the object and the sensor planes[1–25]. Such an imaging geometry is significantly simpler in hardware and much more compact and lightweight than conventional lens-based microscopes. In addition, this geometry, as will be detailed later on, can decouple imaging field-of-view (FOV) and resolution from each other, creating unique microscopes where improved resolution and field-of-view can be achieved at the same time with new sensor chips that are being introduced in consumer electronics products, in particular cellphones and high-end digital camera. This feature might place lensfree on-chip microscopes on a performance curve that *qualitatively* follows the Moore's Law, a trend that is new in optical microscopy.

For a lensfree on-chip microscope there are various design choices that one can select from. In general we can categorize lensfree microscopes into two main streams: (1) contact mode shadow imaging based microscopes[22–25]; and (2) holographic microscopes[1–21]. The first group of lensfree microscopes aims to minimize the distance between the sample and the active region of the detector-array (or an aperture array in some cases[22,23]) so that diffraction can be minimized. Therefore these contact mode lensfree microscopes sample the shadow of objects and treat these shadows as object images under the assumption that optical diffraction within the object body

and between the object and sensor planes can be ignored, where the latter cannot typically get lower than ~0.9-1 μm (since the active region of a pixel is buried under its surface)[24,25]. On the other hand, the second category of lensfree microscopes relies on digital holography to partially undo the effects of optical diffraction that occur between the object and the detector planes, i.e., unlike contact imaging approaches a sizeable distance between the objects and sensor chip can be accommodated. In this second group of lensfree microscopes, the scattered light from each object interferes with the unscattered background light to create an in-line holographic 'shadow'[12], which is then digitally processed to reconstruct an image of the object[5].

There are various holographic imaging and processing techniques that have been used so far in lensfree microscopy context, some of which use a spatially and temporally coherent light source such as a laser that is filtered by a small pinhole (e.g., ≤1-2μm)[1–4], while some others rely on partially-coherent illumination provided by e.g., light-emitting-diodes (LEDs)[5–18,26]. In this Perspective, we will focus on the latter and present the unique features of such partially-coherent lensfree microscopy tools (see Figure 1) that operate under unit fringe magnification and report some of the emerging results that they provide for wide-field imaging needs, achieving e.g., a numerical aperture (NA) of ~0.8 across 20-30 mm^2, or an NA of ~0.1 across ~18 cm^2, corresponding to a space-bandwidth product of ≥1 Billion. We will also present some of the current challenges that these computational on-chip microscopes face, and compare different approaches to shed more light on their future directions and applications.

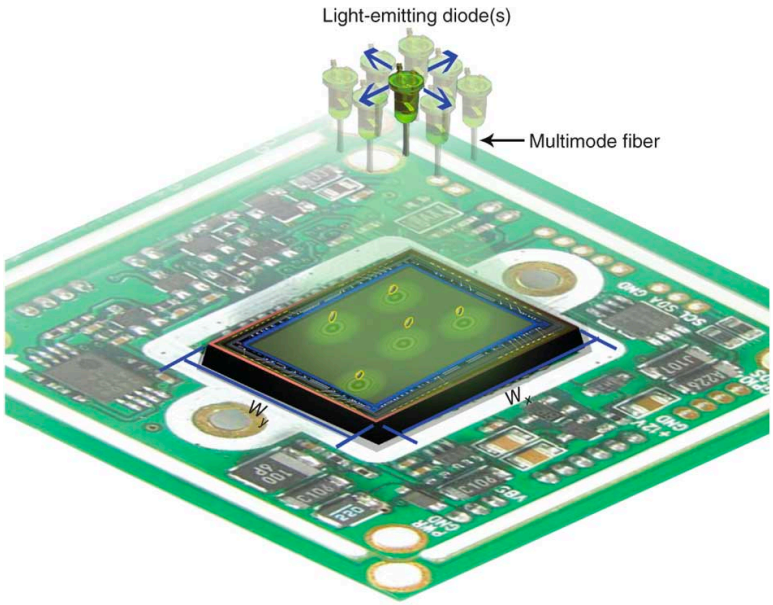

Figure 1.1. Schematic diagram of a partially coherent lens-free transmission microscope that operates under unit magnification, such that the active area of the imager chip (for example, a CCD or CMOS sensor array) is the same as the object FOV.

1.1 Key components of a lensfree holographic on-chip microscope

In a partially-coherent holographic on-chip microscope (Fig. 1) the source can simply be an LED or an array of LEDs. In case wavelength tunability is desired a monochromator can also be used that is coupled to e.g., a multi-mode fiber. The spectral bandwidth of the source can vary between a few nanometers to e.g., 20-30 nm depending on the resolution requirement of the system. Because the sample plane is rather close to the detector plane (e.g., $\leq$ 1-2 mm), significantly reduced temporal coherence lengths of such broadband sources (compared to a laser) do not constitute a problem since the scattered light rays and the background light can still interfere at the sensor-chip.

In addition to temporal coherence requirements, spatial coherence of the illumination is also critical in lensfree holographic microscopy. Under unit fringe magnification, since holographic

shadows of objects do not spread across the entire sensor active area, the spatial coherence diameter that is required at the sampling plane is also significantly smaller[6]. This implies that an LED can simply be butt-coupled without the use of any mechanical alignment stage or light-coupling optics to a large-core fiber-optic cable or a simple pinhole (e.g., 50-100 μm in diameter). This makes alignment and operation of a partially-coherent lensfree holographic microscope rather straight-forward. Since coherence is now used as a gating function, this choice of partial-coherence, besides simplicity of alignment and cost-effectiveness, also helps us reduce speckle and multiple reflection interference noise terms as well as cross-interference among objects' diffraction patterns, which is in general a source of artifact for holography[27].

Apart from the illumination end, the other key component involved in a lensfree holographic microscope is the optoelectronic sensor array that is used to sample the transmitted light pattern from each specimen. Under unit magnification, the imaging FOV of a lensfree microscope equals to the active area of the sensor chip, which implies that using state-of-the-art CCD and CMOS chips, one can achieve a wide range of FOVs varying between e.g., 0.2 cm^2 to >15 cm^2. These numbers constitute significantly wider imaging areas compared to standard objective-lenses employed in conventional optical microscopes.

In addition to the FOV or active area of the sensor chip, another key feature is the pixel size, which directly influences the spatial resolution that can be achieved. Whether or not holographic or contact mode lensfree imaging is used, a smaller pixel size will in general help us achieve better resolution, unless the pixel design exhibits severe angular distortions that create aberrations for oblique rays, corresponding to high numerical apertures. Since the area of the pixel shrinks with the square of its size, to claim the same active area or imaging FOV, more megapixels would also be needed for an ideal lensfree on-chip microscope, which fortunately is

already a major trend in consumer electronics mostly driven by the massive volume of camera-phones, which are now claiming ~40 megapixel imagers[28].

1.2 Reconstruction techniques

For lensfree imaging in general there are two important reconstruction blocks that are needed to visualize an object's image. The first one of these computational blocks, termed "pixel super-resolution" is used to partially remove the under-sampling related limitations due the pixel size and is required to achieve sub-pixel spatial resolution on a chip[7–9]. Contact mode and holographic lensfree on-chip microscopes share this common step to digitally embed more pixels to an image by e.g., shifting the light source and capturing multiple lensfree images of the same static object[7,8]. Alternatively, the motion of the object within e.g., micro-fluidic devices can also be used for the same pixel super-resolution step to resolve finer features of an object[9,16,25].

The second reconstruction block, which follows the "pixel super-resolution" step, is only required for holographic lensfree microscopy, where there is a considerable distance between the objects and the detector array, such that optical diffraction cannot be ignored. In this second computation step, the image of the specimen is reconstructed from its super-resolved holographic shadow by employing e.g., iterative phase reconstruction[29] or twin-image elimination algorithms[30] that are commonly used in holography literature. As a result of this step, both amplitude and phase images of the object are generated, where the latter might be especially important to image weakly scattering transparent specimen like sub-micron bacteria or parasites.[8] .

In addition to these, lensfree holographic on-chip microscopy can also employ additional computational tools to move from 2D cross-sectional images to a lensfree tomogram of the object by e.g., merging the spatial frequency information of different illumination angles[16–18].

We should note that such computational blocks are not needed for a conventional lens-based microscope, which can provide immediate visualization of specimen through e.g., the eye-piece. While this can be considered an important limitation of computational microscopy tools in certain settings, the recent advances in micro-processors such as graphics processing units (GPUs) that are now appearing even on our cellphones[31] make computation extremely cost-effective and widely accessible globally, which we believe would be a key factor for lensfree imaging techniques to scale up.

1.3 Gigapixel imaging using lensfree on-chip microscopes

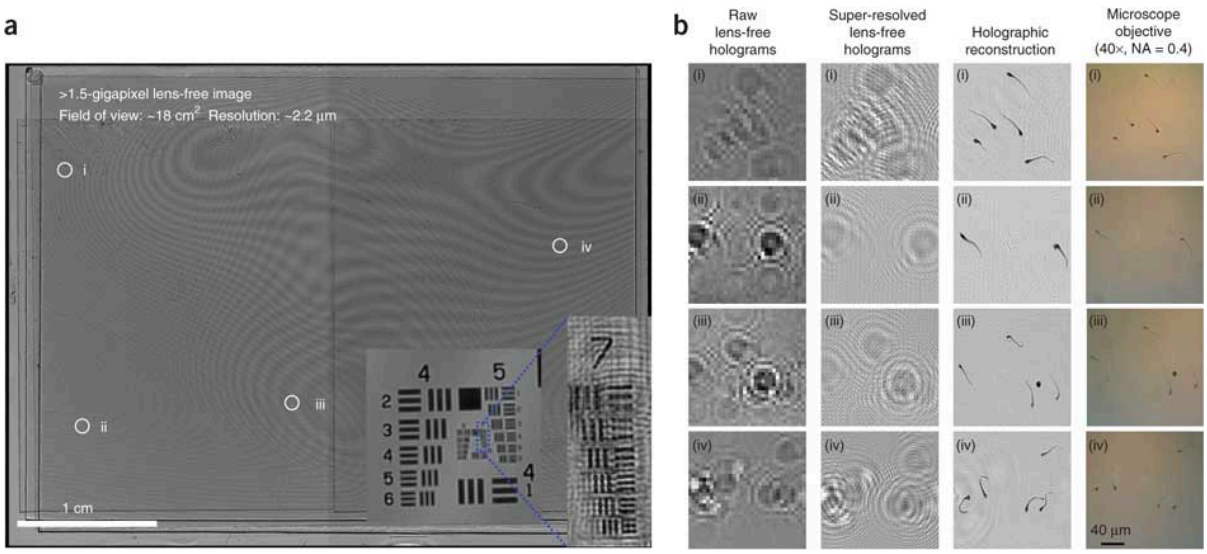

Figure 1.2. (**a**) A super-resolved lens-free image obtained by a partially coherent holographic on-chip imaging platform with a FOV of ~18 cm^2 (~4.9 cm × 3.7 cm) and >1.5 billion pixels. The inset images show a lens-free hologram and its reconstruction results for a resolution target (USAF 1951 test chart) to demonstrate a half-pitch resolution of ~2.19 µm corresponding to an NA of ~0.1. (**b**) Four selected areas of interest (corresponding to the circles and roman numerals in **a**shown at higher magnification. The first column shows raw lens-free holograms of human sperm (immobilized on a glass slide[9]). Because the physical pixel size of this monochrome CCD chip is 6.8 µm, severe under-sampling of holograms is observed. The second column shows the pixel super-resolved lens-free holograms for the same regions, which are digitally synthesized by combining 36 (6 × 6) subpixel-shifted raw lens-

free holograms. The third column illustrates the reconstruction results for these pixel super-resolved lens-free holograms. The fourth column shows the same region imaged with a conventional microscope.

After going over some of the basic features of lensfree on-chip microscopes in general, next we would like to give examples of their state-of-the-art performance. Lensfree computational microscopy permits imaging at extreme space-bandwidth products in excess of e.g., 1 Billion. Using for instance a state-of-the-art CCD enables imaging an ultra-wide FOV of ~18 cm^2 with a spatial resolution of ~2.2 μm, which constitutes a space-bandwidth product of ~1.5 Billion (see Figure 2). In this case, the CCD chip itself has ~40 megapixels, where each pixel is physically ~6 μm wide. However, by employing pixel super-resolution, a deeply sub-pixel resolution corresponding to a numerical aperture of ~0.1 can be achieved across the entire active area of the CCD chip (i.e., an FOV of 18 cm^2). In comparison, conventional objective-lenses with a similar numerical aperture would typically have a few mm^2 FOV. While mechanical scanning of the sample or the objective-lens could be used to widen the imaging area, it would be a complicated and costly solution to achieve such a wide imaging area of e.g., ~18 cm^2.[32]

On the other extreme, using a state-of-the-art CMOS chip, instead of a CCD, enables achieving ~350 nm resolution (illumination wavelength: 530 nm) across a field-of-view of ~20-30 mm^2 in both phase and amplitude images (see Fig. 1.3). In this case, the CMOS chip is a 16 megapixel color RGB sensor with a pixel size of ~1.1 μm that is manufactured to be used in e.g., cellphone cameras. Once again, using pixel super-resolution (only for the green pixels) enables achieving deeply sub-pixel resolution, corresponding to a numerical aperture of ~0.75 across the entire active area of the CMOS sensor chip (i.e., FOV >20 mm^2).

One of the most unique aspects of lensfree computational imaging is the fact that these quoted numbers will immediately improve as new sensor arrays become available. This rapid

advancement in sensor array technologies is driven mostly by the cellphone and digital camera industries, which manufacture more than 1 Billion new camera modules each year, placing lensfree on-chip microscopy on a sweet spot to follow a rapid trend that is qualitatively similar to the Moore's Law in terms of its performance.

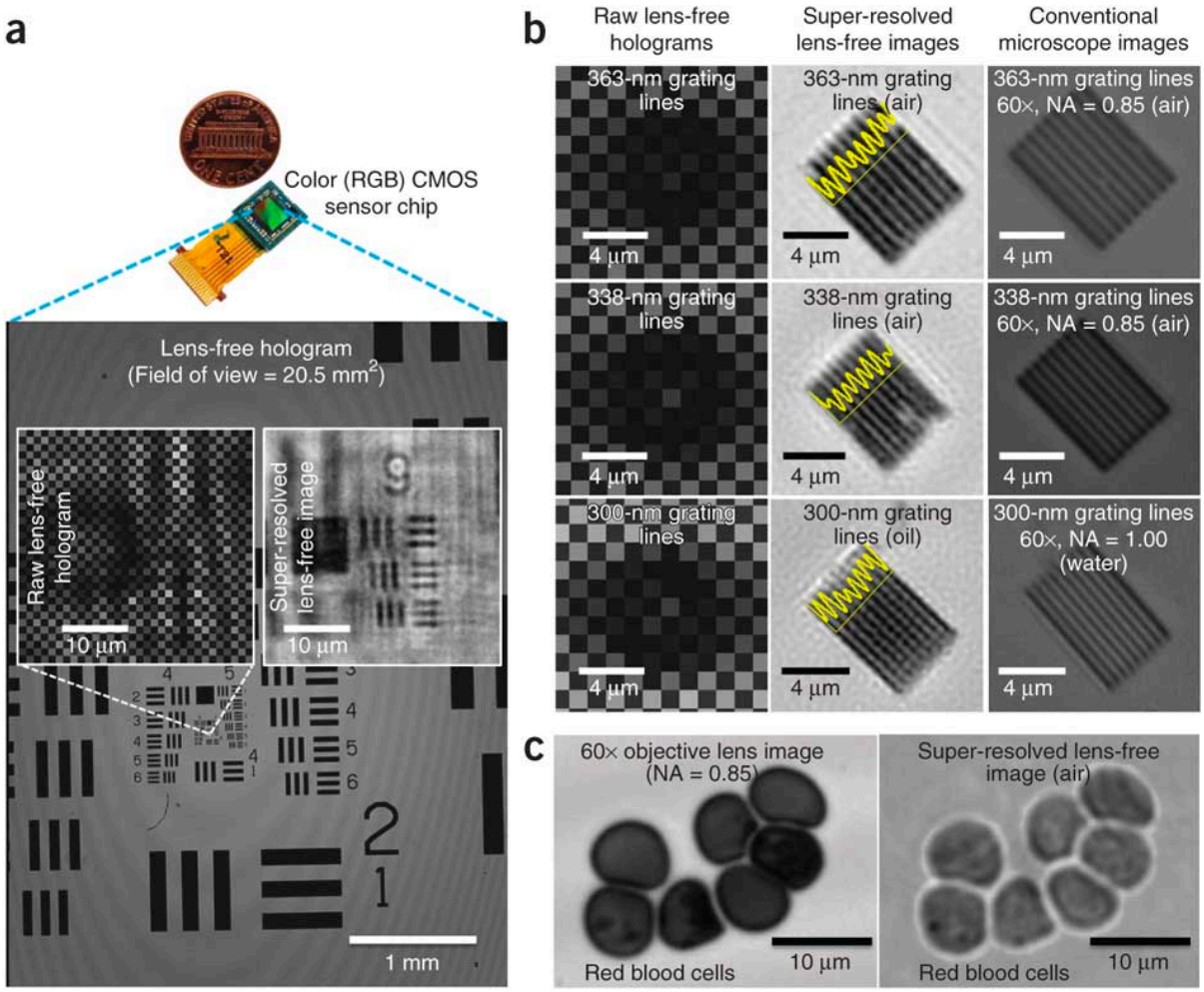

Figure 1.3. (**a**–**c**) Pixel super-resolved lens-free holographic images of a USAF 1951 test chart (**a**), custom-fabricated gratings (milled onto a glass substrate using a focused ion beam system) (**b**) and human red blood cells (**c**) are summarized and compared against conventional high-NA objective lenses. Panel **b** illustrates that this lens-free imaging platform achieves an NA of ~0.8 (in air) together with a half-pitch resolution of <350 nm over a FOV of ~20.5 mm^2. Using oil immersion between the sample and the sensor array, a half-pitch resolution of ~300 nm is also demonstrated in **b**, corresponding to an effective NA of ~0.9 (illumination wavelength, 530 nm). The raw lens-free

holograms in **a** and **b** exhibit the Bayer pattern of the color CMOS sensor, only the green pixels of which were used in our image reconstructions. We used up to 100 (10 × 10) subpixel-shifted raw lens-free holograms in these pixel super-resolution results.

Equally important is that the imaging geometry of Figure 1 decouples spatial resolution from imaging field-of-view. Stated differently, as more megapixels are introduced onto the same chip, while keeping the pixel size the same (*or even smaller*), we can achieve a larger FOV without sacrificing resolution (*or keep the same FOV with improved resolution*). Therefore, the current trend in digital electronics toward smaller pixel size and larger megapixel imager chips will continue to improve the resolution and field-of-view of such lensfree computational microscopes providing us a unique on-chip microscopy platform, where the resolution and FOV are not necessarily tied to each other.

1.4 Future challenges and opportunities for lensfree on-chip microscopes

Resolving micro-scale features of specimen in both space and time, lensfree on-chip microscopes could impact almost all the fields that their conventional lens-based counterparts are used, including imaging[6–8], screening and tracking of cells and other micro-organisms for various applications ranging from high-throughput screening methods to lab-on-a-chip technologies[13,14,24]. Next, we will discuss some of the key challenges that remain for improving the performance and scaling the applications areas of lensfree on-chip microscopes.

Spatial Resolution: Despite their large imaging areas, the state-of-the-art resolution for lensfree on-chip microscopy is still not diffraction limited. Improving the numerical aperture from its current level of e.g., ~0.8 to 1 or even higher (using e.g., liquid immersion) would necessitate new sensor chips that have sub-micron pixel sizes. While this seems to be on the horizon with especially next-generation CMOS imager chips, an important factor that is less

demanding for main-stream use of sensor arrays (e.g., in digital cameras) is angular distortion of pixels. At high numerical apertures, the pixels of a sensor array would typically exhibit artifacts since oblique light rays would experience much higher losses (as a function of e.g., angle) and more importantly could end up generating a signal in neighboring pixels, which would distort the accurate sampling of lensfree transmission patterns. Therefore, special attention has to be given to the design of lensfree imager chips in terms of their angular response, which is not as critical for cellphone camera applications due to the presence and the lower NA of the imaging lens. To reduce pixel related imaging aberrations and get closer to the diffraction limit, new sensor chips that have sub-micron pixel size and a decent external quantum efficiency which is not a strong function of illumination angle are needed.

In addition to these, new signal processing approaches that rely on sparse signal recovery and compressive sampling algorithms[19,20,33]are also promising future directions that can be combined with pixel super-resolution schemes to further improve the resolution of lensfree on-chip microscopes.

Sample density: Because lensfree on-chip microscopy is a transmission imaging modality, sample density can cause issues in our imaging performance, for both holographic and contact imaging schemes. For contact shadow imaging, if the density of the specimen increases in 3D, it creates aberrations since the objects will effectively move away from the sensor active area, increasing the contribution of diffraction to shadow images, reducing the resolution and creating aberrations using pixel super-resolution algorithms[24,25]. In case of density increase for planar 2D objects (where thickness of the specimen can be ignored, e.g., $\leq$1 μm), contact imaging would still exhibit aberrations since pixel super-resolution approaches would create artifacts for imaging dense and connected objects covering a large field-of-view due to: (1) inaccurate sub-

pixel shift estimations for local features; and (2) partial interference of dense object shadows with each other, which is a phenomenon that needs to be carefully analyzed in high-resolution shadow imaging even if the coherence diameter at the detector plane is e.g., less than 1-2 μm. Stated differently, contact mode lensfree imaging that uses pixel super-resolution could exhibit artificial sub-micron features under even a very small coherence diameter that is for example an order of magnitude narrower than the spatial coherence provided by the sun on earth.

Similar limitations also apply for holographic lensfree on-chip imaging in the case of dense samples. For in-line holographic imaging geometry, as the density of the samples gets higher the background light (which acts as a reference wave for encoding the phase of the scattered object field into intensity oscillations) gets distorted deviating from a plane wave for each object hologram. One potential solution for this issue is to increase the distance between the sample and the detector chip so that a beam splitter can reflect an unscattered reference beam on the sensor array[34]. This, however, would necessitate the use of increased temporal and spatial coherence for illumination and relatively complicate the set-up in terms of alignment and size. Due to significantly increased distance between the sample and sensor planes, it would also reduce the useable field-of-view especially for large area CCD chips.

Another solution to this object density issue that has been successfully applied to wide-field on-chip holographic imaging is multi-height lensfree imaging, where the sensor array records the lensfree diffraction holograms of the specimen at different heights. By iteratively propagating back and forth between different heights, phase and amplitude images of dense objects can be reconstructed[11,13,35]. The disadvantage of this approach is that more measurements are now required for the same sample, which also requires the use of additional computation to finely align the FOV of each multi-height lensfree hologram to each other.

Reflection imaging: While dense and transparent specimen can potentially be imaged using lensfree on-chip microscopy tools, if the sample is not transparent it cannot be reconstructed using the above discussed approaches. For thick and non-transparent samples, such as tissue slides, reflection imaging would be needed. There are earlier reports on lensfree reflection imaging methods,[21], however, these approaches have relatively smaller FOV and resolution, which is mostly due to significantly increased distance between the specimen and the detector array in reflection imaging geometry. Furthermore, while these reflection imaging approaches are lensfree, they still rely on a beam splitter cube to channel the scattered reflection field onto a sensor array. As the active area of the sensor array gets larger (e.g., >10 cm^2) the size of such a beam splitter would also grow, which would further increase the distance between the specimen and the detector planes, causing signal to noise ratio limitations for sub-micron features of the object. Therefore, unlike its transmission counterpart, lensfree reflection microscopy is less suitable to reach extreme FOVs (>10-20 cm^2) that are enabled by e.g., the state-of-the-art CCD chips.

Fluorescent imaging: Our lensfree imaging discussions so far have been limited to bright-field transmission microscopy on a chip. Fluorescent imaging, however, is another important modality that needs to be merged onto the same lensfree on-chip microscope for various applications that demand e.g., the use of molecular probes to bring specificity and sensitivity to their imaging needs. For this end, there have been some efforts to create dual-mode lensfree microscopes that can switch back and forth between bright-field and fluorescent imaging[36]. However, the resolution and image quality of these existing lensfree fluorescent imaging solutions are not yet as competitive as their bright-field counterparts[33,37,38]. There are several reasons behind this limited performance of lensfree fluorescent imaging. *First*, fluorescent

emission is not directional as a result of which the signal strength drops much faster as a function of vertical distance in a lensfree imaging geometry. This lower signal to noise ratio demands placing the labeled specimens rather close to the sensor chip surface (e.g., <400-500 μm). *Second*, decent filtering of the excitation light on a chip is challenging. Thin-film based standard fluorescent filters would not work as desired in a lensfree configuration since the scattered excitation light would not be collimated unlike conventional lens-based fluorescent microscopes. This requires relatively thicker absorption filters to be used, which would increase the distance between the sample and the detector active area, reducing the achievable resolution. *Third*, fluorescent emission is spatially and temporally incoherent, and therefore holographic digital reconstruction and related pixel super-resolution techniques are not useful in this case. While recently emerging sparse signal recovery techniques (based on e.g., compressive sampling) have been used to decode lensfree fluorescent images[37], their resolution level is still relatively coarse (~3-4 μm)which is due to reduced signal to noise ratio of fluorescent on-chip imaging.

While the issues discussed above are creating technical challenges to achieve sub-micron fluorescent resolution over a large imaging area, which is the characteristic signature of lensfree on-chip imaging, these difficulties are not fundamental in that systematic improvements in detection signal to noise ratio (through e.g., actively cooled sensor chips), absorption filter performance, smarter illumination schemes (involving e.g., the use of structured excitation light) and better incoherent signal recovery algorithms could help us achieve a dual-mode lensfree on-chip microscope that can switch between fluorescent and bright-field imaging across a large FOV. Once combined with color sensor arrays (e.g., RGB CMOS chips) multi-color lensfree fluorescent imaging could also be achieved, which could further expand the application of these on-chip microscopes into fluorescent cytometry.

Imaging speed: Imaging speed of lensfree on-chip microscopes are limited by the frame rate of the sensor array, which varies from ~1 fps to >50 fps depending on the megapixel count of the sensor chip. On the other hand, this frame rate can be significantly increased to e.g., >200-300 fps by digitally selecting a smaller FOV within the active area of the chip. This also implies that high-throughput scanning of large areas at high frame rates can be achieved by digitally moving the region of interest within the chip active area. This could be quite useful for e.g., observing spatio-temporal dynamics of fast moving micro-organisms such as sperms[15], across large sample volumes to collect massive statistics about their behavior.

Regarding imaging speed, one final note is that the surface temperature of the sensor chip can easily go above 40°C at continuous operation, and therefore places an important limitation for especially contact imaging approaches, which might not succeed in cooling the immediate surface of the imager chip despite the use of cooling circuitry or heat sinks. This concern is also true for lensfree holographic approaches, to a lesser degree however, due to increased distance (e.g., 1-2 mm) between the sample and the sensor chip.

Standardization of reconstruction techniques: The landscape of lensfree on-chip microscopes is rather complicated with various designs. What makes this picture even more confusing is that reconstruction methods/algorithms also vary depending on the imaging architecture. An important obstacle for wide-scale use of such emerging computational microscopy tools, especially in biomedical sciences, can be overcome through standardization of reconstruction algorithms in modular blocks that are integrated to each other for handling different possible lensfree imaging configurations.

Chapter 2 Incorporation of pixel function in pixel super-resolution

Parts of this chapter have been previously published in Greenbaum, A. W. Luo, B. Khademhosseinieh, T-W. Su, A.F. Coskun, and A. Ozcan. Increased space-bandwidth product in pixel super-resolved lensfree on-chip microscopy. *Sci. Rep.* **3,** 1717 (2013).

Spatial resolution of lensfree on-chip microscopy is in general limited by the pixel size of the image sensor chip. This limitation can be circumvented by utilizing pixel super-resolution techniques that can synthesize a much smaller effective pixel size, achieving an improved spatial resolution. Here we shed more light into this improvement and report that by using the two-dimensional pixel function of an image sensor-array as an input to lensfree holographic image reconstruction, pixel super-resolution can improve the numerical aperture (NA) of the reconstructed image by a factor of ~3 compared to a raw lensfree image. This improvement factor was confirmed using two different image sensors that significantly vary in their pixel sizes, circuit architectures and digital/optical readout mechanisms. Under unit magnification, using a 40 Mega-pixel monochrome CCD (Charge-Coupled-Device) image sensor chip with a physical pixel size of 6.8 μm, we achieved an NA of ~0.14 across an ultra-large field-of-view (FOV) of ~18 cm^2 yielding a super-resolved effective pixel size of $\lambda/0.56$, where λ is the illumination wavelength. Under the same lensfree on-chip imaging geometry, using a 16.4 Mega-pixel color CMOS (Complementary Metal-Oxide-Semiconductor) image sensor chip that has a physical pixel size of 1.12 μm, we achieved an NA of ~0.83 across a FOV of ~ 20 mm^2, yielding a super-resolved effective pixel size of $\lambda/3.32$. Compared to the original pixel count of each sensor chip, these pixel super-resolved lensfree images demonstrate a pixel count increase of $(3.81\mu m/\lambda)^2$ and $(3.72\mu m/\lambda)^2$, for our CCD and CMOS imagers respectively, which empirically point to roughly

the same space-bandwidth improvement factor regardless of the sensor chip architecture used in our lensfree on-chip imaging set-up. Besides the resolution improvement, such pixel count increase immediately renders our lensfree on-chip microscope into a Giga-pixel throughput imaging platform without sacrifice in FOVs: with the 6.8 μm-pitch CCD sensor we obtained an effective pixel count of up to 2.52 Giga pixels; with the 1.12 μm-pitch CMOS sensor the effective pixel count reached up to 1.64 Giga pixels. We also demonstrate that this pixel super-resolution based lensfree microscope, when combined with an ultra-violet light emitting diode, is capable of resolving 225 nm line-width gratings and is useful for wide-field on-chip imaging of nano-scale objects such as helical multi-walled carbon nanotubes (MWCNTs).

2.1 Introduction

Lensfree imaging is an emerging technique that requires no imaging lens or its equivalent between the specimen and the image sensor planes [2,4,19,39–46]. In its specific 'on-chip' implementation, by placing the sample close (e.g., <1-2 mm) to the active area of an image sensor chip, this technique brings not only extreme compactness to the entire optical system, but also the unique feature of unit fringe magnification, where the object field-of-view (FOV) of the lensfree on-chip imaging platform is equal to the active area of the sensor chip [6,15,47–56]. Therefore, the FOV of a lensfree on-chip microscope can easily reach e.g., ~20-30 mm^2 or ~10-20 cm^2 using a CMOS or a CCD imager, respectively [56–59]. Unlike conventional lens-based microscopy approaches, an increase in FOV does not necessarily sacrifice spatial resolution, and new image sensor chips with larger active areas and smaller pixel sizes immediately translate into a larger FOV as well as a better spatial resolution, without a change in the optical design of the lensfree on-chip microscope [7,8,60].

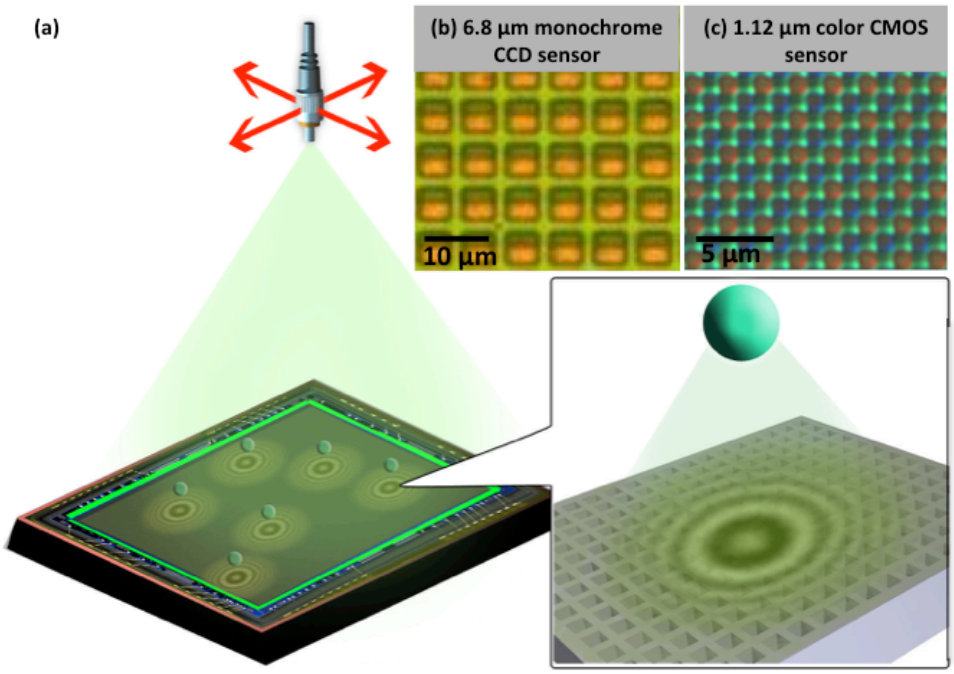

Figure 2.1. Lensfree on-chip microscopy setup. (a) Shows a schematic of the lensfree holographic microscope setup. In this geometry, light coming out from the optical fiber illuminates both the sample and the image sensor. The fiber tip is latterly shifted to perform pixel super-resolution. The close-up of (a) shows that the scattered wave from the object interferes with the unperturbed reference wave and forms a hologram, which is then sampled by the image sensor. The pixel structures exhibits large variability in terms of pixel pitch and morphology as can be seen in (b) and (c). (b) Shows an optical microscope image (20× objective, NA = 0.5) of a 6.8 µm monochrome CCD image sensor chip. (c) Shows an optical microscope image (100× Water immersion objective, NA = 1) of a 1.12 µm color CMOS image sensor chip, the Bayer pattern can be readily seen.

The setup of a lensfree microscope is simple and compact (see e.g., Fig. 2.1.a); a partially coherent and quasi-monochromatic light source (center wavelength, λ) illuminates a specimen that is positioned onto an optoelectronic image sensor-array [56,57,61]. The scattered light transmitted through the specimen interferes with the unperturbed background light and creates an in-line hologram that is sampled and digitized by the image sensor-array (see inset Fig. 2.1.a). Since this on-chip microscope design has unit magnification, when capturing a raw lensfree

hologram, the spatial sampling rate and the sampling function are determined by the sensor's pixel pitch and its two-dimensional (2D) pixel responsivity map within each pixel (which we refer to as the pixel function). Stated differently, it is the pixel function of an opto-electronic sensor-array that fundamentally affects the spatial resolution and image distortions/aberrations in a lensfree holographic on-chip microscope. Different sensor chips have different pixel functions (with various pixel widths/heights and 2D functional forms), and therefore the nature of the spatial under-sampling and convolution operations that occur at the sensor plane is highly dependent on the sensor choice[62].

In this chapter we demonstrate that by incorporating the 2D pixel function of an image sensor chip into lensfree holographic image reconstruction steps (Fig. 2.2), one can improve the numerical aperture (NA) of the reconstructed images by a factor of ~3 compared to a raw lensfree image. This improvement is achieved using pixel super-resolution techniques, and is found to be, by and large, independent of the sensor chip design. Toward this end, we worked with both a monochrome CCD and a color CMOS image sensor chip that had a physical pixel size of e.g., 6.8 μm (Fig. 2.1.b) and 1.12 μm (Fig. 2.1.c), respectively. We used experimental and numerical techniques to estimate the 2D pixel function of each sensor-array, which in general would also be applicable for characterization of other opto-electronic sensors. Based on the information of this 2D pixel function, we experimentally found that in our reconstructed super-resolved images an effective pixel size of $\lambda/0.56$ and $\lambda/3.32$ can be synthesized (assuming two pixels define the minimum feature size) with an effective NA of 0.14 and 0.83, using the same CCD and CMOS sensor arrays, respectively. Compared to the pixel count (i.e., megapixel value) of each native sensor chip, these pixel super-resolved lensfree images demonstrate a pixel density increase of $(3.81\mu m/\lambda)^2$ and $(3.72\mu m/\lambda)^2$, for the CCD and CMOS imagers respectively,

which empirically point to roughly the same space-bandwidth improvement factor regardless of the sensor chip architecture used in our lensfree on-chip imaging set-up. Under unit fringe magnification, the pixel count increase applies for every pixel over the FOV, therefore dramatically increases the throughput of the imaging platform: in practice we have achieved effective pixel count of 2.52 Giga with the 40 Mega-pixel, 6.8 µm-pitch CCD image sensor; we also obtained effective pixel count of 1.64 Giga with the 16.4 Mega-pixel 1.12 µm-pitch CMOS image sensor.

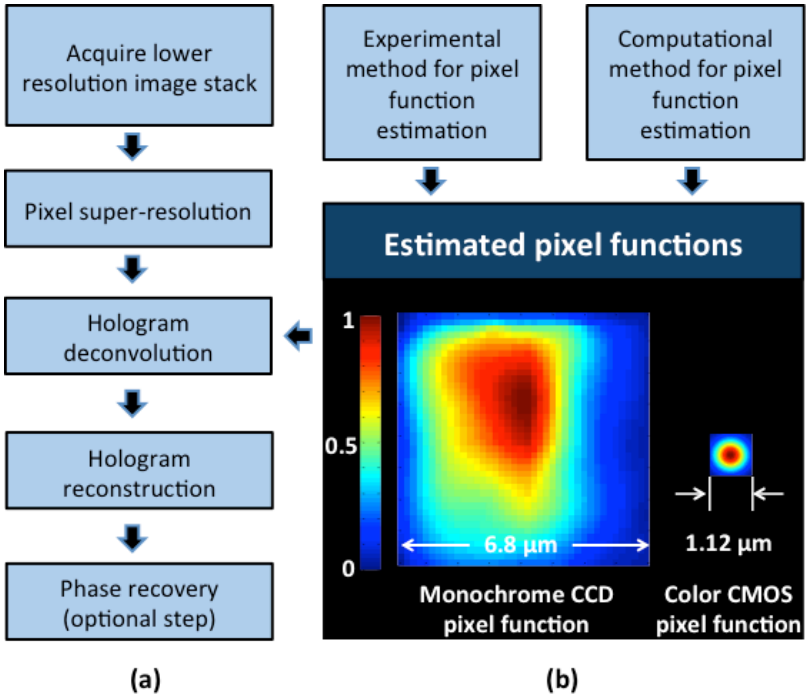

Figure 2.2. Image processing block diagram of lensfree imaging technique. (a) Illustrates the block diagram of the computational methods that are used in producing a high-resolution image. In the hologram deconvolution step, either experimental or computational approach can be used to obtain the pixel function of the image sensor. (b) Shows two pixel function estimations obtained with different methods: the left pixel function obtained with an experimental method for the 6.8 µm monochrome CCD image sensor; and the right pixel function obtained with a computational methods for 1.12 µm color CMOS image sensor. With the estimated pixel function the hologram can be processed with deconvolution algorithms, in which the estimated pixel-function is provided as the blur kernel.

Finally, we also demonstrate that by utilizing a light emitting diode (LED) with a short illumination wavelength (λ = 372 nm), this pixel super-resolution based lensfree on-chip microscope can resolve periodic grating lines with a line-width of 225 nm. To better illustrate the capabilities and the potential applications of this wide FOV high-resolution lensfree microscopy platform we also imaged helical MWCNTs with a diameter of ~160 nm.

2.2 Materials and methods

Experimental setup for measuring the pixel function

The scanning microscope used for CCD pixel function measurement was composed of a bright field microscope in reflection mode (Olympus, BX51), an X-Y-Z piezo stage (PI, 611.3S) and an LED (λ = 470 nm, Mightex, FCS-0470-000) that was butt-coupled to a single mode fiber (ThorLabs, P1-630A-FC2). To create the illumination spot, the eyepiece of the microscope was removed and the fiber end was mounted instead of the eyepiece, while allowing movement of the fiber in only one axis (toward and away from the microscope). In this configuration the image of the fiber is demagnified and projected on the object plane. The demagnification factor used in our setup was 20×, as determined by the objective lens in use. To independently verify the illumination spot size and to focus the spot on the KAF 39MP image sensor, a calibration step was performed. In this step, the focal plane of the projected image of the fiber was calibrated to coincide with the focal plane of the bright field microscope in reflection mode. The calibration was done by placing a reflective metal surface on the microscope stage and focusing the bright field microscope on this reflecting surface. Then, the microscope lamp was turned off, while the LED was turned on, thus creating a spot on the reflective surface. By moving the fiber in the eyepiece toward and away from the microscope, the minimum spot size was found. The fiber is

then fixed to the position that corresponds to the minimum illumination spot size, in order to ensure that the illumination focal plane would coincide with the microscope focal plane. The FWHM of the illumination spot after this calibration step was ~ 1.4 µm as shown in Fig. 3.a.

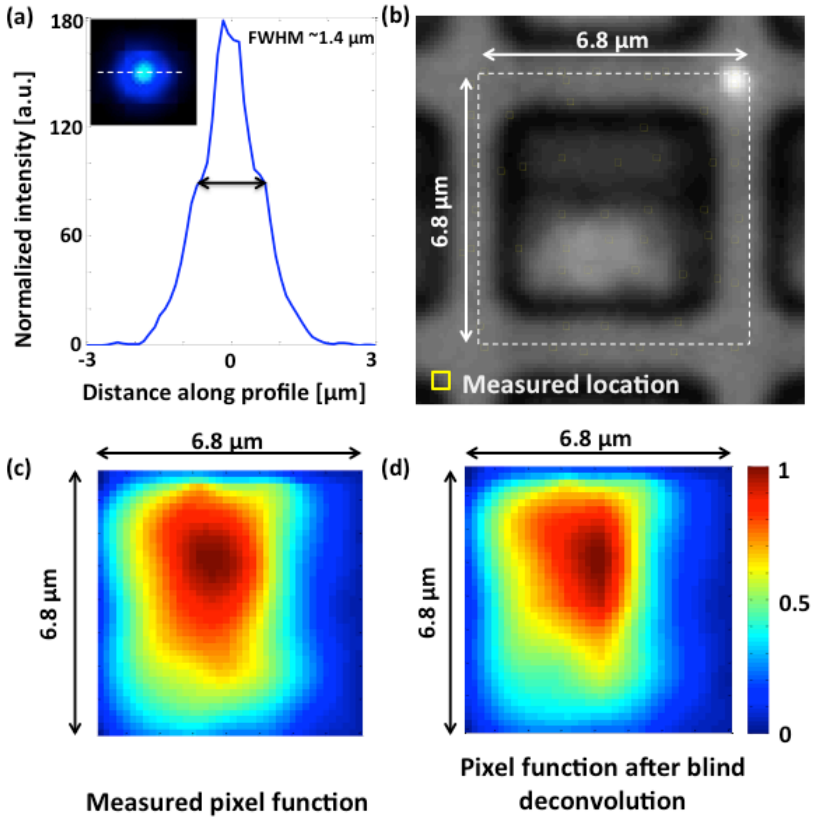

Figure 2.3. Experimental approach for pixel function estimation using a scanning microscope. (a) Shows a cross section of the illumination spot (see inset) of the scanning microscope, which is used to probe the pixel function of the 6.8 µm CCD image sensor. The illumination spot measured FWHM is ~ 1.4 µm in both axis. (b) Shows the illumination spot (the bright spot on the upper right corner) over the CCD image sensor. To estimate the pixel function 54 different locations were probed, each probed location is marked by a yellow hollow rectangle. (c) Shows the measured pixel function after interpolation. (d) Shows the resulting pixel function after the measured pixel function was given as an input to a blind deconvolution algorithm.

Next, the image sensor was placed on the top of the X-Y-Z stage and the X-Y-Z stage was placed on the microscope stage. By turning the LED on and observing the image sensor with the

reflection microscope the spot position could be determined. Fig. 2.3.b shows the reflection microscope image and the illumination spot (bright spot on the upper right corner). To probe a specific location within a single pixel area, the X-Y-Z piezo stage was used to change the relative position of the illumination spot and to correct for focus drifts. After a specific location was selected, the bright field microscope illumination was turned off while the LED (positioned in the eyepiece) was kept on. In this configuration, a narrow spot illuminates only a single pixel while the KAF 39MP image sensor acquires an image. To reduce noise, multiple measurements (~10) were averaged for the same spot location. It should also be noted that to reduce the intensity of the illumination spot and to avoid saturation while capturing the KAF 39MP image, a neutral density filter, which was placed in the filter cube of the microscope, was brought into the illumination path of our set-up.

From raw CCD measurements to pixel function estimation

After probing the area of a single CCD pixel at 54 locations (see Fig. 2.3.b) the pixel function was derived using the following steps. First, the relative position of each measurement was determined by finding the correlation peak between a Gaussian spot and the blue channel image of the microscope image. The blue channel was selected since the illumination spot contrast was higher in comparison to the pixel structure. Second the image was shifted by three pixels to compensate for a systematic bias caused by the positioning of the neutral density filter in the illumination path. Third, the measurements were interpolated to obtain the resulting pixel function shown in Fig. 2.3.c.

To deconvolve the holograms of the test objects with the estimated pixel function we used a built in MATLAB routine deconvblind. This routine implements maximum likelihood estimation

for both the blur kernel (the pixel function in our case) and the unblurred image, by using the expectation-maximization algorithm [63,64]. The measured pixel function (Fig. 2.3c) serves as an initial guess for the algorithm and after 35 iterations the unblurred hologram and the modified pixel function (see Fig. 2.3.d) are provided as outputs.

Computational method for 1.12 µm CMOS sensor pixel function estimation:

As show in Fig. 2.4, based on the assumption that a Gaussian distribution can be used as an estimation of our CMOS pixel function, we optimized the vertical and horizontal FWHM of the distribution and the center position within the pixel area. During the optimization process both FWHMs and center position were numerically scanned, and their corresponding Gaussian distributions were applied in hologram deconvolution step using Wiener deconvolution algorithm [65]. The deconvolved holograms were then back-propagated using an angular spectrum approach to reconstruct the objects [60,66]. By evaluating all the reconstructed images one can find an optimized Gaussian distribution, which can be considered as a close approximation to the actual pixel function.

To evaluate the reconstruction results, two types of known objects were chosen: (1) periodic grating lines fabricated onto a glass substrate using focused ion beam (FIB) milling; and (2) helical MWCNTs (CheapTubes Inc.), which were smeared on a thin glass substrate (~50 µm). During the lensfree imaging process, the vertical distance between the objects and the image sensor were within the range of 50 ~ 150 µm. This gap between the substrate and image sensor planes is filled with a refractive index matching oil to minimize reflection losses and increase NA.

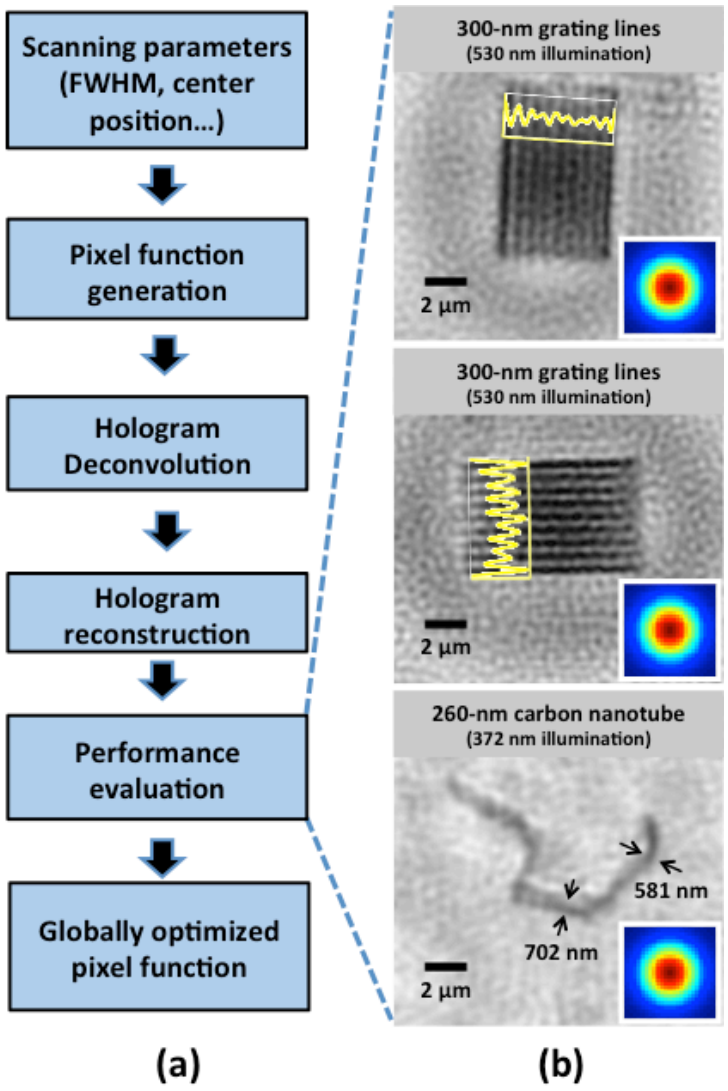

Figure 2.4. Computational approach for 1.12 CMOS pixel function estimation. (a) Shows the block diagram of pixel function estimation using the computational method. (b) Shows the reconstructed images when a globally optimized pixel function is used in hologram deconvolution. Three representative objects are shown : horizontally and vertically oriented grating lines (top and middle), and helical multi-walled carbon nanotube (bottom). The insets show the pixel function estimation of the 1.12 μm CMOS sensor which is a two-dimensional Gaussian distribution centered in a 1.12 μm square and the FWHMs of the distribution in both horizontal and vertical directions are both 550 nm.

Grating lines exhibit a strong signal-to-noise ratio (SNR) at specific spatial frequencies due to their periodic structure. As expected, the reconstruction results of grating lines show a strong

orientation dependency: when the vertically oriented grating lines are imaged, the parameters of horizontal pixel distribution drastically affect the reconstructed image, while parameters of vertical pixel distribution do not exhibit such strong effect on the reconstruction results. Considering this orientation sensitivity, in our lensfree imaging experiments each set of grating lines has been imaged in horizontal and vertical orientations in order to find the optimized pixel parameters in both directions. The reconstructed images are then evaluated by measuring the corresponding modulation depth at the period of the grating lines.

We should also emphasize that the gratings lines are not sufficient for searching the globally optimized pixel parameter space since gratings are inherently limited in terms of their spatial frequency contents, which might lead to locally optimized pixel parameters. To avoid such a bias, besides grating lines with various periods, we also used the helical MWCNTs for pixel function parameter scan. These helical MWCNTs vary in their widths (e.g., ~100-300 nm) and morphologies, and therefore are quite rich in spatial frequency content. To verify our results, same MWCNTs imaged with the lensfree microscope are also imaged with a scanning electron microscope (SEM) to confirm their widths and morphologies. After reconstruction of a lensfree amplitude image, cross-section profiles are taken across the entire imaged MWCNT and the average width of these cross-sections is used for evaluation of the success of reconstruction.

During the search for the pixel function, each individual object has its own 'locally optimized' pixel distribution: for each individual periodic grating, the pixel distribution which leads to the largest modulation depth is considered 'locally optimized'; while for one specific helical MWCNT the pixel distribution which leads to the minimum cross-section width is considered 'locally optimized'. Since the pixel function is independent from the objects, we combine of all the evaluation results of the imaged objects as the cost function and search for a 'globally

optimized' pixel distribution. The pixel distribution which gives maximum overall modulation depth in grating modulation depth and overall minimum MWCNT width is considered as the pixel function.

Implementation of pixel super-resolution in lensfree on-chip holography

Pixel super-resolution is a computational method to overcome undersampling of an image, due to the physical pixel size of the image sensor [8,62,67,68]. Pixel super-resolution aims to generate a high-resolution image from a stack of lower resolution images. Each image in the lower resolution image stack should be of the same object; however, each image should also be translated from the other images in the stack, thus containing new undersampled information about the object of interest. In our experimental setup we used lateral movements of the light source, which was mounted on an X-Y stage (Newport, SMC100PP) in order to achieve sub-pixel shifts of the lensfree holograms on the sensor-chip. The high-resolution lensfree hologram is then synthesized by first digitally estimating the shifts between the acquired lensfree holograms in the stack using an iterative gradient method [62]. After the shifts are calculated, we have chosen a highly efficient non-iterative method to synthesize the high-resolution lensfree hologram (with a much smaller effective pixel size), while preserving the optimality of the reconstruction in maximum-likelihood sense [69]. Pixel super-resolution performs very well with either monochrome or color image sensors (see e.g., Figs. 2.5-2.6); however, for color image sensors minor modifications are required as detailed in [70,71].

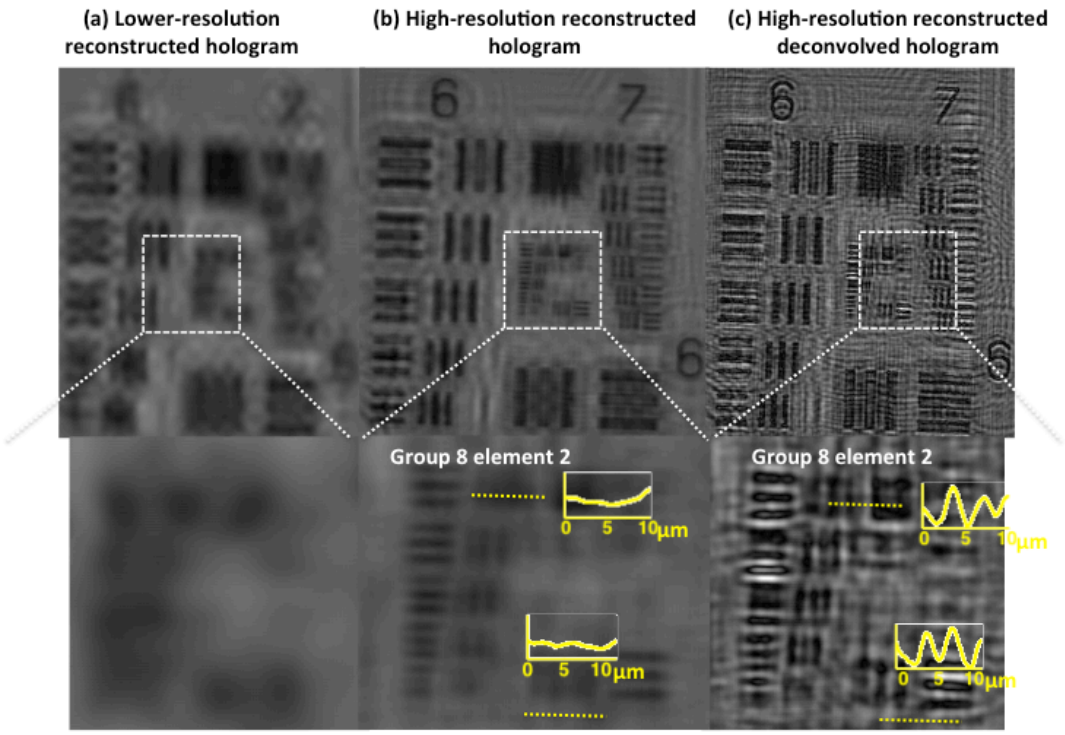

Figure 2.5. Lensfree imaging results obtained with a 6.8 μm CCD image sensor demonstrating an NA of ~ 0.14 with a field-of-view of ~18 cm^2. (a) Shows a lensfree amplitude image, which was reconstructed from a single hologram without using pixel super-resolution (b) Shows a lensfree amplitude image, which was reconstructed from the pixel super-resolved hologram without deconvolution. The horizontal lines of group 8 element 1 and 2 were resolved, while the vertical lines were not resolved as indicated by the cross sections in the image. (c) Shows a lensfree amplitude image, which was reconstructed from the pixel super-resolved hologram with deconvolution. The hologram was deconvolved with the estimated pixel function before the reconstruction step (see Fig. 3.d). The vertical lines in group 8 element 1 and 2 are now resolved as indicated by the cross sections in the image, which corresponds to half pitch resolution of ~1.74 μm and an NA of ~0.14.

Hologram reconstruction and phase recovery

To reconstruct pixel super-resolved lensfree holograms, they are first multiplied by a reference wave, which can be approximated as a plane wave in our current experimental setup[60]. Then, the holograms are back-propagated to the object plane by using the angular

spectrum approach [66]. The resulting back-propagated field is complex and it contains both the phase and amplitude information of the imaged object. The resulting back-propagated field would also contain a noise term commonly referred to as the twin image noise, which is unavoidable in in-line holography geometry. This twin image noise can be mitigated by using an object support based phase-recovery approach; an iterative process that iterates between the object and the hologram planes. In each one of these planes this iterative algorithm enforces a unique constraint [7,60]. In the hologram plane, the enforced constraint is the measured intensity, while in the object plane the enforced constraint suppresses the field to a constant value outside the object support, while keeping the field unchanged in the object support [7,60]. The object support can be evaluated by a simple threshold in the object domain and this phase recovery process typically converges after ~10-15 iterations. Recently, a multi-height lensfree imaging technique has also been demonstrated for on-chip microscopy to entirely eliminate this object support step, which is found especially superior for imaging of dense and connected specimen [72,73].

2.3 Results and discussion

The resolution improvement of lensfree on-chip imaging is achieved by incorporating the estimated pixel functions into the computational procedures that are used in lensfree imaging (see Fig. 2.2.a). In the next sub-sections, we will report estimation of the pixel function of CCD (pixel size: 6.8 μm) and CMOS (pixel size: 1.12 μm) image sensors, using an experimental and a numerical approach, respectively (see Fig. 2.2.b). These pixel functions are then used to deconvolve the high-resolution lensfree holograms to undo distortions and enhance high spatial frequency components that were suppressed. Following this deconvolution step, each lensfree

hologram is reconstructed to retrieve both the phase and the amplitude images of the object (see the Methods Section). We present lensfree imaging results of a resolution test chart (1951 USAF), periodic grating lines and helical MWCNTs to demonstrate the resolution improvement on both of these CCD and CMOS image sensors.

Pixel function estimation of 6.8 μm CCD image sensor

To measure the pixel function of our monochrome CCD image sensor, a scanning microscope was assembled from a bright field microscope, an LED (λ = 470 nm) and an X-Y-Z piezo stage (see the Methods Section). The scanning microscope illumination spot had a full width at half maximum (FWHM) of ~ 1.4 μm in both axes (Fig. 2.3.a), which is much narrower in comparison to the pixel size of the image sensor-array (6.8 μm). This illumination spot allowed a measurement of the pixel function, by probing different positions within the area of a single pixel and recording the pixel response at each position. Fig. 2.3.b shows a microscope image (20× objective lens, NA = 0.5) of a single pixel and the illumination spot (i.e., the bright spot on the upper right corner). Using the pixel output recorded from 54 measured sub-pixel locations (shown in Fig. 2.3.b), an initial estimate of the pixel function of the CCD image sensor was obtained (Fig. 2.3.c, see the Methods Section for details). Since the illumination spot size (~1.4 μm) cannot be treated as a spatial delta function, further refinement of this initial pixel function could be achieved. Toward this end, we deconvolved the lensfree hologram of a known test object (e.g., 1951 USAF resolution test chart) using a blind deconvolution algorithm (built in MATLAB routine deconvblind), which provides maximum likelihood estimation for both the pixel function and the unblurred image [63,74–76]. After 35 iterations of this blind deconvolution

algorithm a refined pixel function was obtained for our CCD image sensor as illustrated in Fig. 2.3.d.

This asymmetrical CCD pixel-function reported in Fig. 2.3.d is in agreement with the literature that reports the architecture of this sensor-array [77,78]. The KAF 39MP CCD image sensor has two gate electrodes for each pixel; one is built using Indium Tin Oxide (ITO), while the other gate electrode is built from doped Polysilicon. ITO is more transparent, and therefore the light collection within the ITO region should be more efficient then in the doped Polysilicon gate electrode [78]. This is also confirmed by the optical microscope image of the pixel (Fig. 2.3.b) which clearly shows its asymmetrical structure: the dark rectangle is the ITO gate electrode and bright rectangle is the doped Polysilicon. Furthermore, the KAF 39MP pixel architecture includes a lateral overflow drain (LOD), which allows off-chip draining of the excessive signal. Accordingly, this LOD region does not collect light; and we believe that its position, which is not visible in the microscope image shown in Fig. 2.3.b, corresponds to the right area of the pixel function that is not sensitive to light.

Pixel function estimation of 1.12 μm CMOS image sensor

It is experimentally challenging to directly measure the pixel function, when the pixel size of image sensor approaches a micrometer scale. Therefore we adopted a computational approach instead, to estimate the pixel function of the 1.12 μm CMOS image sensor (see the Methods Section for details). This computational method generates various pixel functions, and for each pixel function the hologram of a known test object is deconvolved and reconstructed. By evaluating these reconstructed images one can quantify the effect of the estimated pixel function, and the pixel function with the best performance can be treated as an approximation to the real

pixel function. Based on the literature [79] and the image of the lens array installed on this CMOS imager (see Fig. 2.1.c), two assumptions were made on the structure of the pixel function. (1) Similar to the morphology of the microlenses, the pixel function possesses a circular symmetry. (2) The crosstalk between neighbouring pixels is negligible; and therefore the size of the pixel function equals the pixel pitch. Accordingly, we approximated the pixel function of our CMOS sensor-array with a two-dimensional Gaussian distribution within a 1.12 μm square area. Four parameters of the Gaussian pixel function were optimized: the X-Y coordinates of its center position and the FWHM of the Gaussian in both the vertical and the horizontal directions. We scanned the values of these parameters to generate various responsivity distributions within the pixel, and fed each distribution into the hologram deconvolution step (Fig 2.4.a). As shown in Fig. 2.4.b, the objects reconstructed from the deconvolved holograms are evaluated by either measuring the modulation depths (grating lines), or the width of averaged cross-section profiles (helical MWCNTs). We combined all the evaluation results from various objects, and used this combination as the cost function for pixel function optimization. By minimizing this cost function, our estimate of pixel function converged to a Gaussian distribution, which has both a vertical and a horizontal FWHM of ~550 nm as illustrated in Fig. 2.2b.

Lensfree imaging results obtained with 6.8 μm CCD image sensor

Using the CCD sensor-array, we imaged a 1951 USAF resolution test chart to quantify the resolution improvement of our holographic microscope, when pixel super resolution and hologram deconvolution steps are utilized. In these experiments, the illumination wavelength was 480 nm (illumination bandwidth ~4 nm) and the objects were located ~390 μm away from the CCD image sensor. Fig. 2.2.5.a shows the amplitude image of a reconstructed hologram

obtained from only one lensfree hologram measurement i.e., without pixel super resolution. The thinnest resolved grating lines are within Group 6 Element 4, which corresponds to a half-pitch resolution of ~5.52 μm and an NA of ~0.04. After applying only pixel super-resolution, the amplitude image of a reconstructed hologram exhibits a major improvement in resolution (see Fig. 2.5.b). The entire group 7 can now be resolved, which translates to half pitch resolution of ~2.2 μm and an NA of ~0.11. In group 8, the horizontal lines of elements 1 and 2 are also resolved, while the vertical lines cannot be resolved as indicated by yellow cross sections in the same figure. Fig. 2.5.c shows the amplitude image of a reconstructed hologram after applying hologram deconvolution. To deconvolve the image we used 35 iterations of MATLAB built in routine *deconvblind*, using the measured pixel function described earlier as the initial guess [63,75]. The horizontal and vertical lines in group 8 element 1 and 2 are now resolved as indicated by the cross sections in the image, which translates to half pitch resolution of ~1.74 μm and an NA of ~0.14. Overall, after applying pixel-super resolution and hologram deconvolution with the pixel function, the NA of the lensfree holographic microscope improves by a factor of ~3 compared to a single lensfree hologram. Therefore, the effective pixel size is also reduced from λ/0.16 to λ/0.56, yielding an increase in the pixel count by a factor of ~12. Moreover, this resolution improvement does not compromise the FOV, thus with our 6.8 μm 40 Mega-pixel CCD image sensor, the effective pixel count over the entire FOV of 18 cm^2 reaches to 2.52 Giga pixels when 480 nm illumination wavelength is used.

Lensfree imaging results obtained with 1.12 μm CMOS image sensor

Using the 1.12 μm CMOS image sensor, we imaged 225 nm grating lines and a helical MWCNT at an illumination wavelength of 372 nm. With hologram deconvolution based on the

estimated pixel function (Fig. 2.2b), both the grating lines and the helical MWCNT can be clearly resolved as illustrated in Fig. 2.6. At an illumination wavelength of 372 nm, resolving a grating of 225 nm line-width corresponds to an NA of ~0.83, which once again confirms an improvement factor of ~3 compared to a single lensfree holographic image. Therefore, using pixel super-resolution and hologram deconvolution steps on the 1.12 μm CMOS platform, the effective pixel size can be reduced from λ/1.08 to λ/3.32. Such pixel size reduction yields an increase in the effective pixel count by a factor of ~9.4. Thus with a 16.4 Mega-pixel CMOS image sensor we can achieve a pixel count of 1.64 Giga over a FOV of ~20 mm^2 when 372 nm illumination wavelength is used.

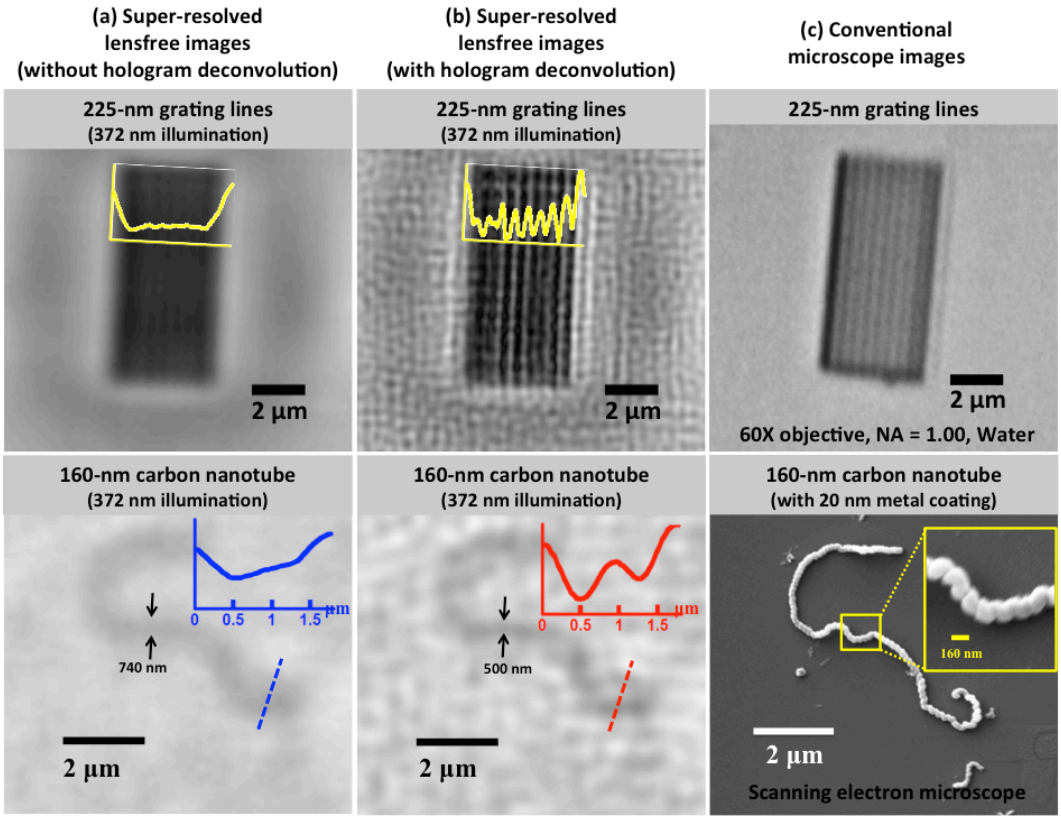

Figure 6. Lensfree imaging results obtained with a 1.12 μm CMOS image sensor demonstrating an NA of ~ 0.83 with a field-of-view of ~20 mm^2. (a) Shows lensfree images reconstructed from high-resolution holograms without deconvolution. (b) Shows lensfree images reconstructed from deconvolved high-resolution holograms. The

holograms were deconvolved with the optimized pixel function before the reconstruction step (see Fig. 2.4.b). (c) Top: a conventional optical microscope image (60× water immersion objective, NA = 1) of the 225 nm line width gratings. Bottom: a SEM image of the helical carbon nanotube. Note that in the SEM image, the 160 nm in diameter helical MWCNT is coated with 20 nm metal coating and thus the observed helical MWCNT diameter is ~ 200 nm.

The image sensor properties play a critical role in lensfree imaging performance, especially for implementing pixel super-resolution. In this work, we shed more light into this affect and reported that by using an estimated 2D pixel function of an image sensor-array as an input to lensfree holographic image reconstruction steps, pixel super-resolution can improve the NA of the reconstructed images by a factor of ~3 compared to a raw lensfree image. We confirmed this improvement factor using two different image sensors that significantly vary in their designs, i.e., a monochrome CCD and a color CMOS image sensor. Using the CCD image sensor-array (pixel size of 6.8 μm), we achieved an NA of ~0.14 across an ultra-large field-of-view (FOV) of ~18 cm^2 yielding a super-resolved effective pixel size of λ/0.56; whereas using the CMOS image sensor-array (pixel size of 1.12 μm), we achieved an NA of ~0.83 across a FOV of ~ 20 mm^2, yielding a super-resolved effective pixel size of λ/3.32. Furthermore, by adopting a short illumination wavelength (λ = 372 nm) a record high spatial resolution for lensfree on-chip imaging is obtained with the same CMOS sensor: a grating with a line width of 225 nm is resolved and a helical MWCNT with a diameter of ~160 nm is successfully imaged.

An interesting observation in these results is a sensor-array independent NA improvement factor of ~3, which is achieved by utilizing pixel super-resolution and hologram deconvolution. Furthermore, compared to the original pixel count of each sensor chip, our pixel super-resolved lensfree images demonstrate a pixel count increase of $(3.81\mu m/\lambda)^2$ and $(3.72\mu m/\lambda)^2$, for our CCD and CMOS imagers respectively, which empirically point to roughly the same space-bandwidth

improvement factor regardless of the sensor chip architecture used in our lensfree on-chip imaging set-up. We believe that a similar level of space-bandwidth improvement could be maintained in lensfree on-chip imaging even if the image sensors differ in their technologies (CMOS vs. CCD), pixel-pitches, detection architectures (e.g., back illuminated vs. front illuminated), and imaging applications (color vs. monochrome).

Finally, we would like to emphasize that in our hologram deconvolution process, higher spatial frequencies that are normally undersampled and suppressed are now boosted; and as a direct consequence of tis, the noise is also amplified. Different deconvolution algorithms might better handle this noise amplification problem, and therefore future research on optimization of deconvolution steps could further improve our results since most of the existing deconvolution codes are optimized for photography applications and not for holography [76].

2.4 Conclusions

The resolution of lensfree holographic microscopes with unit magnification is generally determined by the pixel size of the image sensor. Fortuitously, pixel super-resolution, which is a computational method, can reduce the effective pixel size of the image sensor and consequently improve the spatial resolution of lensfree microscopes. Here we have demonstrated that given a close approximation to the two dimensional pixel-function of the image sensor, pixel super-resolution can improve the NA of the holographic microscope by a factor of ~3, compared to the raw lensfree image. The NA improvement factor was demonstrated using two independent image sensors that varied in their pixel-size, read-out mechanism and circuit architecture. By utilizing a CCD image sensor with a physical pixel size of 6.8 μm we achieved an NA of 0.14 across a FOV that can reach up to 18 cm^2, this result translates to an effective pixel-size of $\lambda/0.56$. Furthermore,

by maintaining the same imaging geometry and utilizing a CMOS image sensor with a physical pixel size of 1.12 μm we achieved an NA of 0.83 across a FOV that can reach up to 20.5 mm^2, this result translates to an effective pixel-size of λ/3.32. The improvement in the pixel count i.e. the area of the physical pixel divided by the area of an effective pixel is $(3.81\mu m/\lambda)^2$ and $(3.72\mu m/\lambda)^2$ for the CCD and CMOS image sensors respectively. Interestingly, this empirical improvement in the space-bandwidth product i.e. pixel count is roughly the same for the two very different image sensors. Thanks to the lensfree on-chip configuration, this improvement benefits the entire FOV, which equals to the area of the image sensor, and thus converting our microscope into a Giga-pixel imaging platform: with a 6.8 μm 40 Mega-pixel CCD sensor one can achieve an effective pixel count of up to 2.52 Giga pixels; while with a 16.4 Mega-pixel CMOS sensor the effective pixel count can reach up to 1.64 Giga pixels. Upon such improvement in resolution, by utilizing a ultra-violet LED (λ = 372 nm) as our illumination source our holographic microscope resolved periodic grating lines with a width of 225 nm and imaged nano-objects like helical MWCNT. This demonstrates a potential application for this large FOV and yet high-resolution lensfree microscope.

Chapter 3 Lensfree imaging using synthetic aperture

This chapter has been previously published in Luo W, Greenbaum A, Zhang Y, Ozcan A. Synthetic aperture-based on-chip microscopy. Light Sci Appl 2015; 4: e261.

3.1 Introduction

Wide field-of-view (FOV) and high-resolution imaging is crucial for various applications in biomedical and physical sciences. Such tasks demand microscopes that have large space-bandwidth products (SBP) with minimal spatial aberrations that distort the utilization of the SBP of the imaging system. Conventional lens-based digital microscopes can achieve high resolution imaging over a large FOV using mechanical scanning stages to capture multiple images from different parts of the specimen that are digitally stitched together. This scanning approach, however, demands a relatively bulky and expensive imaging set-up. In contrast, recent advances in digital components and computational techniques have enabled powerful imaging methods [80,39,81–88], and when these are combined with state-of-the-art image sensor technology, it has made lenses unnecessary in certain microscopic imaging tasks [56,57,89–93]. For example, by taking advantage of image sensor chips with large mega-pixels, small pixel pitch and low cost, lensfree holographic on-chip microscopy provides unique opportunities for achieving ultra-large SBP within a cost-effective and compact imaging design [94–96]. Using source-shifting-based pixel super-resolution techniques [94,97], lensfree on-chip imaging achieves sub-micrometer resolution over a wide FOV of 20-30 mm^2, providing gigapixel throughput with a simple, compact and unit-magnification design [61,98,99]. This computational imaging technique reconstructs not only the amplitude but also the phase information of the specimen, revealing its optical path length distribution. For robust recovery of this phase information, previous lensfree on-chip imaging

approaches adopted a multi-height approach [96,100–103,46], which captures diffraction patterns of the sample at different sample-to-sensor distances. [25–29]

To maintain a high numerical aperture (NA) and improved resolution across the entire visible spectrum, some of the major challenges that on-chip microscopy faces include signal-to-noise ratio (SNR) deterioration and aberrations that affect the high spatial frequencies of the sample. The physical origin of the challenge of detecting high spatial frequencies on a chip is the relatively narrow angular response and large pixel size of opto-electronic image sensor chips. This effect becomes much worse at longer illumination wavelengths because the diffraction angles of a given high spatial frequency band increase with wavelength. Although computational approaches involving pixel super-resolution [94,97] and pixel function estimation or measurement [98] can help to boost some of these spatial frequencies, on-chip microscopy has thus far been limited to an NA of less than ~0.8-0.9 [56,98,104].

Synthetic aperture approaches in optical microscopy [105–119] were originally implemented to overcome the limited space-bandwidth products of traditional objective lens-based imaging designs. Here, we demonstrate the first application of the synthetic aperture technique in lensfree holographic on-chip imaging to reach a record high NA of 1.4 over a large FOV of >20 mm^2, where the sample is sequentially illuminated at various angles using a partially coherent light source (Figure 3.1). In this approach, which we term LISA (lensfree imaging using a synthetic aperture, see Figure 3.2 and the Methods Section), each hologram is recorded using an oblique illumination angle. Therefore, some of the higher spatial frequencies that are normally attenuated or missed by the sensor chip are shifted to lower spatial frequencies where the pixel response is significantly improved (Figure 3.3). This frequency shifting process due to angular diversity in illumination could also enable some of the evanescent waves that would normally never reach

the sensor chip to be converted to travelling waves, permitting the digital synthesis of an NA that is larger than the refractive index of air.

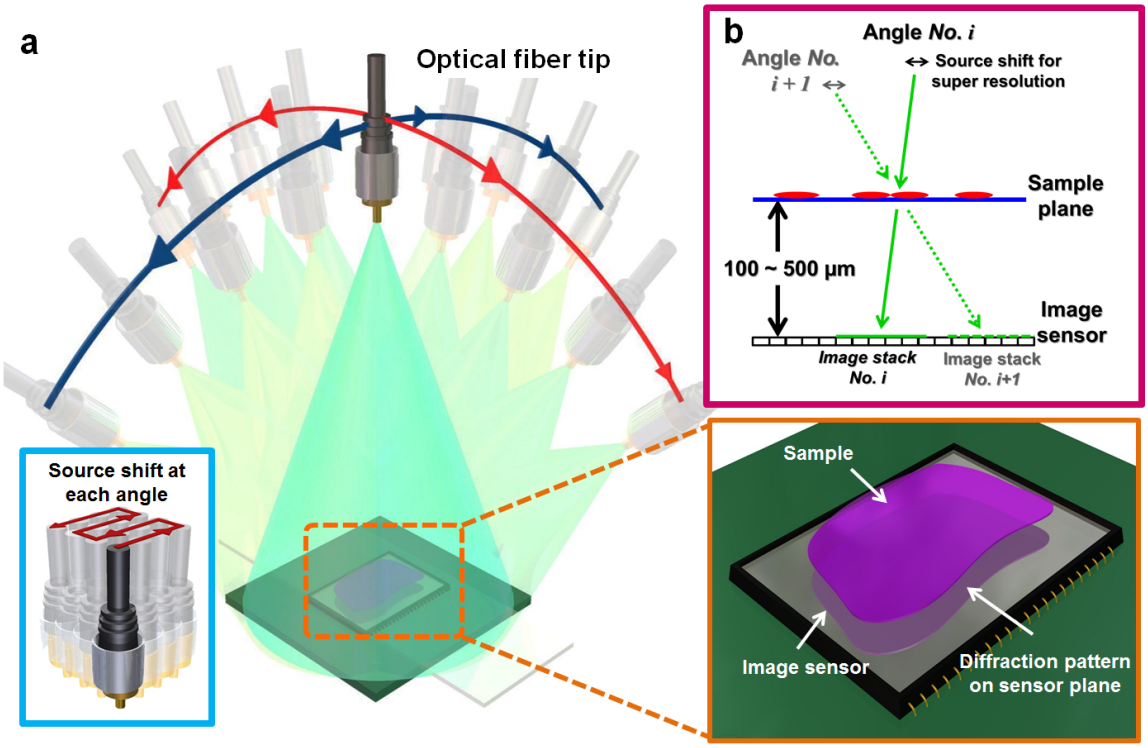

Figure 3.1 Lensfree Imaging using Synthetic Aperture (LISA) experimental setup. (**a**) A partially coherent light source (spectral bandwidth: ~2.5 nm) is coupled to a single mode fiber. This fiber is mounted on a rotational arm to provide tilted illumination across two orthogonal axes (red and blue trajectories). At each angle, the source is laterally shifted multiple times (see bottom left inset) to capture a stack of lower-resolution holographic images. (**b**) The sample is placed onto the image sensor chip at a distance of ~100-500 µm. Both the sample-to-sensor distances and illumination angles are automatically calculated using computational methods, thus eliminating the need for complicated calibration procedures.

In addition to achieving the largest NA reported for on-chip microscopy, combining the information acquired at different illumination angles also significantly improves the overall SNR of the spatial frequency map of the sample, which permits robust phase recovery even for dense and connected samples, such as histopathology slides, without the need for multi-height scanning [46,96,100–103] or any prior information about the specimen/object [60,120]. To demonstrate LISA's

success in complex wave retrieval, we performed lensfree color imaging of breast cancer tissue samples stained with hematoxylin and eosin (H&E) over a very large FOV of 20.5 mm^2 (Figure 3.4 and 3.5), which is equal to the active area of the sensor chip. Furthermore, we achieved high-resolution imaging of unlabeled biological samples, such as unstained Papanicolaou (Pap) smears (Figure 3.6). Such unstained pathology samples do not exhibit sufficient contrast in intensity and are therefore difficult to observe unless phase contrast objective-lenses and special illumination schemes are used. With LISA, however, these unstained samples can be imaged using the reconstructed phase information without a change in either the imaging set-up or the reconstruction algorithm.

Compared to other applications of synthetic aperture techniques in microscopy [105–119], LISA has important advantages in terms of a significantly wider FOV, simplicity, compactness and cost of the imaging set-up and could be quite useful for various biomedical and physical science related applications that demand high-resolution and large FOV microscopic imaging.

3.2 Materials and methods

Experimental setup

In our setup (Figure 3.1), a broadband light source (WhiteLase-Micro from Fianium Ltd, Southampton, United Kingdom) is filtered using an acousto-optic tunable filter (AOTF) and then coupled into a single mode optical fiber to provide partially coherent and tunable illumination of the specimen. The spectral bandwidth of the light coming out of the fiber is approximately 2.5 nm, and the power of the illumination is ~20 μW. The illumination fiber is mounted on a rotational arm whose axis of rotation is aligned within the plane of the image sensor chip (1.12 μm pixel-pitch CMOS color sensor from Sony Corp, Tokyo, Japan). The distance between the fiber end and the image sensor is ~7-11 cm. The rotational arm is installed on a set of linear

stages that provide a lateral light source shift that is used for pixel super-resolution. The CMOS image sensor is also installed on a rotation mount so that the sensor can be rotated within a lateral plane. During the data acquisition process, source shift, angle tilt and image acquisition are all automated and coordinated by custom-written LabVIEW software.

Pixel super-resolution

To digitally mitigate under-sampling artifacts and consequently improve LISA's spatial resolution, pixel super-resolution is implemented. During the lensfree image acquisition at each angle, the light source is shifted laterally by a small amount (e.g., ~ 0.1–0.2 mm), and a raw diffraction pattern is sequentially captured at each light source position. Note that these sub-pixel lateral shifts are negligible compared to the source-to-sample distance (e.g., ~7-11 cm), and therefore, the illumination angle remains approximately constant during the pixel super-resolution data acquisition. These sub-pixel shifts allow us to synthesize a high-resolution in-line hologram for each angle using multiple (typically 16 to 64) lower-resolution in-line holograms [62,69,70,94,97,121]. In the synthesis of the super-resolved holograms, the responsivity distribution within the pixel is also taken into account to compensate for the attenuation of the specimen's high frequency components, as detailed in ref [98]. In a typical lensfree synthetic aperture experiment, images from two orthogonal illumination axes are acquired at 10° increments spanning -50° to +50°.

Autofocus algorithm

An autofocus algorithm is implemented to digitally estimate the sample-to-sensor distance as well as the illumination angle, which will be detailed in the next sub-section. For sample-to-

sensor distance estimation, the super-resolved hologram from the lowest illumination angle is back-propagated to different planes; in each plane, the algorithm evaluates the sharpness of the resulting image, which is defined as the variance of the gradient of the image, calculated using Sobel operators [61,122]. The plane with the highest sharpness is selected as the object plane.

Computational calibration of the illumination angle

In our setup, a rotation arm is used to vary the illumination angle. This rotation arm is inaccurate and can cause up to 4° discrepancies between experiments. However, our iterative synthetic aperture and phase retrieval algorithm requires accurate angle information, as such errors would result in a loss of spatial resolution and phase convergence problems. To this end, we devised a three-step computational method to automatically calibrate the illumination angles. First, the sample-to-sensor distance is evaluated using an autofocus algorithm, as detailed in the previous sub-section. For this purpose, a hologram, which is captured at an approximately normal illumination angle, is utilized. Second, given the calculated sample-to-sensor distance, an "angular autofocus algorithm" is used to accurately find the illumination angle that is associated with one of the measurements. This algorithm receives one super-resolved hologram as input, which is captured with an oblique illumination angle, and an initial guess for the illumination angle based on the rotational arm position. The algorithm then back-propagates the hologram while scanning the illumination angles at 0.1° increments spanning -4° to +4° around the initial illumination angle estimate. The algorithm calculates the edge sharpness for each resulting image, and the angle that corresponds to the maximum sharpness is selected to be the correct illumination angle for this hologram. After finding the absolute illumination angle for one

hologram (i.e., the "anchor" hologram), the rest of the illumination angles can be found by finding the shifts of the rest of the super-resolved holograms relative to the "anchor" hologram.

Iterative synthetic aperture-based phase recovery

The iterative phase recovery process enables the reconstruction of connected and dense specimens by reconstructing the phase of the optical wave. The algorithm receives as input N pixel super-resolved holograms that are synthesized from N different illumination angles and an initial guess of the specimen. This initial guess can be generated by simply back-propagating the hologram at one of the illumination angles using the angular spectrum approach [66]. Alternatively, the initial guess can be generated by summing the back-propagation results from multiple angles and carrying out a four-step iterative process to perform synthetic aperture-based phase retrieval (see Figure 3.2). First, the initial guess, i.e., a complex field representing the specimen, is forward-propagated to the sensor plane. Before the propagation, a phase modulation is applied, which is determined by the illumination angle that is selected. Due to our lensfree and unit magnification configuration, we can simply use a flat-top filter as the forward-propagation aperture. Second, the amplitude of the forward-propagated field is updated using the square root of the diffraction pattern measured at this angle (updated using a weighted average: ~60% of the newly forward-propagated field and ~40% of the measured one). Third, this updated field on the sensor plane is back-propagated to the sample plane, and the phase modulation is removed. Fourth, in the frequency domain, a subregion, i.e., an aperture, is updated (also using a weighted average, as detailed above) using the back-propagated complex field from step three. The center of this aperture is determined by the illumination angle, and the boundary of this aperture is defined as where the signal attenuation is equal to 3 dB. In our setup, 22 angles (e.g., -50° to 50°

at 10° increments along two orthogonal axes) and 5 iteration cycles are typically utilized to achieve phase retrieval. The entire reconstruction algorithm, including pixel super-resolution and synthetic aperture phase retrieval, is implemented using MATLAB on a 3.60 GHz CPU computer (Intel Xeon E5-1620, 16 GB RAM). For a 1 × 1 mm subregion, the reconstruction time is 46 minutes; 21 minutes are required to super-resolve the 22 angles with 64 low-resolution images per angle, while 25 minutes are required to complete 5 iteration cycles of our phase recovery algorithm. During the reconstruction process, neither GPUs nor parallel computing were used. This reconstruction time could be considerably reduced by a factor of ~20 by implementing the algorithm using the *C* language on GPUs [90]; refer to the Discussion Section.

Digital colorization of lensfree on-chip images

Lensfree amplitude images reconstructed at three wavelengths (470 nm, 532 nm and 632 nm) are converted into intensity maps and then combined to form lensfree color (RGB) images of the sample. During this process, histogram equalization is applied to each individual color channel. Such equalization imposes a monotonic global intensity transformation to the reconstructed intensity map so that the resulting color images agree with a visual inspection of the same sample using conventional lens-based microscopy tools. This intensity transformation can be obtained by minimizing the overall difference between the histograms of the reconstructed image and conventional microscope images within several subregions of the sample FOV. Once the transformations for all color channels are obtained, they can be applied to other regions or samples as long as the same illumination conditions apply.

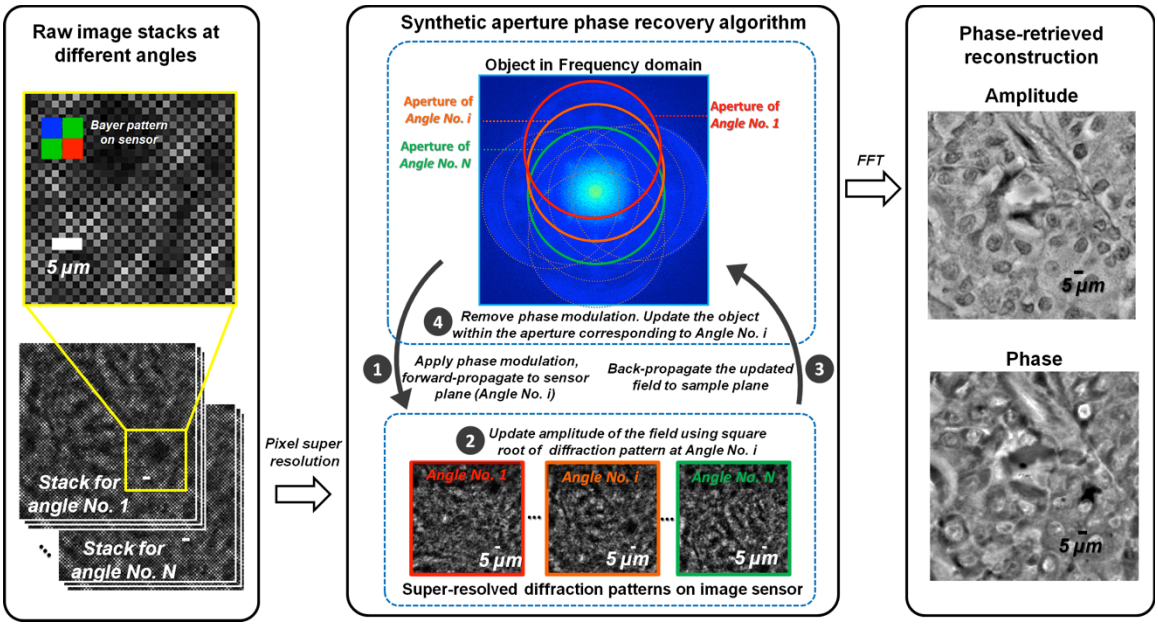

Figure 3.2 Reconstruction algorithm of lensfree on-chip imaging using the synthetic aperture approach. The pixel super-resolution algorithm uses lensfree lower-resolution images (left column) captured at different illumination angles (No. *1* through No. *N*) to synthesize pixel super-resolved in-line holograms. Middle: a four-step iterative process for synthetic aperture and phase retrieval, which is repeated for all the illumination angles. As an example, for a human breast tissue sample, the reconstruction of the complex sample field can be obtained (right column) after 5-10 cycles using 22 different illumination angles (-50° to 50° at 10° increments along two orthogonal axes).

Another method to create a color image is to digitally colorize a lensfree image that was reconstructed from *only one illumination wavelength*. This second colorization method maps intensity to color based on prior knowledge of the imaged sample (see, e.g., Figure 3.5). This colorization method works in the YUV color space [123,124], which contains three channels, the Y channel, which measures luma (brightness), and the U and V channels, which measure chrominance (color). The YUV color space can be converted to the RGB representation by a linear transformation. To map a mono-color image into a color image, the amplitude (or intensity) of the mono-color lensfree image is used as the Y channel, while the U and V channels can be inferred from the Y channel. The mapping is created by statistically learning a number of bright

field microscope color images of the same type of specimen that are also imaged by our lensfree on-chip microscope. In this training stage, the microscope images are transformed to the YUV color space, and a pixel-by-pixel scan then links each Y value to its corresponding average U and V values, yielding a nonlinear mapping. Before applying the mapping to the mono-color lensfree image, the brightness values of important features, such as the nuclei and the extra-cellular matrix, must be matched between the learning statistics and the to-be-colored gray scale image. This can be done either by manually picking features of interest or by matching histograms. We should emphasize that this learning step needs to be executed *only once* for each sample type of interest.

Digital phase contrast in lensfree on-chip imaging

Once the complex field of the sample is obtained after the phase retrieval steps, a phase shift of $\pi/2$ is digitally applied to its zero-frequency (i.e., DC) component. The intensity of this modified complex object field is then calculated to create a digital phase contrast image of the specimen (see, e.g., Figure 3.6).

Sample preparation steps

The grating lines (Figure 3.3) used for NA and resolution quantification are fabricated on a glass substrate using focused ion beam milling. Anonymized biological samples (human breast cancer tissue in Figures 3.4-5) were purchased from the Translational Pathology Core Laboratory (TPCL) at UCLA. Unstained Pap smears are prepared through ThinPrep® preparation (Figure 3.6). All these pathology slides are sealed between two glass slides. The gap between the sensor and glass slides is filled with refractive index matching oil (n = 1.52). The sample-to-sensor

distances are ~100 μm for grating lines, ~255 μm for breast cancer tissue slides, and ~350 μm for Pap smear slides.

3.3 Results and discussion

To demonstrate the NA improvement brought about by LISA, 250 nm grating lines were imaged under a 700 nm illumination wavelength using the unit magnification on-chip imaging set-up shown in Figure 3.1. As detailed in Figure 3.2, the spatial sampling limitation of the sensor chip due to its 1.12 μm physical pixel pitch and unit magnification is mitigated by using source-shifting-based pixel super-resolution, which achieves an effective pixel size of 100-150 nm. The remaining major limitation on spatial resolution is the loss of SNR for high spatial frequencies, which can be addressed by the synthetic aperture approach that we have taken (see the Methods Section). In the frequency domain, this loss of high spatial frequency information fills a low-pass filter function (3. 3a). Tilting the illumination angle shifts the passband of the imaging system to a new subregion, allowing higher spatial frequencies to be detected by the image sensor (Figure 3.3b). By digitally combining lensfree holographic measurements obtained at different illumination angles (see Figure 3.2 and the Methods Section), we obtain the 2D image of the object (Figure 3.3d) with a significantly broadened spatial bandwidth, as shown in 3.3b. Figure 3.3d illustrates our lensfree reconstruction results based on this synthetic aperture approach, clearly resolving 250 nm grating lines under a 700 nm illumination wavelength, which effectively corresponds to an NA of 1.4, i.e., 700 nm/(2 × 250 nm), much larger than earlier on-chip imaging results using similar sensor chips [98]. In this reconstruction result, the reduced modulation depth that is observed toward the edges can be partially attributed to the 3D structure of the fabricated grating, where focused ion beam milling induced structures at the edges start to

fall out of the reconstructed depth due to our high NA. Because resolution and FOV are decoupled in our on-chip imaging set-up (Figure 3.1), this large numerical aperture also comes with an ultra-large FOV of 20.5 mm^2, which constitutes the active area of the sensor chip.

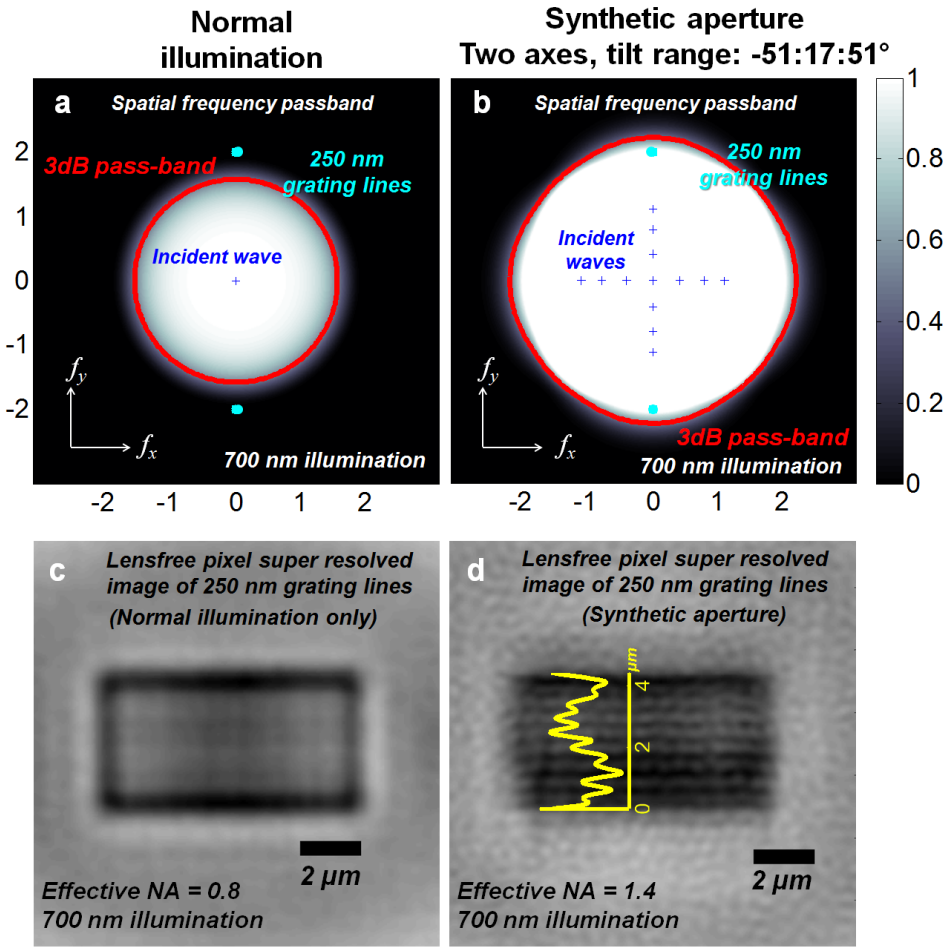

Figure 3.3. Our synthetic aperture approach enables lensfree on-chip imaging to reach a numerical aperture of 1.4. (**a**) and (**b**) show the imaging system passbands in the spatial frequency domain, without and with the synthetic aperture, respectively. (**c**) and (**d**) lensfree amplitude images of 250 nm grating lines without and with the iterative synthetic aperture reconstruction algorithm, respectively. The spatial frequencies of the grating lines are marked by cyan dots in (**a**) and (**b**). To reconstruct the image in (**d**), illumination angles of -51°:17:51° across two axes are used (λ = 700 nm), and four iterations, as described in Figure 3.2, were sufficient to achieve convergence. Note that the sample-to-sensor distance is ~100 µm.

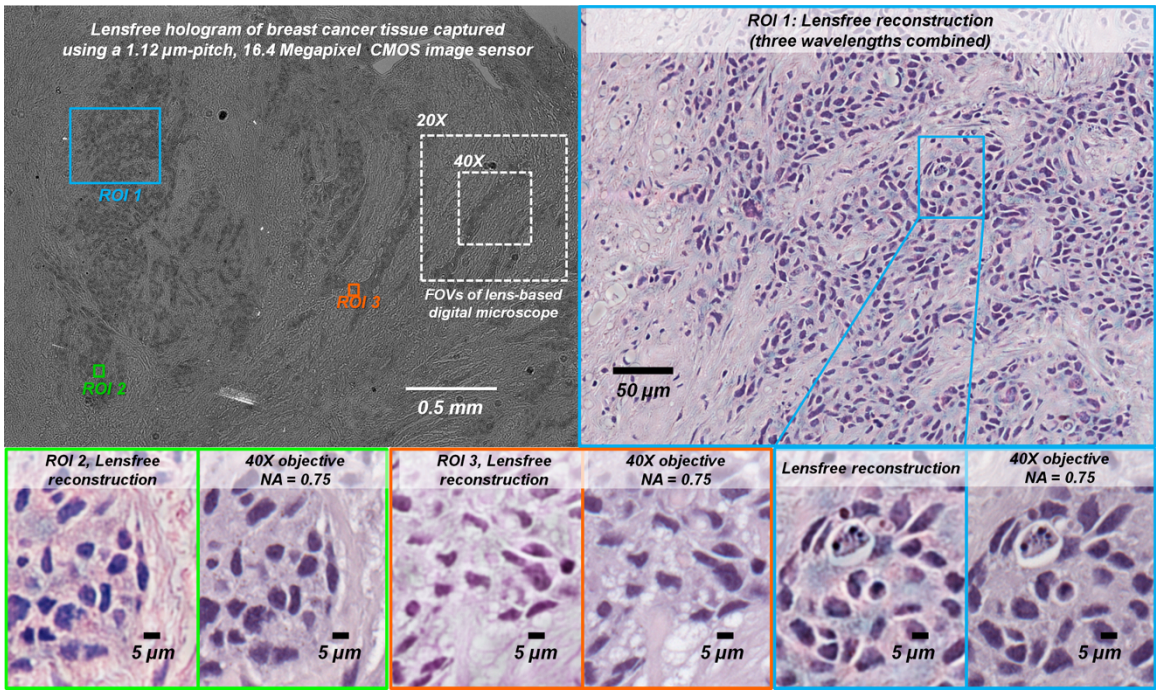

Figure 3.4 Lensfree color imaging of breast cancer tissue (H&E staining) using LISA. Top left: subregion of a lensfree hologram captured by a CMOS sensor chip; FOVs of 20× and 40× microscope objective lenses are also shown for comparison (white dashed squares). Top right: lensfree reconstruction of region of interest (ROI) No. 1. Bottom: zoomed images of lensfree reconstructions of various regions within the large reconstructed FOV. Conventional microscope images (40× objective, NA = 0.75) are also provided for comparison. To create the lensfree color image, on-chip holographic images at three different illumination wavelengths were used (λ = 472 nm, 532 nm, 632 nm). The sample-to-sensor distance is ~255 µm.

Next, to demonstrate the significantly improved phase recovery performance of LISA, as well as its accurate color rendering capability, we imaged connected tissue samples (i.e., H&E stained breast cancer tissue) over a wide FOV, as illustrated in Figure 3.4. During the image acquisition process, we sequentially imaged these pathology samples at three distinct wavelengths (472 nm, 532 nm and 632 nm) to digitally generate a lensfree color (i.e., RGB) image of the specimen [20,56]. LISA's color images (see Figure 3.4 and the Methods Section for details) show very good agreement with 40× microscope objective images of the same specimen.

To boost the data acquisition speed, we further demonstrated that lensfree color imaging capability can also be achieved by transforming the intensity channel of a holographically reconstructed image acquired at a single wavelength [20] into a pseudo-color image (see Figure 3.5). This intensity-to-color transformation, as successfully demonstrated in Figure 3.5, can be statistically established and fine-tuned based on prior knowledge of the sample type, as well as the stain of interest, and can provide a rapid solution for digital colorization of lensfree holographic images without the need to perform multi-wavelength illumination of the specimen.

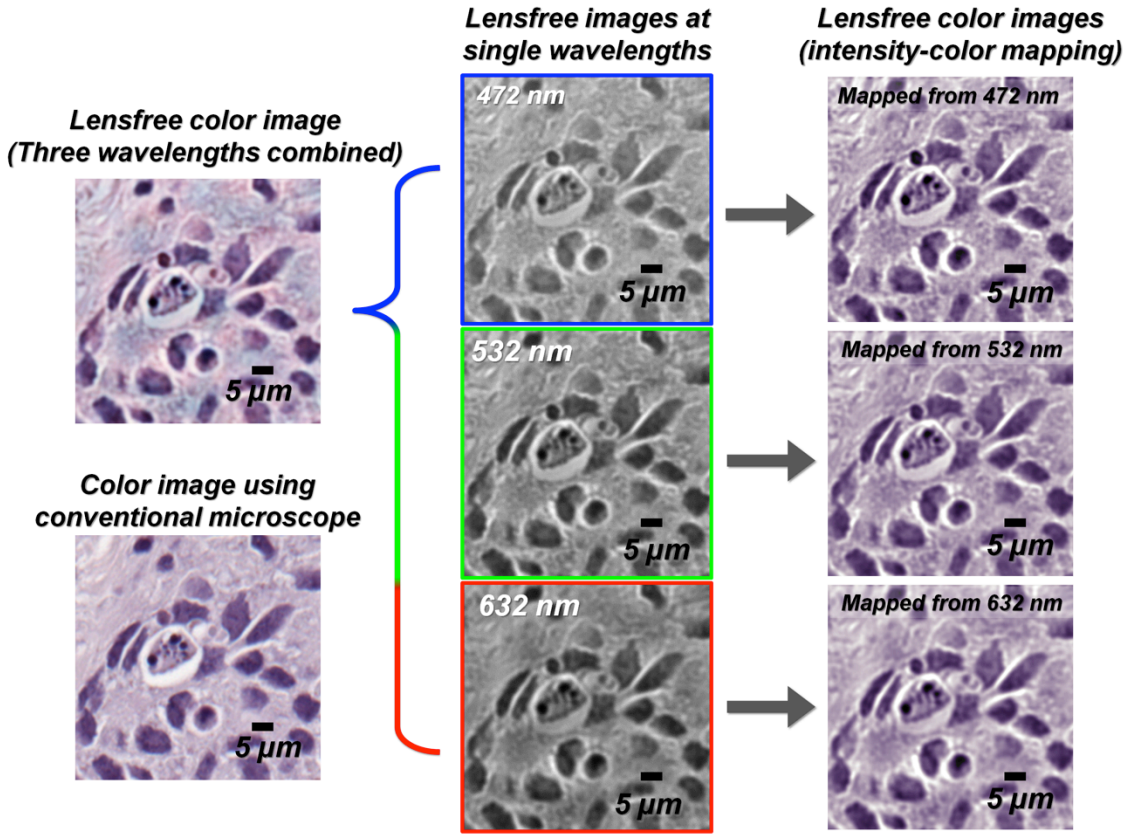

Figure 3.5 Colorization methods of LISA images. Top left column: lensfree color (RGB) image generated by combining the reconstructions from three wavelengths. Bottom left column: image of the same sample taken by a conventional lens-based microscope (40× objective, NA = 0.75). Center column: lensfree mono-color reconstructions at three different illumination wavelengths (λ = 472 nm, 532 nm and 632 nm). Right column:

lensfree color images generated by colorizing (using intensity for color mapping) a single gray scale image obtained using a single illumination wavelength. The specimen is a human breast cancer pathology slide.

To demonstrate the label-free imaging capabilities of LISA, we also imaged unstained *Papanicolaou* smear slides, as illustrated in Figure 3.6. Imaging this type of transparent and unlabeled samples usually requires adding a special objective lens and/or illumination module to a conventional microscope to convert optical path differences into brightness variations. With LISA, no additional components or modification in the reconstruction algorithm are needed because LISA inherently reconstructs both the amplitude and phase information of the specimen. In addition to directly visualizing the phase image of the specimen, as illustrated in Figure 3.6b and 6e, we can also digitally replicate the physical image formation process of a phase contrast microscope [125]. For example, a phase shift of $\pi/2$ can be added to the zero frequency component of the complex field, and the intensity of this new field mimics a phase contrast image, as seen in Figure 3.6c and 3.6f. These lensfree images provide decent agreement with images of the same sample taken by an actual phase contrast microscope using a 40× (NA=0.75) objective lens.

In lensfree on-chip microscopy, the characteristic signature is unit magnification, where the FOV and resolution are decoupled, setting the active area of the sensor array as the sample FOV. While these features are highly desirable for creating high-throughput and compact microscopy systems, they also create two major problems, both of which are related to the pixels of the sensor array: first, spatial undersampling due to large pixel size (e.g., 1-2 μm) and, second, poor SNR and aberrations experienced by high spatial frequencies due to the narrow pixel acceptance angle and the opto-electronic hardware in front of the active region of the pixels. Pixel super-resolution approaches [94,97] mitigate the first challenge by, e.g., source shifting, which creates sub-

pixel shifted replicas of the diffraction patterns of the samples on the sensor array, which can be utilized to digitally divide each pixel into smaller effective pixels, undoing the effects of spatial undersampling. To implement pixel super-resolution, LISA uses a very small angular modulation of the source (<0.5° in our setup), which is sufficient to generate a sub-pixel shift of the in-line hologram at the sensor plane. In contrast, shadow imaging-based on-chip microscopes [93] demand very large illumination angles (e.g., ± 60°) to be scanned to perform pixel super-resolution because their sample-to-sensor distances need to be sub-micron for acceptable spatial resolution. Stated differently, shadow-based on-chip microscopy utilizes angular diversity of the illumination *entirely* for pixel super-resolution [93], whereas LISA uses a much smaller angular range (<0.5°) to perform pixel super-resolution and leaves the rest of the angular space in illumination to increase the effective NA using a synthetic aperture. This synthetic aperture approach is essential to mitigate pixel-related aberrations and signal loss that high spatial frequencies inevitably experience in an on-chip microscope design, the effects of which become even worse at longer illumination wavelengths because the diffraction angles of a given band of high spatial frequencies increase with wavelength. Such an improvement in NA brought about by LISA is critical for maintaining a competitive resolution, especially at longer wavelengths, which paves the way for high resolution on-chip microscopy across the entire visible spectrum. Assuming that the partial coherence of light does not pose any resolution limitations (i.e., the spectral bandwidth and the spatial coherence of the illumination source are appropriately adjusted), this synthetic aperture-based on-chip microscope, through pixel super-resolution, can theoretically achieve an effective NA of $n_1 + n_2$, where n_1 is the refractive index of the medium above the sample plane and n_2 is the refractive index of the medium between the sample and sensor planes. However, SNR degradation of the lensfree holograms, especially at oblique

illumination angles and with larger sample-to-sensor distances, would create practical limitations to ideal pixel super-resolution and phase recovery, which would make it challenging to reach this theoretical NA value ($n_1 + n_2$). In fact, compared to Figure 3.3, the relatively lower resolution that is observed in our reconstructed LISA images in Figures 3.4-3.6 can be attributed to reduced hologram SNR and increased sample-to-sensor distance (from 100 μm in Fig. 3.3 to 255 μm and 350 μm in Figs. 3.4 and 3.6, respectively).

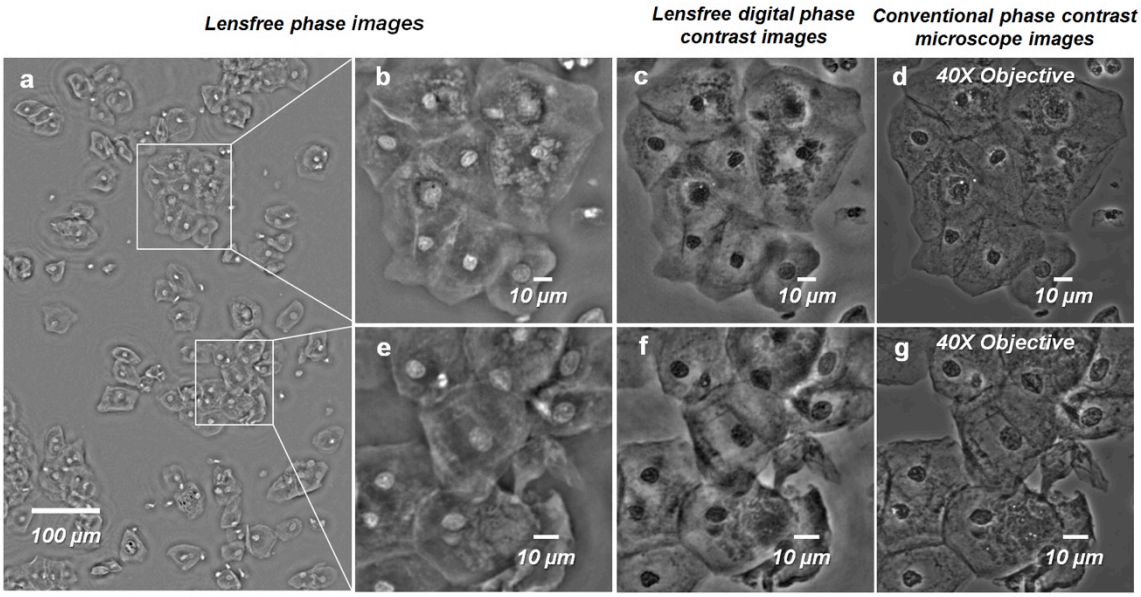

Figure 3.6. LISA images of an unstained Papanicolaou smear. (**a**) A phase image of the sample obtained after 6 iterations of the iterative synthetic aperture reconstruction algorithm and two zoomed in regions, (**b**) and (**e**). Note that with a regular lens-based microscope, these unstained cells suffer from poor contrast and could not be imaged, while the lensfree phase images reveal subcellular features of the specimen. (**c**) and (**f**) lensfree digital phase contrast images processed from (**b**) and (**e**), respectively. The corresponding conventional phase contrast microscope images (**d** and **g**) using a 40× objective-lens (NA = 0.75) are also provided for comparison. The sample-to-sensor distance is ~350 μm.

In addition to a significant NA increase, LISA also has a very important advantage for performing robust phase recovery, even for dense and connected tissue samples that have been

difficult to reconstruct using transmission-based in-line holographic methods. The high phase recovery performance of LISA relies on our iterative synthetic aperture approach and is illustrated using pathology samples, as presented in Figures 3.4-3.6. It should be emphasized that this complex wave retrieval step also enables us to digitally 'focus' on the sample plane without the need for *a priori* knowledge of the sample-to-sensor distance. As a comparison, precise depth focusing during the imaging process is crucial for lens-based systems, especially when high-NA lenses are used, and mechanical implementation of precise autofocusing during the scanning process can dramatically increase the complexity and cost of the imaging set-up. Moreover, for transparent samples, such as unlabeled biological tissue, focusing is particularly difficult using conventional microscopes unless costly additional optical components are added to the imaging system. LISA replaces such laborious processes with automated sample-to-sensor distance search and angle calibration algorithms (detailed in the Methods Section), which enable autofocusing of the complex optical wave on the sample plane during the reconstruction process. Stated differently, local fluctuations of the vertical gap between the sample and sensor planes across the large imaging FOV are digitally tolerated in LISA, which is another major advantage over shadow-based on-chip microscopy. Shadow-based imaging demands the same vertical gap to be sub-micron across the entire FOV, which is rather difficult to satisfy in real samples. Placing the specimen directly in contact with the sensor chip surface can *partially* mitigate such height/depth variations for perfectly planar 2D objects, but it comes with the risks of significantly heating the sample and damaging the sensor and, more importantly, will inevitably demand very large illumination angles to perform pixel super-resolution. These large illumination angles unfortunately introduce major spatial artifacts for shadow/contact imaging [58] because, at high illumination angles, the shadow of the specimen cannot be considered as a

shifted version of the same object function, which forms the basic assumption of pixel super-resolution. Using synthetic aperture enabled robust phase recovery, LISA mitigates these autofocusing challenges and related spatial artifacts while maintaining a simple, cost-effective and unit magnification imaging design.

Once the high resolution complex field of the sample is recovered, various visualization methods are at the user's disposal, such as multi-wavelength-based colorization [56], intensity-based color mapping [20] and digital phase contrast techniques (see the Methods Section). Compared with the intuitive method of combining reconstructions at multiple wavelengths (e.g., red, green, blue) to digitally form a color image of the sample, intensity-based color mapping/transformation [20] takes advantage of prior knowledge of the sample type and staining method to transform a lensfree mono-color intensity image into a color image (see Figure 3.5). While such an approach could greatly reduce the data acquisition and reconstruction time for an unknown sample of interest without prior information of staining, lensfree colorization using the red, green and blue channels, as illustrated in Figure 3.3, would generally be the optimal choice.

To image transparent and colorless samples, instead of physically adding optical components to obtain phase contrast images, we can simply apply a digital phase shift to the zero frequency component of the holographically reconstructed complex object to mimic the physical image formation in phase contrast microscopy [125], and the intensity of this phase-shifted field serves as the phase contrast image of the sample. Such images can be especially appealing for unstained pathology samples (see, e.g., Figure 3.6), as they visualize and enhance the contrast of spatial features that are difficult to observe under regular bright field microscopes.

Although our proof-of-concept LISA system includes mechanical components such as linear stages to perform source-shifting-based pixel super-resolution and a rotational arm to vary the illumination angle, the implementation of our optical setup can be further simplified and constructed without any moving components. As demonstrated earlier, source shifting can be performed by sequentially lighting up fibers within a bundle that are individually butt-coupled to light emitting diodes (LEDs) [94–96]. Furthermore, as a result of our wide passband in the frequency domain (i.e., 2.0 ~ 3.2 μm^{-1} in diameter), the number of illumination angles can also be reduced to, e.g., ~20 angles, further simplifying the optical set-up. Because the angle calibration is carried out during our numerical reconstruction process, precise alignment of the LISA set-up and illumination sources is *not* required, making the system robust even for mobile applications.

Being a computational imaging technique, LISA not only benefits from the rapid evolution in image sensor technology but also from advances in computing power; both the image sensor pixel count and CPU transistor count have exhibited exponential increases in the past decade, and such advances would provide immediate improvements to the performance of LISA in terms of larger space-bandwidth products and faster reconstructions. Parallel-computing platforms, such as graphics processing units (GPUs) and computer clusters, could also significantly increase the reconstruction speed of LISA, as our entire reconstruction algorithm is highly parallelizable. For instance, our full FOV (~20.5 mm^2) image reconstruction can be digitally divided into subregions for parallel processing, and for each subregion, pixel super-resolution can be individually performed for different illumination angles. Our phase retrieval algorithm relies extensively on fast Fourier transform (FFT) operations, which can also be significantly

accelerated by using GPUs. In its current implementation, without parallel computing or GPU use, the entire image reconstruction (including pixel super-resolution and phase retrieval) for a 1 × 1 mm subregion takes ~46 minutes on a single desktop computer (Intel Xeon E5-1620) using MATLAB (see the Methods section). This leaves significant room for speed improvement in our reconstructions; for example, utilization of the *C* language (instead of MATLAB) on a GPU could accelerate the phase recovery process by ~20 folds [90].

3.4 Conclusions

We demonstrated an on-chip microscopy modality that can achieve a numerical aperture of 1.4 across a very large field-of-view (20.5 mm^2) under unit magnification and without any lenses. This wide-field on-chip microscope utilizes multiple angles of illumination to holographically synthesize the largest numerical aperture reported for an on-chip microscope and enables color imaging of tissue samples, including pathology slides, using complex wave retrieval. Its simple and compact design makes this partially coherent holographic on-chip microscopy platform highly appealing for high-resolution and wide-field imaging applications in biomedical and physical sciences.

Chapter 4 Wavelength scanning pixel super-resolution

Parts of this chapter have been previously published as Luo W, Zhang Y, Feizi A, Göröcs Z, Greenbaum A, Ozcan A. Pixel super-resolution using wavelength scanning. Light Sci Appl 2015. doi:10.1038/lsa.2016.60.

Undersampling and pixelation affect a number of imaging and microscopy systems, limiting the resolution of the acquired images, which becomes especially significant for wide-field microscopy applications. Various super-resolution techniques have been implemented to mitigate this resolution loss by utilizing sub-pixel relative displacements in the imaging system, achieved by e.g., shifting the illumination source, the sensor array and/or the sample, followed by digital synthesis of a smaller effective pixel-size by merging this sequence of sub-pixel shifted low-resolution images. Here we introduce a new pixel super-resolution method that is based on wavelength scanning and demonstrate that, as an alternative to physical shifting/displacements, wavelength diversity can be used to boost the resolution of a wide-field imaging system and hence significantly increase its space-bandwidth product. We confirmed the success of this new technique by improving the resolution of lensfree microscopy and developed an iterative algorithm to generate high-resolution reconstructions of the specimen using undersampled diffraction patterns recorded at a few wavelengths, covering a narrow spectrum (~10-30 nm). When combined with a synthetic aperture technique, this wavelength scanning super-resolution approach can achieve a half-pitch resolution of 250 nm, corresponding to a numerical aperture of ~1.0, across a large field-of-view (>20 mm^2). We further demonstrated the success of this approach by imaging various biological samples, including blood and Papanicolaou smears. Compared to displacement-based super-resolution, wavelength scanning brings uniform

resolution improvement in all directions across the sensor array and requires significantly less number of measurements. This technique would broadly benefit wide-field imaging and microscopy applications that demand larger space-bandwidth products.

4.1 Introduction

High-resolution imaging across a wide field-of-view (FOV) is essential for various applications in different fields and it requires imaging systems to have large space-bandwidth products. Ever since the wide adoption of charge-coupled devices (CCDs) and complementary metal-oxide semiconductor (CMOS) based image sensors to capture digital images, tremendous amount of research and development has been devoted in optics, semiconductor technologies and signal processing to create high-resolution and wide-field imaging and microscopy systems. In conventional lens-based optical imaging designs, a large space-bandwidth product can be achieved by using higher magnification and bigger lenses, and the image sensors are accordingly made larger in area with more pixel counts. Another approach is to make image sensors with smaller pixel pitch while still maintaining a relatively large active area. However, both of these approaches have drawbacks: larger optical components make the imaging system bulky and significantly more expensive, on the other hand physically reducing the pixel size sacrifices the signal-to-noise ratio (SNR) because less light sensing area is made available for each pixel, reducing the external quantum efficiency of the imager chip[126].

As an alternative, optical signal processing community has provided a powerful framework, which is termed pixel super-resolution[127,62,69,121,7027,62,69,121,70 28,63,70,122,71 127,62,69,121,70], to obtain a high-resolution image from a series of low-resolution (i.e., undersampled) images. Pixel super-resolution was originally developed in lens-based, point-to-point projection imaging systems[127,62,69,121,70] and later has been applied to lensfree and holographic imaging

techniques[90,94,97,128–130] to significantly enhance the space-bandwidth product of the reconstructed images using both CCD and CMOS imager chips. In either implementation, lens-based or lensfree, this super-resolution framework requires the low-resolution undersampled measurements to have subpixel shifts with respect to each other so that new and independent information can be exploited at each raw measurement (even though pixelated) to digitally synthesize a much smaller effective pixel size for the reconstructed image.

Here we introduce a fundamentally new pixel super-resolution method that utilizes wavelength scanning to significantly improve the resolution of an undersampled or pixelated imaging system, without the use of any lateral shifts or displacements. In this technique, the specimen is sequentially illuminated at a few wavelengths that are sampled from a rather narrow spectral range of ~10-30 nm. Compared to sub-pixel displacement or lateral shift-based super-resolution techniques, wavelength scanning brings uniform resolution improvement across all the directions on the sample plane and requires significantly less number of raw measurements to be made. Reduced number of measurements without sacrificing performance could greatly benefit high-speed wide-field imaging, field-portable microscopy and telemedicine applications, which are all sensitive to data transmission and storage.

We demonstrated the success of this new wavelength scanning based pixel super-resolution approach using lensfree holographic microscopy (Figure 4.1) to improve the resolution and the effective numerical aperture (NA) of a unit magnification imaging system by a factor of ~4 in all directions. Using 12 different illumination wavelengths between 480 nm and 513 nm, we achieved a half-pitch resolution of ~250 nm and an effective NA of ~1.0 across a large FOV of >20 mm^2. At the heart of these results, there is an iterative pixel super-resolution algorithm that

was developed to obtain high-resolution complex (i.e., phase *and* amplitude) reconstructions from undersampled (i.e., pixelated) lensfree digital holograms acquired at different wavelengths.

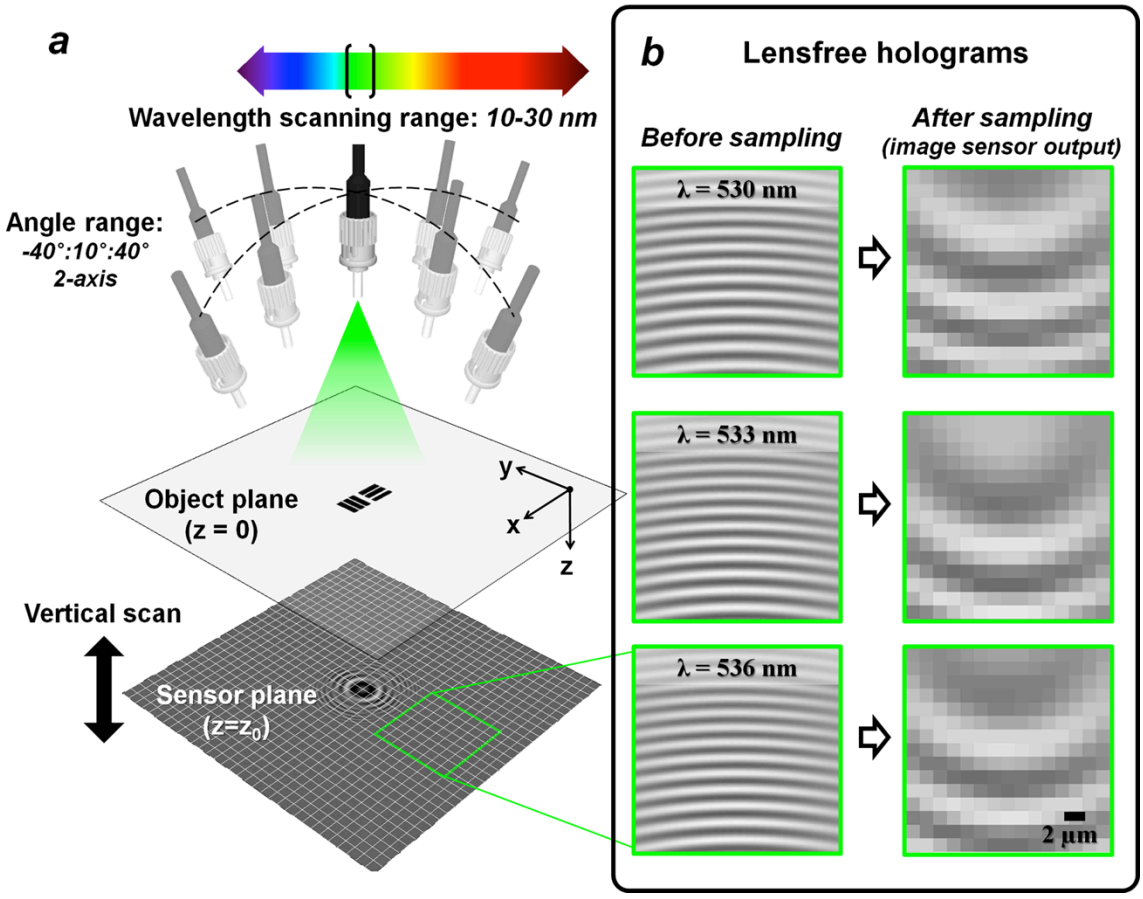

Figure 4.1. Optical setup of wavelength scanning pixel-super resolution. **(a)** A lensfree holographic on-chip microscope using wavelength scanning pixel super-resolution. A fiber-coupled tunable light source is placed above the object. When performing pixel super-resolution, the wavelength is scanned within a spectral range of ~10-30 nm. Multi-height and synthetic aperture imaging configurations are also integrated into this setup to enable phase retrieval. **(b)** Lensfree holograms at different wavelengths before and after digital sampling at the image sensor plane.

In previous work, wavelength diversity in illumination has been mainly utilized for two general purposes. The first one has been to obtain color or spectral information of the sample[82,131–142]; wavelength-dependent transmission, absorption or scattering features of the

specimen enhance the contrast of the image and might reveal chemical and/or physical properties of biological samples. The second purpose is to recover the phase of the optical wavefront in digital holography. Earlier reports[143–146] have demonstrated a phase retrieval technique by tuning the wavelength of the illumination for non-dispersive objects. This wavelength diversity based phase retrieval approach requires the illumination to be tuned in a rather large spectral range[143–146] (i.e. > 60 nm) and assumes that the specimen maintains similar transmission properties across such a large bandwidth. Recently a means of using wavelength diversity to provide modest (e.g., ~16%) improvement in resolution has also been reported[147]. However this method also assumes that the transmission properties of the specimen remain constant (unchanged) across an even larger spectral range of >400 nm (i.e., 460-870 nm), which would not be satisfied for realistic samples, including e.g., pathology slides and most biological specimens.

Besides significantly improving the resolution and the space-bandwidth product of the imaging system, our wavelength scanning pixel super-resolution approach over a narrow band also helps in robust phase unwrapping to accurately determine the optical path length differences between the sample and surrounding medium[148–150]. For samples where the optical path length is larger than the wavelength, the obtained phase map will be wrapped. Especially when the object has sharp boundaries, such errors may be difficult to correct using state-of-the-art phase unwrapping techniques based on a single wavelength reconstruction[151–154]. By making use of all the illumination wavelengths in our super-resolution approach, we also demonstrated robust phase unwrapping in our high-resolution microscopic phase images, correctly revealing the optical path length information of the samples.

In addition to lensfree and/or holographic imaging techniques, the same wavelength scanning based super-resolution framework can also be applied to improve the resolution of lens-based

imaging techniques (with the introduction of a slight defocus), making this work broadly applicable to various coherent or partially coherent wide-field imaging modalities that are limited by pixelation or undersampling. Therefore, we believe that this new wavelength scanning based super-resolution technique would largely benefit various wide-field microscopy applications that require enhanced space-bandwidth products.

4.2 Materials and methods

Optical setup

As depicted in Figure 4.1, the optical setup of the lensfree microscope consists of three major components: the light source, the image sensor array, and the specimen. A fiber-coupled, wavelength-tunable light source (WhiteLase-Micro, model VIS, Fianium Ltd, Southampton, UK) is used to perform the wavelength scanning. During the imaging process, the central wavelength of the source is scanned within a spectral range of ~10-30 nm (e.g., from 498 nm to 510 nm) with a step size of ~3 nm. The spectral linewidth of illumination at each wavelength is ~2 nm, and the power of the light source is adjusted to ~20 μW. The image sensor chip is a 1.12-μm pixel size color CMOS sensor-chip manufactured for cellphone camera modules (IU081, Sony Corporation, Japan). During the imaging process, the specimen is mounted on a transparent substrate and placed ~100-500 μm above the image sensor chip. We merged our wavelength scanning based pixel super-resolution approach with both multi-height[129] and synthetic aperture imaging[130] configurations to obtain phase-retrieved, high-resolution reconstructions of the specimen. For synthetic aperture based imaging[130], the fiber outlet of the light source is mounted on a *rotational* arm (PRM1Z8, Thorlabs, New Jersey, USA), and the image sensor is placed on a stage which can rotate within a horizontal plane. Therefore the incident light can be set to

arbitrary illumination angles, needed for the synthetic aperture approach. For the multi-height based phase retrieval[128,129], the incremental height change between the image sensor and the specimen is enabled by a mechanical positioning stage (MAX606, Thorlabs, New Jersey, USA). The image sensor is mounted on this mechanical stage whereas the specimen is held by a 3D-printed sample holder. After finishing the image capture for each height, the stage lowers the image sensor by typically 10-15 μm before the image capture for the next height starts. During the imaging process, all the necessary steps, including the wavelength scanning of the light source, multi-height and synthetic aperture related scans and the data acquisition using the image sensor chip are automated by a custom-written LabVIEW code (Version 2011, National Instruments, Texas, USA).

Wavelength calibration and dispersion compensation

Wavelength calibration of our light source is achieved using an optical spectrum analyzer (HR2000+, Ocean Optics, Amersham, UK). The intensity-weighted average wavelength of each measured spectrum is considered as our illumination wavelength. To achieve optimal resolution, the refractive index of the glass substrate (100 μm, N-BK7, Schott AG, Mainz, Germany) at each wavelength is also corrected using the dispersion formula for borosilicate glass.

Sample preparation

The grating lines used for resolution quantification are fabricated on a ~100 μm glass slide (N-BK7, Schott AG, Mainz, Germany) using focused ion beam (FIB) milling. Unstained Papanicolaou (Pap) smear slides are prepared through ThinPrep® method (Hologic,

Massachusetts, USA). The blood smear samples are prepared using EDTA (ethylenediaminetetraacetic acid) anticoagulated human blood and stained with Wright's Stain[155].

Mathematical formalism of wavelength scanning pixel super-resolution

We assume that the specimen is a thin object mounted on a plane parallel to the image sensor chip and that the specimen is sequentially illuminated by multiple wavelengths $\{\lambda_k\}$. At a given wavelength λ_k, the object wave can be written as $o_k(x,y)=1+s_k(x,y)$, where $s_k(x,y)$ represents the scattered object wave, right at the exit of the object plane (z = 0, in Figure 4.1a). The 2D Fourier transform of $o_k(x,y)$ can be written as $O_k(f_x,f_y)=\delta(f_x,f_y)+S_k(f_x,f_y)$. At the image sensor plane ($z = z_0$ in Figure 4.1a), the Fourier transform of the intensity distribution, $i_k(x,y)$, can be written as (see the Supplementary Materials for details):

$$I_k=\delta+T_k\cdot S_k+\left(T_k^{-}\cdot S_k^{-}\right)^{*}+SS_k \tag{4.1}$$

To simplify our notation, we hide the expression of the variables for spatial frequencies (f_x,f_y), and the superscript '-' stands for $(-f_x,-f_y)$. On the right hand side of Eq. (4.1), the first item, δ, represents the background intensity; the second and third items are conjugate holographic terms, which represent the interference of the scattered object wave with the background wave at the sensor plane. The fourth item is the self-interference term, which can be considered to be negligible for weakly scattering objects. The expression of T_k can be written as:

$$T_k(f_x,f_y)=H_k^{*}(f_{x,k},f_{y,k})\cdot H_k(f_x+f_{x,k},f_y+f_{y,k}) \tag{4.2}$$

where $H_k(f_x,f_y)$ is the free space transfer function, and the frequency shifts $f_{x,k}$ and $f_{y,k}$ are determined by the illumination wavelength and the incident angle (refer to the Supplementary Materials for details). After the object intensity is sampled by an image sensor array with a pixel

pitch of Δx and Δy, the discrete Fourier transform (DFT) of the sensor's output can be expressed as[156]:

$$I_{sampled,k} = \sum_{u,v=0,\pm1,\ldots} I_{pix,k}(f_x - \frac{u}{\Delta x}, f_y - \frac{v}{\Delta y}) \tag{4.3}$$

where u and v are integers, f_x and f_y are discrete spatial frequency values. Note that $I_{pix,k}(f_x,f_y) = I_k(f_x,f_y)\cdot P_k(f_x,f_y)$, and $P_k(f_x,f_y)$ represents the Fourier transform of the pixel function, i.e., the 2D responsivity distribution[98] within each pixel: $p_k(x,y)$. Variables u and v represent the order of *spatial aliasing due to pixelation*, and (u, v) = (0,0) corresponds to the non-aliased real (i.e., target) signal. The periodic nature of DFT enables us to extend the expression of $I_{sampled,k}$ to a broader range of frequency space by upsampling (Figure 4.2). Based on these definitions, we can express the undersampled or pixelated lensfree hologram at a given wavelength λ_k as such:

$$I_{sampled,k} = \sum_{u,v}\left[\delta_{uv} + T_{uv,k}\cdot S_{uv,k} + \left(T^{-}_{uv,k}\cdot S^{-}_{uv,k}\right)^{*} + SS_{uv,k}\right]\cdot P_{uv,k} \tag{4.4}$$

The non-aliased target signal $o_k(x,y)$ or its spatial Fourier spectrum can be obtained under (u, v) = (0,0), i.e., $\delta_{00} + S_{00,k}$, which can be written as:

$$\begin{aligned}\left(\delta_{00} + S_{00,k}\right)\cdot P_{00,k} = {} & T^{*}_{00,k}\cdot I_{sampled,k} - T^{*}_{00,k}\cdot T^{-*}_{00,k}\cdot P_{00,k}\cdot S^{-*}_{00,k} \\ & - \sum_{u\neq0,v\neq0}\left(T^{*}_{00,k}\cdot T_{uv,k}\cdot P_{uv,k}\cdot S_{uv,k} + T^{*}_{00,k}\cdot T^{-*}_{uv,k}\cdot P_{uv,k}\cdot S^{-*}_{uv,k}\right) \\ & - \sum_{u\neq0,v\neq0} T^{*}_{00,k}\cdot\delta_{uv} - \sum_{u,v=0,\pm1,\ldots} T^{*}_{00,k}\cdot P_{uv,k}\cdot SS_{uv,k}\end{aligned} \tag{4.5}$$

On the left side of Eq. (4.5), we still keep the pixel function $P_{00,k}$, which can be removed later, at the last step of the image reconstruction, using e.g., spatial deconvolution with a Wiener filter[124] as illustrated in Ref. [98]. Eq. (4.5) also shows that, in order to obtain the non-aliased object at (u, v) = (0,0), one needs to eliminate or subtract four terms from the upsampled and back-propagated holographic term (i.e., $T^{*}_{00,k}\cdot I_{sampled,k}$). For this aim, the first item to eliminate,

$T^{*}_{00,k} \cdot T^{-*}_{00,k} \cdot P_{00,k} \cdot S^{-*}_{00,k}$, is the twin image noise, a characteristic artifact of in-line holography. The second term in Eq. (4.5), which contains $S_{uv,k}$ and $S^{-*}_{uv,k}$ ($u \neq 0$, $v \neq 0$) in the summation represents the effects of spatial aliasing and undersampling for both the real and twin image terms. The third item, which contains δ_{uv} in the summation is the periodic background artifact generated during the upsampling process, and the last item is the self-interference term and its upsampling related artifacts. Starting with the next subsection, we will discuss a two-stage reconstruction algorithm to eliminate all these four items listed on the right side of Eq. (4.5) using wavelength scanning to enable super-resolved reconstructions of complex (i.e., phase and amplitude) object functions.

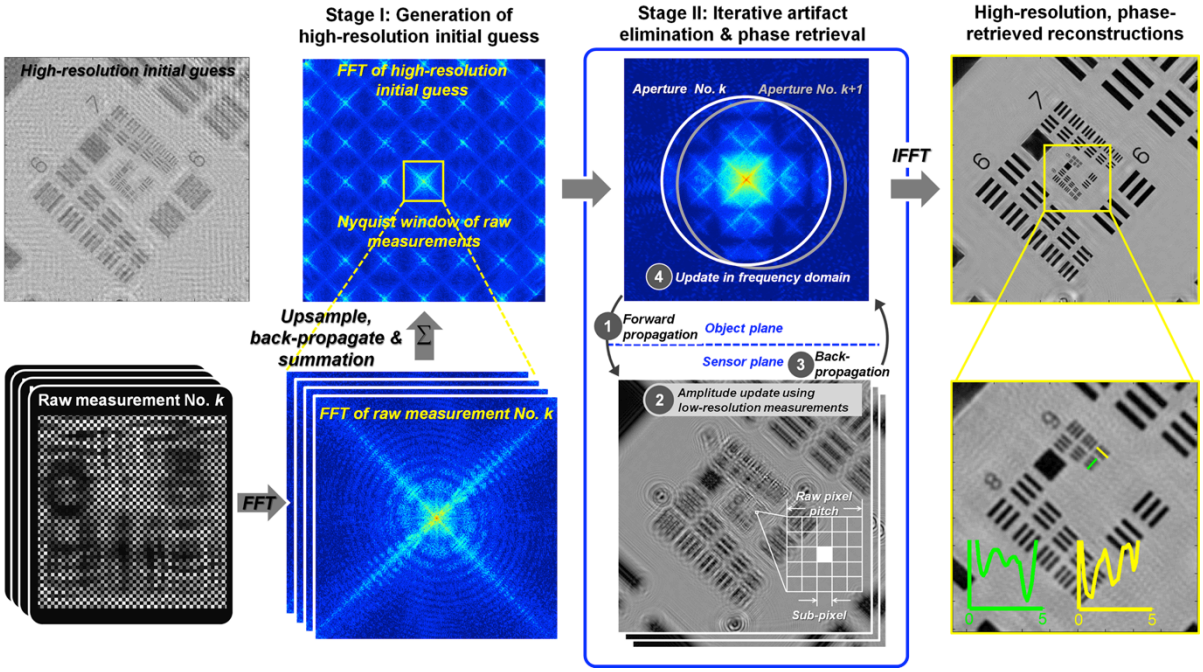

Figure 4.2. Reconstruction algorithm for wavelength scanning pixel super-resolution, integrated with multi-height or synthetic aperture based lensfree phase retrieval. Refer to the Materials and Methods Section for further details. The fourth column shows super-resolved and phase retrieved reconstruction of the specimen. FFT, fast Fourier transform; IFFT, inverse fast Fourier transform.

Reconstruction Stage 1: Generation of a high-resolution initial guess of the specimen using wavelength diversity

As depicted in Figure 4.2, the reconstruction of the specimen image includes two stages. First, notice that in Eq. (4.5) the functions $\{T^*_{00,k} \cdot T_{uv,k}$ ($u\neq0$, $v\neq0$)$\}$ have complex values with a unit amplitude, and their phases are very sensitive to changes in wavelength (see the Supplementary Materials for details). Therefore, when the illumination wavelength (λ_k) is scanned over K different wavelengths that are uniformly spread across a narrow bandwidth, the set of functions $\{T^*_{00,k} \cdot T_{uv,k}$ ($u\neq0$ or $v\neq0$)$\}$ can be considered as rotating unit vectors, and by summing up all these rotating vectors as a function of wavelength, we can get:

$$\left|\sum_{k=1}^{K} T^*_{00,k} \cdot T_{uv,k} \cdot P_{uv,k}\right| << K \cdot \left|P_{uv,k}\right| \tag{4.6}$$

This expression means that by summing up all the back propagations at different wavelengths (over a narrow spectral range of e.g., 10-30 nm), the reconstructed image, i.e., $\delta_{00} + S_{00,k}$ or $\left(\delta_{00} + S_{00,k}\right) \cdot P_{00,k}$, can be significantly enhanced by a factor of K while the spatial aliasing and undersampling related terms with $T^*_{00,k} \cdot T_{uv,k}$ will be considerably suppressed. Therefore in this first stage of our reconstruction process, we generate a high-resolution ***initial guess*** of the specimen by summing up all the upsampled and back-propagated raw measurements, i.e., low-resolution diffraction patterns. We subtract the artifacts items $\{\delta_{uv}$ ($u\neq0$, $v\neq0$)$\}$ before the back-propagation step to create a cleaner image.

Notice that modifying Eq. (4.6) into a weighted average at each spatial frequency point could achieve better suppression of spatial aliasing and undersampling related artifacts. However, using our current computation platform that is based on a central processing unit (CPU), search

for optimal weighting factors at each frequency point will significantly increase the total computation time. Therefore, in this proof-of-concept implementation, we chose a simpler summation approach to minimize the computation time for generation of the *initial* object guess. *The spatial aliasing and undersampling related artifacts of this initial guess will be further eliminated and cleaned up during the second stage of our algorithm, as will be detailed next*.

Reconstruction Stage 2: Multi-wavelength based iterative pixel super-resolution and phase retrieval

The second stage of our numerical reconstruction is composed of an iterative algorithm, which contains four sub-steps in each iteration:

(*1*) Knowing each raw measurement's corresponding wavelength and incidence angle, we apply the corresponding plane wave illumination on the initial guess of the specimen (from Stage 1, discussed above) and propagate the optical field from the object plane to the image sensor plane using the angular spectrum approach[66].

(*2*) Update the amplitude of the high-resolution field on the image sensor plane using the low-resolution measurement at the corresponding wavelength. In order to do so, the intensity of the high-resolution field is convolved with the image sensor's pixel function and downsampled to the same grid size as the pixelated raw measurement. The difference between the raw measurement and the downsampled intensity map is considered as a low-resolution 'correction' map for each illumination wavelength. A high-resolution correction map can be then generated by taking the Kronecker product of this low-resolution map and the pixel function. To perform a smooth update, this high-resolution correction map is added to the high-resolution intensity distribution with a relaxation parameter, typically set to ~0.5. After the smoothened update, a

Wiener deconvolution filter which incorporates the image sensor's noise level is applied on this updated intensity distribution. The square root of this filtered high-resolution intensity distribution is then applied to the amplitude of the field on the sensor plane while the phase map is kept *unaltered*.

(*3*) This updated field is then back-propagated to the object plane.

(*4*) The back-propagated field is used to update the transmission field on the object plane. This update is performed in the frequency domain (see Figure 4.2) within a circular area whose center is determined by the corresponding illumination wavelength and angle. The radius of this circle is defined by the boundary within which all the spatial frequencies experience less than 3dB attenuation after propagation in spatial domain. This update on object plane is also smoothened using a relaxation factor of ~0.5. After the update, the phase of the field on the object plane is converted to an optical path length map, and its amplitude is directly used as the transmission of the object.

These four steps described above are performed for every raw (i.e., undersampled) measurement captured by the image sensor array. It is considered as *one iteration cycle* when each one of the raw measurements has been used for amplitude update. Typically after 5-10 iteration cycles the reconstruction converges. The convergence condition for the iteration is defined as[157]:

$$\left| SSE_{avg}^{itr} - SSE_{avg}^{itr-1} \right| < \varepsilon \tag{4.7}$$

where SSE_{avg}^{itr} is the sum squared error between the raw measurement and the downsampled intensity map[157], '*itr*' is the index of the iteration, and ε is a convergence constant, typically determined by the noise level of the raw (undersampled/pixelated) measurements.

Phase retrieval using multi-height and synthetic aperture techniques

Multi-height[128,129,100,101,103] and synthetic aperture[130] techniques have been proven to be robust phase retrieval methods for lensfree on-chip imaging. In previously reported lensfree reconstructions[128–130], pixel super-resolution and phase retrieval are carried out sequentially: at each height or illumination angle, first lateral shift-based pixel super-resolution is performed to obtain high-resolution diffraction patterns on the image sensor plane. Then these super-resolved diffraction patterns are used by an iterative phase retrieval algorithm, where wave propagations between the object plane and the image sensor plane are executed repeatedly[128–130]. *However*, in wavelength scanning based pixel super-resolution, raw measurements are essentially undersampled versions of *different* holograms. Therefore, we chose to use the same iterative algorithm detailed in the previous subsection (i.e., Reconstruction Stage 2) to realize resolution enhancement *and* phase retrieval altogether. More specifically, in the multi-height configuration, the specimen is illuminated sequentially at each wavelength, and the corresponding lensfree holograms are captured before the vertical scanning stage moves the sample or the image sensor to the next height. Each height will be labeled with index l and therefore all the measurements $\{I_{sampled,k}\}$ and the corresponding transfer functions $\{H_k\}$ and $\{T_{uv,k}\}$ that are used in the previous derivations can be relabeled as $\{I_{sampled,kl}\}$, $\{H_{kl}\}$ and $\{T_{uv,kl}\}$, respectively. During the numerical reconstruction process, all the raw holograms are upsampled, back-propagated, and then summed together to generate the high-resolution initial guess at a given height. In Stage 2 of our reconstruction algorithm, the aforementioned four-step process is applied to each raw measurement. The same set of operations and processing also apply to the synthetic aperture technique,[130] except that index l now refers to each illumination angle instead of sample height.

In general, for pathology slides such as blood smears and Pap smears, the optical path length difference between the specimen (i.e., biological tissue) and the medium (i.e., air or the sealing glue) is rather small. Under these circumstances, phase unwrapping is not a concern and therefore in the phase recovery process we can use a scrambled order of $\{ I_{sampled,kl} \}$ in each iteration cycle. However, when dealing with samples with larger optical path length differences such as grating lines carved into a glass substrate, one extra step, i.e., phase unwrapping needs to be added after the reconstruction, and the order of iterations also needs to be modified accordingly, which will be detailed in the next sub-section.

Multi-wavelength phase unwrapping

A robust phase unwrapping algorithm requires high-resolution and phase-retrieved reconstructions at multiple wavelengths, therefore we divide the raw measurements into subsets, where the wavelengths are identical or very close (e.g., $\Delta\lambda \leq 5$ nm), and perform the four-step reconstruction process discussed earlier (as part of the Reconstruction Stage 2) on each subset separately. For example, reconstruction No.1 uses subset $\{ I_{sampled,kl} \mid k=1, l=1,\ldots L\}$, No. 2 uses $\{ I_{sampled,kl} \mid k=2, l=1,\ldots L\}$, etc. When iterations for all these subsets are finished, we end up with high-resolution (i.e., super-resolved) phase-retrieved reconstructions at multiple wavelengths, i.e., $\{O_k\}$, whose phase maps $\{ \phi_{k,wrapped} \}$ need unwrapping. Using these wrapped phase maps $\{ \phi_{k,wrapped} \}$ at multiple wavelengths, we perform phase unwrapping to accurately reveal the optical path length differences between the specimen and the surrounding medium. Assuming that the optical path length difference is $\Delta L(x,y)$, the phase distribution at the object plane at each wavelength can be written as $\phi_k(x,y) = 2\pi \cdot \Delta L(x,y) / \lambda_k$. The wrapped phase can then be expressed as $\phi_{k,wrapped}(x,y) = \phi_k(x,y) \pm 2N\pi$ where $-\pi < \phi_{k,wrapped} \leq \pi$ and N is an integer. These

resulting wrapped phase maps { $\phi_{k,wrapped}$ } that are generated through super-resolved and phase-retrieved reconstructions at multiple wavelengths are then fed into an optimization algorithm[158] which finds an optimum path length $\Delta L_{opt}(x,y)$ at each spatial point (x,y) by minimizing a cost function that is defined as:

$$\sum_{k=1}^{K}\left|e^{j\phi_k(x,y)}-e^{j2\pi\cdot\Delta L_{opt}(x,y)/\lambda_k}\right|^2 \tag{4.8}$$

To avoid convergence to a local minimum and reduce the computation cost/time, we define a search range of [ΔL_0-min{ λ_k }/2, ΔL_0+ min{ λ_k }/2], where ΔL_0 is the initial guess of the optical path length:

$$\Delta L_0(x,y)=\frac{1}{2\pi\cdot(K-1)}\sum_{k=2}^{K}\left[\phi_k(x,y)-\phi_{k-1}(x,y)\right]\cdot\frac{\lambda_k\lambda_{k-1}}{\lambda_{k-1}-\lambda_k} \tag{4.9}$$

where the total number of wavelengths (K) is typically ~5-10. Within this search interval, we scan the values to find the optical path length $\Delta L_{opt}(x,y)$ that minimizes the cost function, resulting in an unwrapped object phase image.

Computation platform used for super-resolved image reconstructions

Our reconstructions are performed using MATLAB (Version R2012a, MathWorks, Massachusetts, USA) on a desktop computer equipped with 3.60-GHz central processing unit (Intel Xeon E5-1620) and 16 GB random-access memory. For a 1×1 mm^2 sub-region with an upsampling factor of seven, one iteration of our wavelength scanning super-resolution routine takes ~1.2 seconds. As an example, one cycle of our algorithm, which goes through all the undersampled measurements (e.g., 7 wavelengths for each angle/height, and 22 angles/heights in total), takes ~3 minutes. In our proof-of-concept implementation, the iterations did not use either GPU (graphics processing unit) or parallel computing, which could significantly improve our

overall computation time[90]. The total image reconstruction time could be further improved when the algorithm is implemented using C language, rather than MATLAB.

4.3 Results and discussion

The physical basis for wavelength scanning pixel super-resolution is the strong wavelength dependency of the undersampled interference patterns in coherent or partially coherent diffraction imaging systems such as lensfree, holographic microscopy (Figure 4.1) or defocused lens-based imaging systems. When illuminated at slightly different wavelengths, the high frequency interference fringes due to object scattering will change, also changing the undersampled output of the image sensor chip (Figure 4.1b). Our derivations (see the Materials and Methods Section) show that, in the spatial frequency domain the aliasing signal caused by pixel induced undersampling is modulated by a complex transfer function whose phase is rather sensitive to even small wavelength changes, which makes it possible to use wavelength diversity within a narrow spectral range (i.e. ~10-30 nm) to cancel out the spatial aliasing term and enhance the resolution of the reconstructions beyond the pixel pitch.

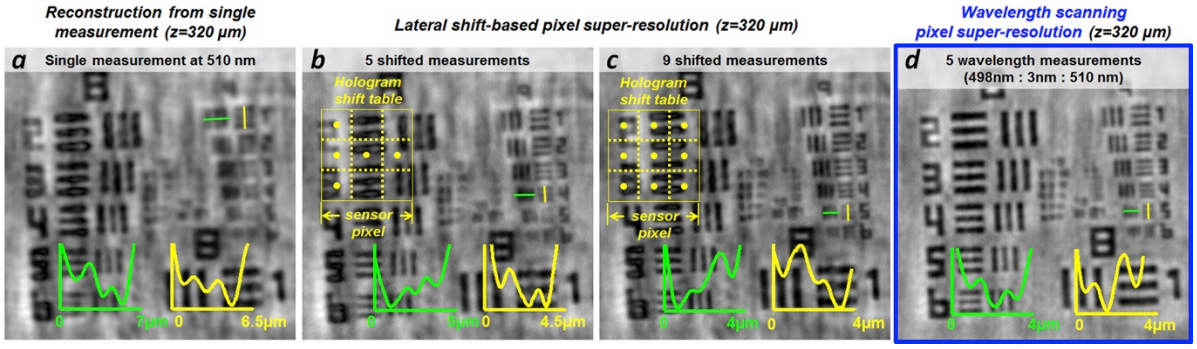

Figure 4.3. Resolution improvement brought by wavelength scanning pixel super-resolution. **(a)** Reconstruction from a single raw measurement captured by a 1.12 μm pixel pitch image sensor chip. **(b)** and **(c)**: Lensfree reconstructions using *lateral shift-based* pixel super-resolution. (b) and (c) are reconstructed using super-resolved holograms synthesized from five and nine sub-pixel shifted raw measurements, respectively. The corresponding sub-

pixel shifts of the raw measurements are marked within the hologram shift tables. **(d)** Reconstruction using wavelength scanning pixel super-resolution; 5 wavelengths are used with a scanning range of 498-510 nm and a scan step size of 3 nm.

This spatial resolution improvement brought by our wavelength scanning pixel super-resolution technique for different lensfree imaging configurations is demonstrated very well in Figures 4.3, 4.4 and 4.5.

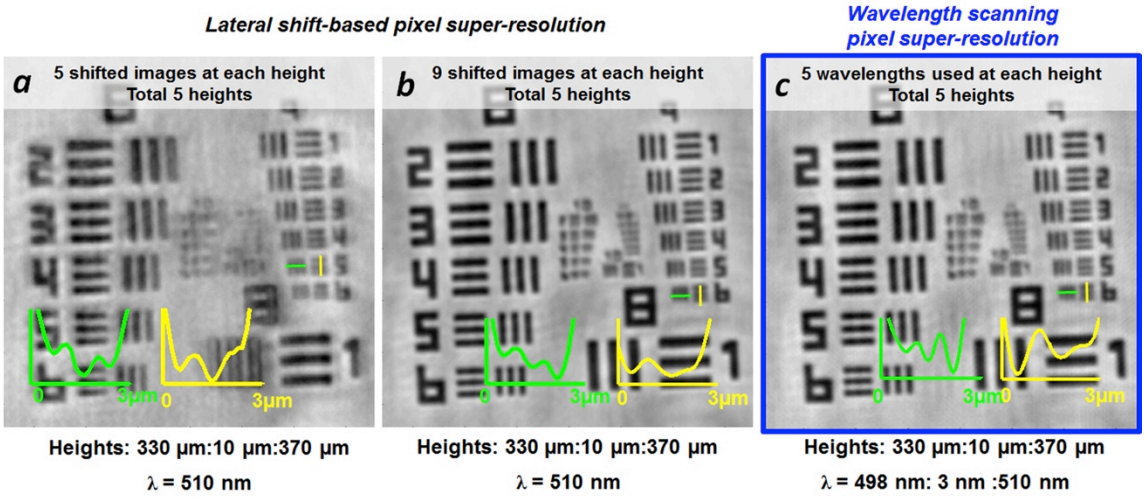

Figure 4.4. Lensfree imaging using multi-height phase retrieval and wavelength scanning pixel super-resolution. Five heights are used in each case shown in (a-c). **(a)** and **(b)** are lensfree reconstructions using *lateral shift-based* pixel super-resolution and multi-height phase retrieval. **(a)** uses five and **(b)** uses nine sub-pixel shifted raw measurements at each height. **(c)** Lensfree reconstruction using wavelength scanning pixel super-resolution and multi-height phase retrieval; 5 wavelengths are used with a scanning range of 498-510 nm and a scan step size of 3 nm.

Without pixel super-resolution, lensfree microscopy with a unit magnification on-chip imaging geometry (where the sample FOV equals to the sensor-chip's active area) can achieve a half-pitch resolution close to the image sensor's pixel pitch (i.e., ~1 μm in Figure 4.3a, using a CMOS sensor that has 1.12 μm pixel pitch). For the same configuration depicted in Figure 4.3,

utilizing the wavelength diversity in illumination boosts the half-pitch resolution to ~0.6 μm by using five different wavelengths between 498 and 510 nm (see Figures 4.3c-d). When integrated with the multi-height phase retrieval technique[128,129], the resolution can be further improved to ~0.5 μm, corresponding to an effective NA of ~0.5 (Figure 4.4). Using the synthetic aperture technique[130], however, can provide not only twin image elimination, but also a significant increase in spatial bandwidth of the reconstructed images, which enables us to take full advantage of wavelength scanning based pixel super-resolution technique and achieve a half-pitch resolution of ~250 nm with an effective NA of ~1.0 under a unit magnification geometry, where the FOV is >20 mm^2 (see Figure 4.5). These results clearly demonstrate pixel super-resolution capabilities of our wavelength scanning approach.

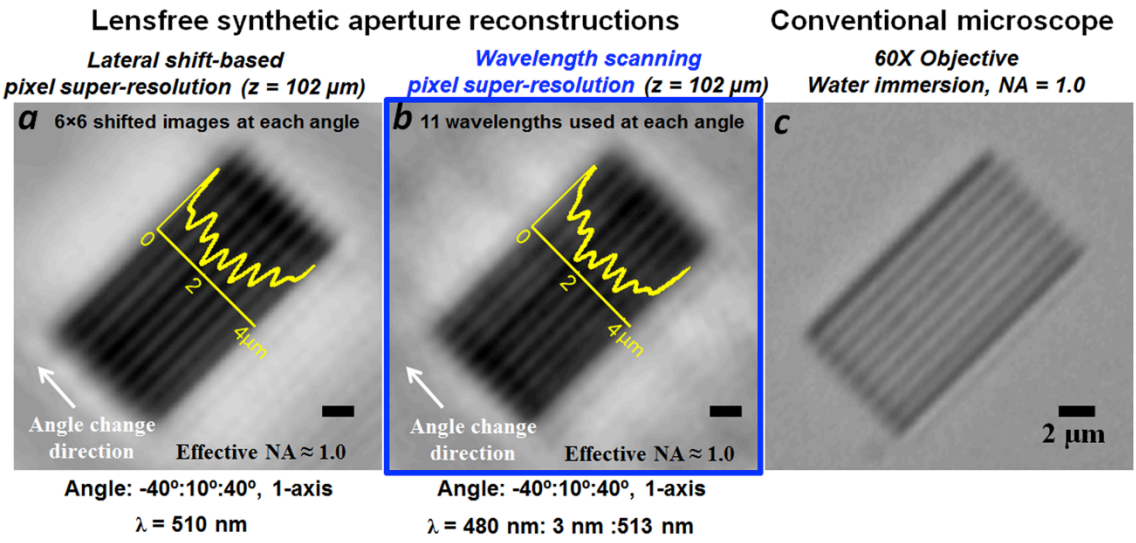

Figure 4.5. **(a)** Lensfree imaging using synthetic aperture and lateral shift-based pixel super-resolution. At each illumination angle, 6×6 = 36 sub-pixel lateral shifts, which spread evenly within the pixel area, are used for super-resolution. **(b)** Lensfree imaging using synthetic aperture and wavelength scanning pixel super-resolution. 12 wavelengths are used with a scanning range of 480–513 nm and a scan step of 3 nm. The illumination angle scanning directions, ranges and scanning steps are the same in both **(a)** and **(b)**. **(c)** Image of the specimen using a conventional lens-based microscope with a 60× water-immersion objective lens (NA = 1.0).

Besides delivering a competitive resolution and NA, the wavelength scanning based super-resolution approach also offers better data efficiency compared to lateral shift-based pixel super-resolution techniques, i.e., fewer raw measurements are needed for the same resolution improvement. In lateral shift-based pixel super-resolution, the subpixel shifts between the raw measurements are obtained by moving the light source, image sensor and/or the specimen with respect to each other[56,94,97,129], and the resolution improvement is direction dependent. Therefore, sub-pixel shifts that spread uniformly within a 2-dimensional pixel area are preferred in lateral shift-based pixel super-resolution techniques to achieve optimal resolution enhancement. As a result of this, the number of raw measurements generally increases as a quadratic function of the pixel super-resolution factor. On the other hand, in wavelength scanning super-resolution approach, the resolution improvement due to wavelength diversity is uniform in all lateral directions across the sensor array, which enables us to achieve competitive resolution with much fewer raw measurements compared to lateral shift shift-based super-resolution. To exemplify this important advantage of our approach, in a normal-illumination configuration, compared with lateral shift technique which needs nine measurements to achieve a half-pitch resolution of ~0.6 μm (Figure 4.3b and 4.3c), it only takes wavelength scanning technique five raw measurements (Figure 4.3d) to reach the same imaging performance. Similarly, when combined with multi-height phase retrieval[128,129], wavelength scanning super-resolution needs 25 raw measurements in total (five wavelengths at each of five heights) which is significantly smaller than the amount needed using lateral shifts (i.e., 45 raw measurements as shown in Figure 4.4). When integrated with synthetic aperture based lensfree imaging[130], an even higher spatial resolution can be achieved using wavelength diversity and the advantages of wavelength scanning over lateral shifts become more significant. As shown in Figure 4.5, to achieve a half-pitch resolution of

~250 nm in all lateral directions, lateral shift-based super-resolution approach takes 36 raw measurements at each illumination angle, while the wavelength scanning approach needs only 12 raw measurements to achieve the same resolution improvement. This important advantage in terms of reduced number of measurements can be translated into shorter imaging times and smaller data storage space, which are critical for increasing the speed and utility of high-resolution wide-field imaging techniques.

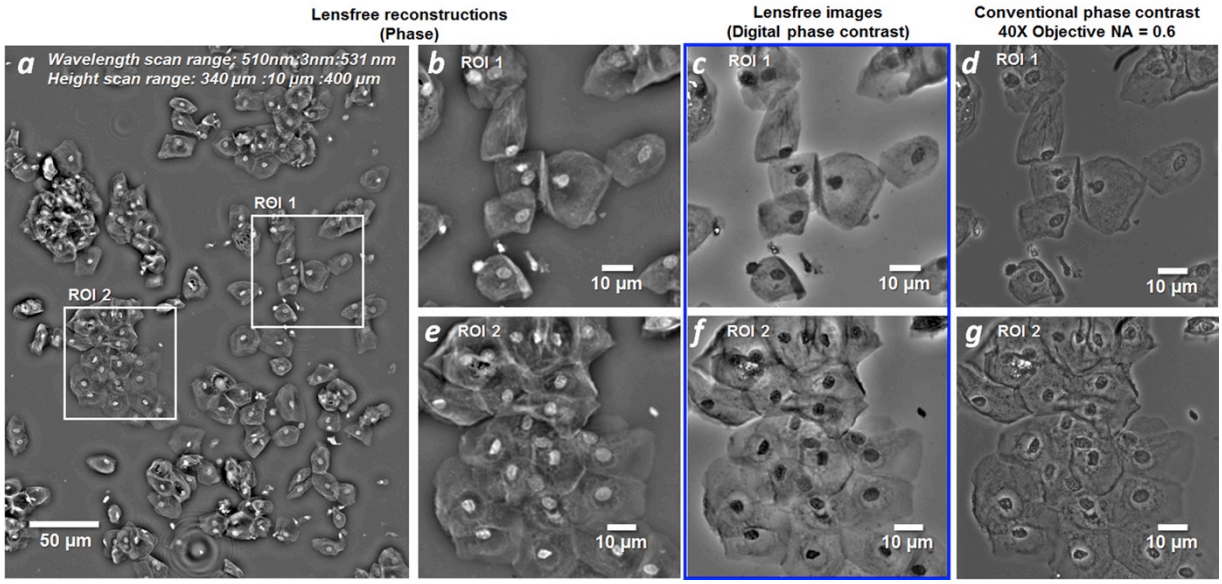

Figure 4.6. Lensfree imaging of a Papanicolaou (Pap) smear using wavelength scanning pixel-super resolution and multi-height phase retrieval. **(a)** Super-resolved lensfree phase image of the Pap smear. Wavelength scanning range: 510-531 nm, scanning step: 3 nm. **(b)** and **(e)** show regions-of-interest (ROI) No. 1 and 2, respectively. **(c)** and **(f)**: digital phase contrast images generated from lensfree reconstructions (refer to the Materials and Methods Section for details). **(d)** and **(g)**: Conventional lens-based phase contrast images obtained using a 40x objective lens (NA = 0.6).

We should re-emphasize that wavelength scanning super-resolution only requires a few wavelengths taken from a narrow spectral range (e.g. ~10-30 nm). With this new super-resolution approach, we can obtain high-resolution amplitude reconstructions of not only colorless but also colored (i.e., stained/dyed) samples without further modifications in our

reconstruction algorithm. We demonstrated this capability by imaging various biological samples, including unstained Pap smears (Figure 4.6) as well as stained blood smears (Figure 4.7). Since our lensfree reconstructions provide both amplitude and phase channels, we can also visualize the reconstructed images using different methods to create e.g., a digital phase contrast image[125,130] as illustrated in Figure 4.6.

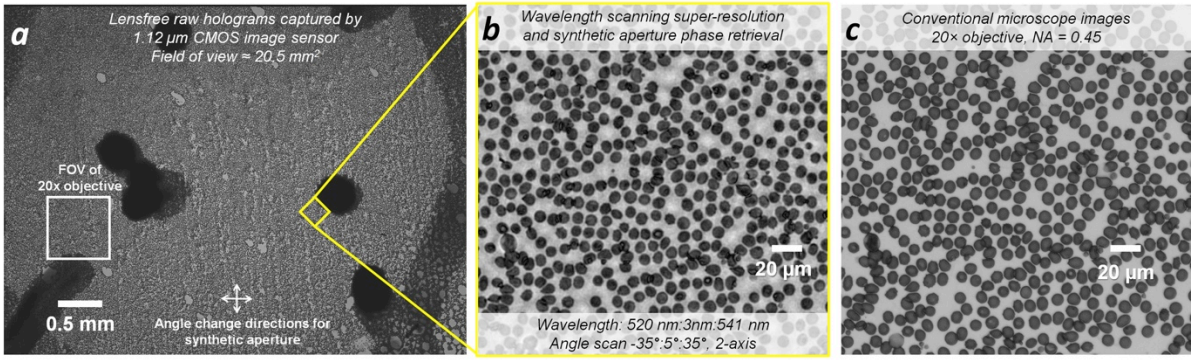

Figure 4.7. Lensfree imaging of a blood smear using wavelength scanning pixel super-resolution and synthetic aperture phase retrieval. Wavelength scanning range: 520-541 nm, scanning step: 3 nm. Angle scanning (two axis) range: -35° to 35° with 5° steps. **(a)** Lensfree raw hologram captured using a 1.12 µm pixel CMOS image sensor with a FOV of ~20.5 mm^2. **(b)** Lensfree reconstruction of a sub-region, marked with a yellow square within the full FOV. **(c)** Conventional lens-based microscope image using a 20x objective lens (NA = 0.45).

Besides significantly improving the resolution and mitigating undersampling, wavelength diversity also enables us to perform robust phase unwrapping and reveal the optical path length differences between the specimen and surrounding medium. The retrieved phase reconstruction from a single wavelength is constrained to its principle value ($-\pi$, π], and therefore large optical path length differences can cause polarity errors that may not be corrected even using state-of-the-art phase unwrapping algorithms[151–154] (see e.g., Figures 4.8a-b). Such polarity errors in phase reconstructions can also be mitigated by detecting the phase differences between the reconstructions at two different wavelengths[150,159]. However, this two-wavelength phase

unwrapping approach still faces the challenge of ambiguity or uniqueness[159]. In addition to achieving pixel super-resolution, we further utilized wavelength scanning to significantly improve the robustness of phase unwrapping by incorporating all the wavelengths of illumination that are used in pixel super-resolution to unwrap the reconstructed phase (see the Materials and Methods Section). Our phase unwrapping results shown in Figures 4.8c,f clearly illustrate that through optimization we can entirely rule out incorrect optical path length differences within our reconstructed images and achieve robust phase unwrapping at a super-resolved image.

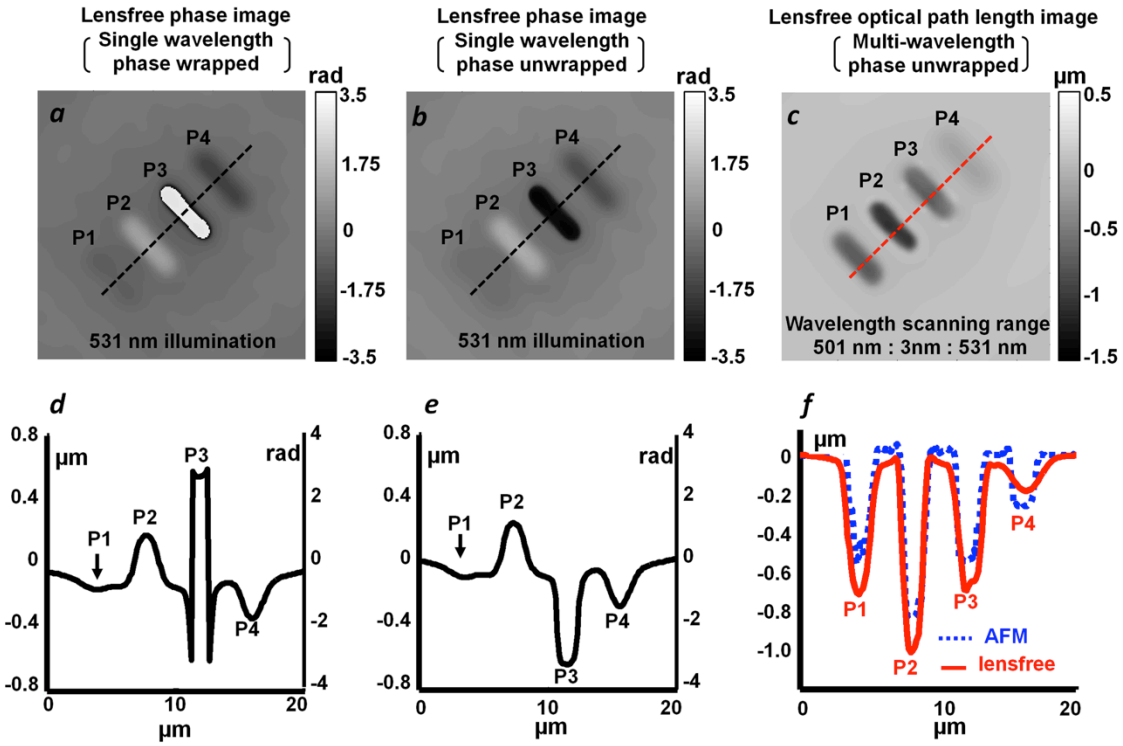

Figure 4.8. Phase unwrapping using multiple wavelengths. The sample consists of four grating lines carved into a glass substrate using focused ion beam milling. **(a)** Lensfree phase image using a single wavelength; phase map is wrapped. **(b)** Unwrapped lensfree phase image from a single wavelength reconstruction using a 2D phase unwrapping technique that is based on minimum network flow[153]. **(c)** Unwrapped lensfree phase image using reconstructions from multiple wavelengths. 11 wavelengths are used with a scanning range of 501-531 nm and a scan step size of 3 nm. Refer to the Materials and Methods Section for further details on multi-wavelength phase

unwrapping. **(d) (e)** and **(f)**: depth profiles of **(a)**, **(b)** and **(c),** respectively. The blue dashed line in **(f)** is the depth profile of the sample gratings measured using an atomic force microscope (AFM).

Wavelength scanning pixel super-resolution approach, together with phase retrieval methods, including multi-height[128,129], synthetic aperture[130], and object support based techniques[60,94,96], could constitute high-resolution imaging systems with greatly improved imaging speed. For a bench-top system, high-speed wavelength scanning can be realized using a fast tunable source (employing e.g., an acousto-optic tunable filter with a supercontinuum source) synchronized with the image sensor chip. Compared with lateral shift-based super-resolution setups, such a combination avoids motion blur, and could bring the data acquisition speed up to the maximum frame rate of the image sensor. Furthermore, the lateral shifts generated by source-shifting approach[94,97,128,130] are determined by both the sample-to-sensor and sample-to-aperture distances, which can make it challenging to generate optimized lateral shifts for samples at different vertical heights. Wavelength scanning approach, on the other hand, is performed with evenly distributed wavelengths regardless of the sample height. Therefore, we believe that wavelength scanning pixel super-resolution is more favorable over lateral shifting techniques for building high-resolution wide-field microscopes with high imaging speeds. Additionally, better data efficiency of our wavelength scanning super-resolution approach can reduce the cost of data storage and transmission, benefiting telemedicine implementations and server-based remote reconstructions.

Besides delivering competitive results on a bench top system, the presented wavelength scanning pixel super-resolution approach also has great potential for field-portable microscopy applications. Compared to lateral shift-based pixel super-resolution, wavelength scanning approach does *not* require any mechanical motion or fiber bundle[94,96], which could make the

mobile imaging platform more robust. Since the wavelength scanning range is narrow (i.e., ~10-30 nm), the combination of a few light-emitting diodes (LEDs), each with a standard spectral bandwidth of ~15-30 nm and a variable optical thin-film filter to narrow down the LED spectra will be sufficient to implement wavelength scanning super-resolution in a field portable and cost-effective design.

Finally, we should emphasize that the presented wavelength scanning pixel super-resolution approach, in addition to lensfree or holographic diffraction based imaging systems, can also be applied to lens-based point-to-point imaging modalities. By introducing a simple defocus into a lens-based imaging system (by e.g., a relative axial shift of the sensor array, object and/or the objective lens) the entire wavelength diversity framework described in this manuscript would be able to achieve pixel super-resolution. For proof-of-concept, as shown in Fig. 4.9, we demonstrated our wavelength scanning pixel super-resolution on a conventional lens-based microscope. A 10× objective (NA=0.3) with a 3.75-μm pixel size CMOS sensor is used. Originally the half-pitch resolution of the microscope is ~0.8 μm (corresponding NA of ~0.3 and) with a small FOV of ~0.17 mm^2. We expanded the FOV to ~1.20 mm^2 by adding a ×0.35 camera adaptor, which makes the imaging system pixel size-limited. To bring the resolution back to the resolving capability of the objective lens, we defocused the lens to a distance of 160 μm – 300 μm with 20 μm step size. The wavelength scanning range is from 500 nm to 521 nm with 3 nm step size. We captured the diffraction patterns at these different wavelengths and focal distances, and reconstructed the image using the same two-stage algorithms that has been described in Materials and Methods Section. The result in Fig. 4.9c and 4.9d shows that, wavelength scanning pixel super-resolution successfully boosted the resolution back to the resolving capability of objective lens while expanding the FOV by ~7 folds. The simple

implementation confirms again that our wavelength scanning pixel super-resolution technique is broadly applicable to various coherent and partially coherent wide-field imaging modalities.

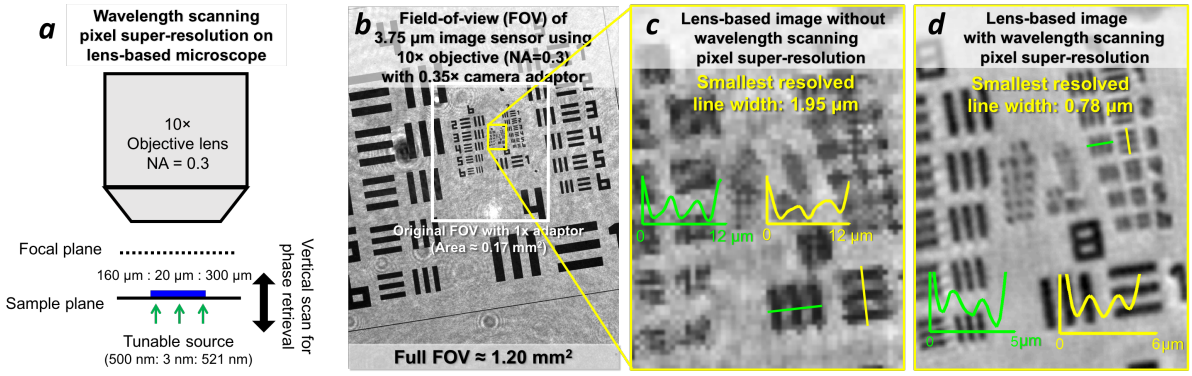

Figure 4.9. Implementation of wavelength scanning pixel super-resolution on a lens-based microscope. **(a)** schematic of the optical setup. In the proof-of-concept system, a 10× objective lens with NA of 0.3 is used. The sample plane is scanned from160 μm to 300 μm from the focal plane of the objective lens at a 20 μm step size. The wavelength of the plane wave illumination is tuned between 500 nm and 521 nm with 3 nm step size. **(b)** full field-of-view of a 3.75 μm CMOS image sensor (1280×960 pixels) using a 10× objective lens with a ×0.35 (×0.38 after calibaration) camera adaptor; **(c)** lensbased image of the resolution test chart without wavelength scanning pixel super-resolution. The line width of the smallest resolved feature is 1.95μm. **(d)** lensbased image of the resolution test chart without wavelength scanning pixel super-resolution. The line width of the smallest resolved feature is 0.78 μm.

4.4 Conclusions

We reported a new wavelength scanning based pixel super-resolution technique, which generates high-resolution reconstructions from undersampled raw measurements captured at multiple wavelengths within a narrow spectral range (i.e., 10-30 nm). Compared with lateral shift-based super-resolution, this wavelength scanning method avoids the need for shifting mechanical components and more importantly, brings uniform resolution improvement along all

the directions across the image sensor or sample plane. This framework enabled us to improve the resolution and effective NA of a wide-field lensfree microscope by a factor of ~4, achieving a half-pitch resolution of 250 nm with an NA of ~1.0 using significantly fewer measurements compared to lateral shift-based super-resolution methods. Since this wavelength scanning super-resolution technique utilizes a narrow spectral range, it permits super-resolved imaging of both colorless (e.g., unstained) and stained/dyed biological samples. Reconstructions at multiple wavelengths also enable robust phase unwrapping to reveal the optical path length differences between the specimens and surrounding media. This new wavelength scanning super-resolution approach would broadly benefit various wide-field microscopy applications that require large space-bandwidth products.

Chapter 5 Propagation phasor approach in lensfree microscopes

Parts of this chapter have been accepted for publication and is currently in print: W. Luo, A. Greenbaum, Y. Zhang, and A. Ozcan, Propagation phasor approach for holographic image reconstruction, Scientific Reports (2016).

5.1 Introduction

High-resolution wide-field optical imaging is needed in various fields, especially in medical and engineering applications that demand large space-bandwidth-products. Originally invented for electron microscopy[160], holography has become an emerging solution for high-resolution and wide-field digital imaging. The concept of holography relies on reconstructing the image of a specimen using interference patterns created by the diffracted object fields, which can be recorded and digitized even without the use of any lenses. Recent advances in digital holographic microscopy have largely benefited from the rapid evolution of e.g., the opto-electronic sensor technology and computing power[161], which have led to the development of various new imaging configurations and reconstruction techniques[162–173,60,97,174–177,90,94,178,179,128,56,96,180,181,98,57,129,182–184].

Generally speaking, in-line holographic imaging modalities, where the diffracted object field and the reference wave co-propagate along the same direction are more susceptible to twin-image noise that arises due to the loss of the optical phase or intensity-only spatial sampling at the sensor chip. Although off-axis holography offers a robust solution for this phase retrieval problem by using an angled reference wave, it sacrifices the space-bandwidth-product of the imaging system. For wide-field implementations of high-resolution holographic microscopy, another limitation is posed by pixelation of the holograms since high magnification optics (e.g., objective lenses) or fringe magnification in the form of large distance wave propagation would

both result in a significant reduction in the imaging volume and the field-of-view of the microscope.

Previously, these challenges of spatial aliasing (i.e., undersampling) and twin image noise in digital holography have been addressed by pixel super-resolution and phase retrieval techniques, implemented sequentially to reconstruct images of the specimen with ultra-large space-bandwidth-products[56,97,185,186]. Conventional pixel-super resolution relies on digital synthesis of high spatial frequency content of the sample using multiple low-resolution measurements that are recorded at different sub-pixel displacements between the image sensor and object planes[62,69,70,90,94,97,121,187]. Using this mathematical framework, high-resolution (i.e., super-resolved) holograms can be obtained, and then used for digital phase retrieval. To retrieve the lost optical phase in an in-line imaging geometry, multiple super-resolved holograms can be utilized at e.g., different sample-to-sensor distances[128,185,186,46], illumination angles[182], or illumination wavelengths[145,146,188,189]. Each one of these holograms essentially serve as independent physical constraints on the amplitude of the optical field, which enables the use of an iterative algorithm to force the complex object field to be consistent with all these measurements[46,100,101,185,186]. Although this sequential implementation of pixel super-resolution followed by phase retrieval has enabled digital holographic microscopy to deliver high-resolution and wide-field reconstructions with giga-pixel level throughput, they currently require large amounts of holographic data. For instance, in a multi-height configuration (i.e., using multiple sample-to-sensor distances)[128,185,186,46], if 4×4 pixel super-resolution is implemented at eight different heights, the total number of raw holograms to be captured becomes 128, which could be a limitation for e.g., high-speed imaging applications.

Here, we present a new computational method, termed as *propagation phasor approach*, which for the first time, combines pixel super-resolution and phase retrieval techniques into a unified mathematical framework, and enables new holographic image reconstruction methods with significantly improved data efficiency, i.e., using much less number of raw measurements to obtain high-resolution and wide-field reconstructions of the specimen. Based on our analytical derivations, the twin image noise and spatial aliasing signals, along with other digital holographic artifacts, can be interpreted as noise terms modulated by digital *phasors*, which are all analytical functions of the imaging parameters including e.g., the lateral displacement between the hologram and the sensor array planes, sample-to-sensor distance, illumination wavelength, and the angle of incidence. Based on this new *propagation phasor approach*, we devised a two-stage holographic image reconstruction algorithm that merges phase retrieval and pixel super-resolution into the same unified framework. Compared to previous holographic reconstruction algorithms, our new method reduces the number of raw measurements by five to seven fold, while at the same time achieving a competitive spatial resolution across a large field-of-view.

Based on the same propagation phasor framework, we also created two new digital methods to achieve pixel super-resolution using (1) the diversity of the sample-to-sensor distance (i.e., multi-height based pixel super-resolution), and (2) the diversity of the illumination angle (i.e., multi-angle based pixel super-resolution). We demonstrated the success of these methods by imaging biological specimens such as Papanicolaou and blood smears. We believe that with its significantly improved data efficiency, this new propagation phasor based approach could be broadly applicable to increase the space-bandwidth-product of various digital holographic microscopy systems.

5.2 Materials and methods

Optical setup for holographic imaging

Fig. 5. 1a depicts our configuration of an in-line holographic imaging system: the coherent or partially coherent incident light first impinges on the specimen, the directly-transmitted light and the scattered light then interfere at an image sensor chip, which samples and digitizes the intensity of this interference pattern. To demonstrate our propagation phasor approach for holographic image reconstruction, we selected to implement it using lensfree holographic microscopy although it is broadly applicable to other holographic microscopy platforms.

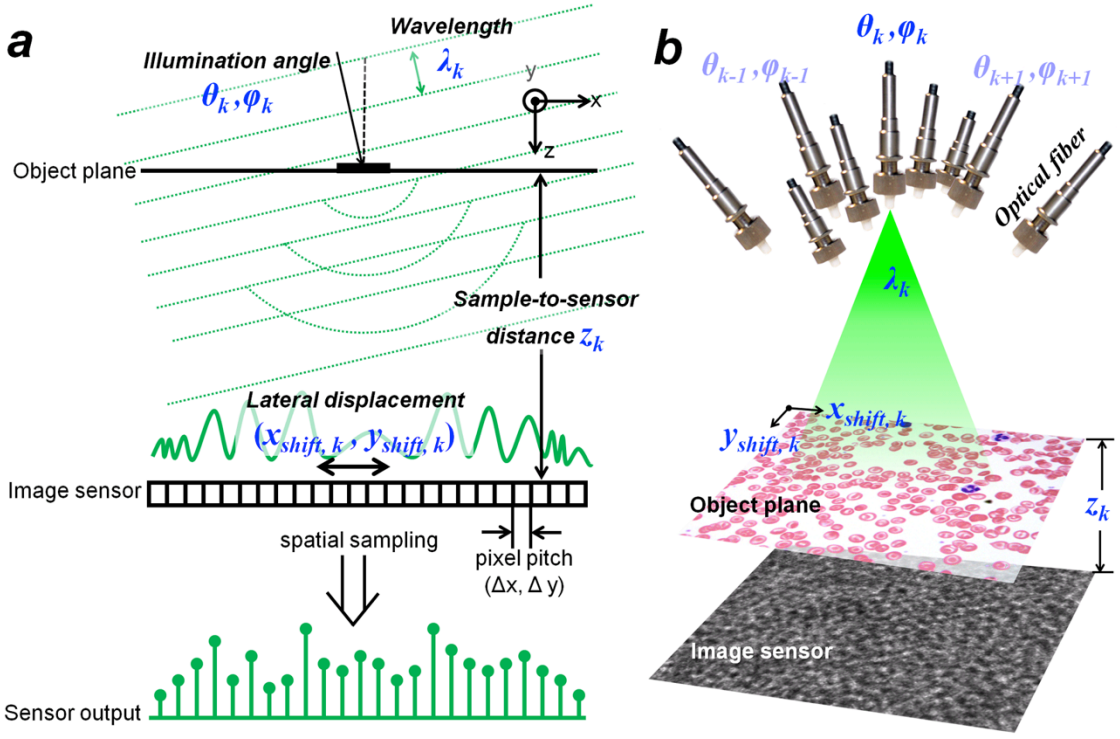

Figure 5.1. (a) Configuration of an in-line holographic imaging system. Some of the controllable parameters of the imaging system are marked in blue color, including the illumination angle (θ_k and φ_k), wavelength λ_k, sample-to-sensor distance z_k, and the lateral displacements between the hologram and the image sensor planes ($x_{shift,\,k}$ and $y_{shift,\,k}$). **(b)** Schematic of the optical setup of a lensfree on-chip holographic microscope.

As depicted in Fig. 5. 1b, our lensfree holographic microscope includes three parts: a fiber-coupled wavelength-tunable light source (WhiteLase-Micro, model VIS, Fianium Ltd, Southampton, UK), an image sensor chip (IU081, Sony Corporation, Japan), and a thin specimen mounted above the sensor chip. The optical fiber's outlet is placed at e.g. ~10 cm away from the sample whereas the sample-to-sensor distance is typically 0.1-1 mm and thus the illumination at the object plane can be considered as a plane wave. By bringing sample close (sub-mm) to an image sensor chip, lensfree on-chip holography allows the utilization of the image sensor active area as the object field-of-view, creating a unit magnification in-line holographic imaging system, where the spatial resolution and field-of-view can be independently controlled and adjusted by the pixel design and the number of pixels, respectively[190]. The fiber optic cable is mounted on a rotational arm (PRM1Z8, Thorlabs, New Jersey, USA) that can move across a dome above the specimen so that the incidence light can also be adjusted to an arbitrary angle. The rotational arm is loaded on a mechanical linear stage that moves in lateral directions to introduce sub-pixel displacements between the hologram and the image sensor-array. The specimen is held by a piezo-driven positioning stage (MAX606, Thorlabs, New Jersey, USA), which can move vertically to change the distance between the sample and the image sensor chip. During the holographic data acquisition, the tunable source, the mechanical stages, and the image sensor chip are all automated and coordinated by a PC running a custom-written LabVIEW program (Version 2011, National Instruments, Texas, USA).

Sample preparation

Besides a standard 1951 USAF resolution test target, we also demonstrated the success of our propagation phasor approach by imaging biological samples, including unstained Papanicolaou

(Pap) smear slides and blood smears. Pap smears are prepared using ThinPrep® method (Hologic, Massachusetts, USA). The blood smear samples are prepared using EDTA (ethylenediaminetetraacetic acid) anticoagulated human blood and stained with Wright's Stain[155].

5.3 Mathematical formalism of propagation phasor approach in digital holography

In this sub-section we present the concept of propagation phasors by deriving the analytical expressions that contain not only the holographic information of the specimen, but also the twin image noise, spatial aliasing signal, and upsampling related spatial artifacts. In this manuscript, we use lower case letters to represent the functions in spatial domain, and the upper case letters for functions in spatial frequency domain. Throughout our analysis, we assume a plane wave illumination as also supported by our imaging set-up, Fig. 5. 1. The transfer function of the optical system between the specimen and the image sensor plane can be written as $h_k(x,y,z_k,\lambda_k,\theta_k,\varphi_k)$, where x and y are the lateral coordinates at the sensor plane, z_k is the vertical sample-to-sensor distance, λ_k is the illumination wavelength, and (θ_k, φ_k) defines the angle of incidence. The subscript k denotes different imaging configurations, achieved by e.g., vertically moving the specimen or sensor chip to record the holograms at different sample-to-sensor distances z_k, changing the illumination wavelength λ_k, or tilting the illumination beam to change the angle of incidence, θ_k and φ_k. One additional pair of variables in our imaging configuration is the lateral displacements between the image sensor and the object planes, i.e., $x_{shift,\ k}$ and $y_{shift,\ k}$, see Fig. 5. 1a. Such sub-pixel displacements are utilized as one way of mitigating the spatial undersampling at the image sensor chip due to a large pixel size.

Under these different imaging configurations, each labeled with index k, the transmission properties of a two-dimensional (2D) specimen can be generally expressed as

$o_k(x,y) = 1 + s_k(x,y)$, where s_k refers to the scattered object field that interferes with the background unscattered light. The frequency spectrum $O_k(f_x, f_y)$ of $o_k(x,y)$ can be written as:

$$O_k(f_x, f_y) = \delta(f_x, f_y) + S_k(f_x, f_y) \tag{5.1}$$

Similarly, we can write the 2D spatial frequency spectrum of the transfer function $h_k(x, y, z_k, \lambda_k, \theta_k)$ as:

$$H_k(f_x, f_y, z_k, \lambda_k, \theta_k) \equiv FT\{h_k(x, y, z_k, \lambda_k, \theta_k)\} \tag{5.2}$$

where FT refers to the Fourier Transform operation. From now on, we will simplify the expressions of all the frequency spectra in our equations by hiding the spatial frequency variables f_x, and f_y. The frequency spectrum of the field intensity $i_k(x,y)$ on the image sensor plane can then be expressed as:

$$I_k = \delta + T_k \cdot S_k + (T_k^- \cdot S_k^-)^* + SS_k \tag{5.3}$$

where '$\cdot$' represents the multiplication operation, the superscript '-' represents using variable set ($-f_x$, $-f_y$) instead of (f_x, f_y) and the asterisk stands for complex conjugate operation. SS_k represents the self-interference terms, which can be written as $SS_k = \Gamma_{f_x, f_y}\{H_k \cdot S_k\}$, where Γ_{f_x, f_y} refers to the autocorrelation operation. T_k is determined by the transfer function H_k, i.e.,:

$$T_k = H_k^*(f_{x,k}, f_{y,k}) \cdot H_k \tag{5.4}$$

where $f_{x,k} = n_k \cdot \sin\theta_k \cdot \cos\varphi_k / \lambda_k$, $f_{y,k} = n_k \cdot \sin\theta_k \cdot \sin\varphi_k / \lambda_k$, and n_k is the refractive index of the medium, which is assumed to be a function of only the illumination wavelength. It is important to notice that H_k is a complex function with a unit magnitude, defining a *phasor*[66]. Based on Eq. (4), as a product of $H_k^*(f_{x,k}, f_{y,k})$ and H_k, the function T_k is also a *phasor*, and

we term T_k as a ***propagation phasor***, the function of which in our reconstruction framework will be more clear later on.

When any intensity distribution $i_k(x,y)$ is sampled by an image sensor-array with a pixel pitch of Δx and Δy in lateral directions, the discrete Fourier transform (DFT) of the sensor's output can be expressed as:

$$I_{sampled,\,k} = \sum_{u,v=0,\pm1,\pm2,} I_k(f_x - \frac{u}{\Delta x}, f_y - \frac{v}{\Delta y}) \cdot P_k(f_x - \frac{u}{\Delta x}, f_y - \frac{v}{\Delta y}) \tag{5.5}$$

In Eq. (5.5) u and v are integers representing the aliasing orders, and $(u, v) = (0, 0)$ denotes the non-aliased *target* signal of the object. $P_k(f_x, f_y)$ is the 2D FT of the pixel function that defines the responsivity distribution within each pixel of the image sensor chip[98]. Originally, f_x, and f_y in Eq. (5.5) are discrete frequency values confined within the Nyquist window. Based on the periodic nature of DFT, Eq. (5.5) and all of our further derivations can be numerically extended to a broader frequency domain by simply upsampling the raw measurements. Therefore, without change of notations, $I_{sampled,\ k}$ refers to the DFT of the *upsampled* version of our raw measurements.

Now we will incorporate the lateral displacements between the holograms and the image sensor chip into Eq. (5.5). If we add lateral shifts ($x_{shift,\,k}$, $y_{shift,\,k}$) to each hologram, then Eq. (5.5) can be re-written as:

$$I_{sampled,\,k} = \sum_{u,v=0,\pm1,\pm2,} I_{uv,\,k} \cdot P_{uv,\,k} \cdot e^{-j\phi_{shift,\,uv,\,k}} \tag{5.6}$$

where we simplify the expression of spatial aliasing order by using the subscript uv, and $\phi_{shift,\,uv,\,k}$ represents the phase change caused by a lateral shift:

$$\phi_{shift,\,uv,\,k} = 2\pi[(f_x - \frac{u}{\Delta x}) \cdot x_{shift,\,k} + (f_y - \frac{v}{\Delta y}) \cdot y_{shift,\,k}] \tag{5.7}$$

In Eq. (5.6), by replacing the expression of $I_{uv,\,k}$ with Eq. (5.3), we can obtain an expanded expression for $I_{sampled,\,k}$:

$$I_{sampled,\,k} = \sum_{u,v=0,\pm1,\pm2,} [\delta_{uv} + T_{uv,\,k} \cdot S_{uv,\,k} + (T^{-}_{uv,\,k} \cdot S^{-}_{uv,\,k})^{*} + SS_{uv,\,k}] \cdot P_{uv,\,k} \cdot e^{-j\phi_{shift,\,uv,\,k}} \tag{5.8}$$

On the right side of Eq. (5.8), we can see that, for each aliasing order (i.e., each combination of *u* and *v*, including the target signal: *u*=0, *v*=0), there are four items inside the square brackets. *The first item, δ_{uv}, represents the background light, the second item, $T_{uv,\,k} \cdot S_{uv,\,k}$, represents the real image, the third item, $(T^{-}_{uv,\,k} \cdot S^{-}_{uv,\,k})^{*}$, represents the twin image; and the last item, $SS_{uv,\,k}$, is the self-interference term*.

Next, we will present a generic, two-stage holographic reconstruction algorithm using propagation phasors, which aims to recover the object term $\delta_{00} + S_{00,\,k}$ from a series of measured holograms.

Stage I of Propagation Phasor based Holographic Reconstruction: Generation of an Initial Guess

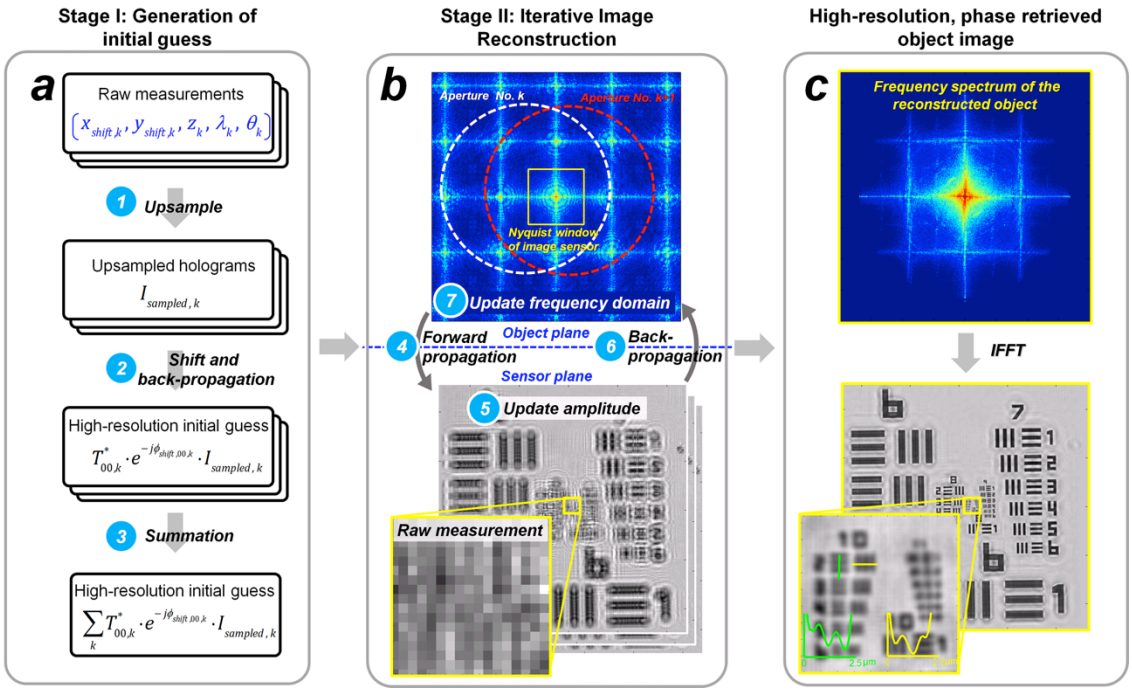

Figure 5.2. Propagation phasor approach-based holographic image reconstruction. **(a)** Stage I: generation of an initial guess. **(b)** Stage II: iterative image reconstruction. **(c)** High-resolution, phase retrieved reconstruction of the object.

As depicted in Fig. 5. 2, the first stage of the reconstruction is to generate a high-resolution initial guess of the specimen, and this *Stage I* is composed of three steps (i.e., Steps 1-3 in Fig. 5. 2).

- Step 1: Upsampling of each raw measurement serves as the first step in our holographic reconstruction algorithm. This upsampling factor, although does not introduce any new information, should be large enough to expand the expression of $I_{sampled,\ k}$ to cover the entire passband of the optical system. Since the computation cost of the reconstruction increases quadratically with the upsampling factor, it should also be limited to avoid unnecessary computational burden/time. For our lensfree microscopy platform reported here, we typically set an upsampling factor of ≤ 7.

- Step 2: The second step of the holographic reconstruction is to offset the lateral displacements $x_{shift,\,k}$, and $y_{shift,\,k}$, and then perform back-propagation on the upsampled raw measurements. To do so, we multiply both sides of Eq. (5.8) with $T^{*}_{00,\,k}\cdot e^{j\phi_{shift,\,00,\,k}}$ and reorganize the terms to extract the true object signal, i.e., the target signal:

$$\begin{aligned}(\delta_{00}+S_{00,\,k})\cdot P_{00,\,k} = {} & T^{*}_{00,\,k}\cdot e^{j\phi_{shift,\,00,\,k}}\cdot I_{sampled,\,k} \\ & - T^{*}_{00,\,k}\cdot T^{-*}_{00,\,k}\cdot P_{00,\,k}\cdot S^{-*}_{00,\,k} \\ & - \sum_{u\neq 0,v\neq 0} T^{*}_{00,\,k}\cdot T_{uv,\,k}\cdot e^{j(\phi_{shift,\,00,\,k}-\phi_{shift,\,uv,\,k})}\cdot P_{uv,\,k}\cdot S_{uv,\,k} \\ & - \sum_{u\neq 0,v\neq 0} T^{*}_{00,\,k}\cdot T^{-*}_{uv,\,k}\cdot e^{j(\phi_{shift,\,00,\,k}-\phi_{shift,\,uv,\,k})}\cdot P_{uv,\,k}\cdot S^{-*}_{uv,\,k} \\ & - \sum_{u\neq 0,v\neq 0} T^{*}_{00,\,k}\cdot e^{j(\phi_{shift,\,00,\,k}-\phi_{shift,\,uv,\,k})}\cdot P_{uv,\,k}\cdot \delta_{uv} \\ & - \sum_{u,v} T^{*}_{00,\,k}\cdot e^{j(\phi_{shift,\,00,\,k}-\phi_{shift,\,uv,\,k})}\cdot P_{uv,\,k}\cdot SS_{uv,\,k}\end{aligned} \tag{5.9}$$

On the left side of Eq. (5.9), we have kept the pixel function $P_{00,\,k}$ multiplied with $\delta_{00}+S_{00,\,k}$; note, however, that it can be later removed using deconvolution techniques as the last step of the holographic reconstruction[98]. The right side of Eq. (5.9) shows that in order to extract $(\delta_{00}+S_{00,\,k})\cdot P_{00,\,k}$, there are five terms that need to be eliminated from the back-propagated intensity (i.e., $T^{*}_{00,\,k}\cdot e^{j\phi_{shift,\,00,\,k}}\cdot I_{sampled,\,k}$). The first term, $T^{*}_{00,\,k}\cdot T^{-*}_{00,\,k}\cdot P_{00,\,k}\cdot S^{-*}_{00,\,k}$, represents the *twin image noise*; the second and third terms which contain $S_{uv,\,k}$ or $S^{-*}_{uv,\,k}$ ($u\neq 0,\ v\neq 0$) represent the *spatial aliasing signals* for real and twin images, respectively; the fourth term with δ_{uv} ($u\neq 0,\ v\neq 0$) is the *high frequency artifacts* generated during the upsampling process. The last term with $SS_{uv,\,k}$ is the *self-interference signal*.

- Step 3: Summation of all the upsampled and back-propagated holograms $T^{*}_{00,\,k}\cdot e^{j\phi_{shift,\,00,\,k}}\cdot I_{sampled,\,k}$ to generate an initial guess. This initial summation can greatly suppress

the twin image noise, aliasing signal and other artifact terms outlined above in Step 2. To better explain the impact of this summation step, we can simplify the expression of the phasor terms in Eq. (5.9) as:

$$\begin{aligned}(\delta_{00}+S_{00,\,k})\cdot P_{00,\,k} \approx\; & T^{*}_{00,\,k}\cdot e^{j\phi_{shift,\,00,\,k}}\cdot I_{sampled,\,k} - \; Q^{twin}_{00,\,k}\cdot P_{00,\,k}\cdot S^{-*}_{00,\,k} \\ & - \sum_{u\neq 0, v\neq 0} Q^{real}_{uv,\,k}\cdot P_{uv,\,k}\cdot S_{uv,\,k} - \sum_{u\neq 0, v\neq 0} Q^{twin}_{uv,\,k}\cdot P_{uv,\,k}\cdot S^{-*}_{uv,\,k} \\ & - \sum_{u\neq 0, v\neq 0} Q^{artifact}_{uv,\,k}\cdot P_{uv,\,k}\cdot \delta_{uv} - \sum_{u,v} Q^{artifact}_{uv,\,k}\cdot P_{uv,\,k}\cdot SS_{uv,\,k}\end{aligned} \tag{5.10}$$

where $Q^{twin}_{k} = T^{*}_{00,\,k}\cdot T^{-*}_{00,\,k}$, $Q^{real}_{uv,\,k} = T^{*}_{00,\,k}\cdot T_{uv,\,k}\cdot e^{j(\phi_{shift,\,00,\,k}-\phi_{shift,\,uv,\,k})}$, $Q^{twin}_{uv,\,k} = T^{*}_{00,\,k}\cdot T^{-*}_{uv,\,k}\cdot e^{j(\phi_{shift,\,00,\,k}-\phi_{shift,\,uv,\,k})}$, and $Q^{artifact}_{uv,\,k} = T^{*}_{00,\,k}\cdot e^{j(\phi_{shift,\,00,\,k}-\phi_{shift,\,uv,\,k})}$. Here, $Q^{twin}_{00,\,k}$, $Q^{real}_{uv,\,k}$, $Q^{twin}_{uv,\,k}$ and $Q^{artifact}_{uv,\,k}$ are also *phasors* with unit amplitudes, and their phases change as a function of all the imaging parameters (i.e., z_k, λ_k, θ_k, φ_k, $x_{shift,\,k}$, and $y_{shift,\,k}$), see e.g., Figs. 3-4.

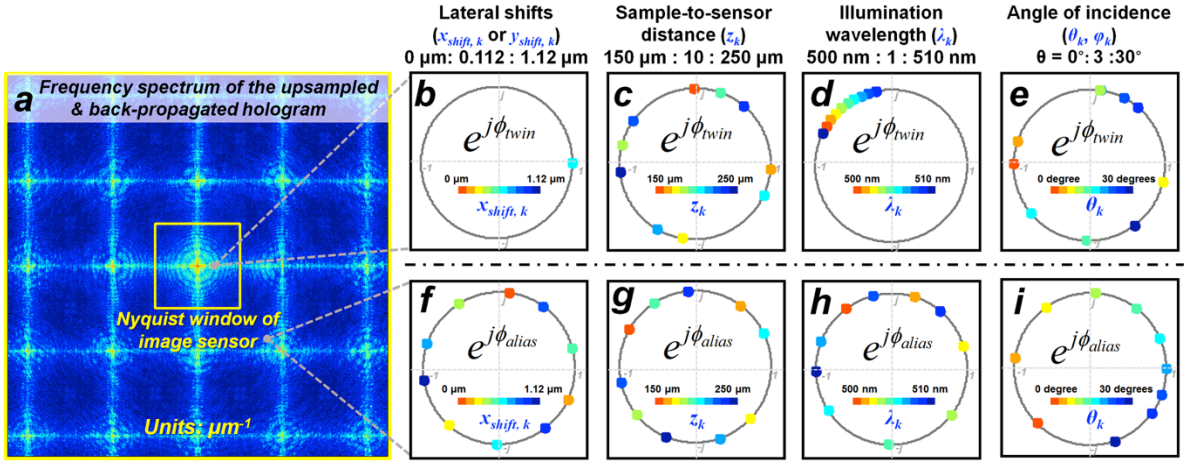

Figure 5.3. Examples of propagation phasor values as a function of various imaging parameters. **(a)** The frequency spectrum of an upsampled and back-propagated hologram. To give examples, we probe the values of the ***twin image phasor*** at (f_x=0.1 μm^{-1}, f_y=0 μm^{-1}) as shown in **(b)**, **(c)**, **(d)**, **(e)** and the ***spatial aliasing phasor*** at (f_x=0.8 μm^{-1}, f_y=-0.8 μm^{-1}) as shown in **(f)**, **(g)**, **(h)**, **(i)**. In each subfigure, we scan one of the imaging parameters while keeping all the others constant, and plot the values of the phasors in color-coded points on the unit circle. The first row shows the twin image phasor values as a function of **(b)** the lateral shifts between the hologram and the image sensor-array,

$x_{shift,\,k}$ and $y_{shift\,k}$, **(c)** the sample to sensor-distance, z_k, **(d)** the illumination wavelength, λ_k, and **(e)** the illumination angle θ_k. Similarly, the second row shows the spatial aliasing phasor values as a function of **(f)** $x_{shift,\,k}$ and $y_{shift\,,\,k}$, **(g)** z_k, **(h)** λ_k, and **(i)** θ_k.

Also notice that except the illumination wavelength λ_k, the changes of the imaging parameters z_k, θ_k , φ_k, $x_{shift,\,k}$, and $y_{shift,\,k}$ do not affect the transmission properties of the 2D specimen. During the imaging process, we confine the illumination wavelengths within a narrow spectral range, typically less than 10 nm, so that the transmission properties of the specimen and the image sensor's pixel function can be approximately considered identical when generating an initial guess of the object, i.e., $S_{uv,\,k} \approx S_{uv}$, and $P_{uv,\,k} \approx P_{uv}$. If we list Eq. (5.10) for all the possible K imaging conditions (e.g., as a function of various illumination wavelengths, sub-pixel shifts, etc.), and then sum them up with a set of weighting factors, $\{c_k\}$, we can have:

$$\begin{aligned}\left(\sum_{k=1}^{K} c_k\right)(\delta_{00}+S_{00})\cdot P_{00} \approx \sum_{k=1}^{K} c_k \cdot T^{*}_{00,\,k}\cdot e^{j\phi_{shift,\,00,\,k}}\cdot I_{sampled,\,k} - \left(\sum_{k=1}^{K} c_k \cdot Q^{twin}_{00,\,k}\right)\cdot P_{00}\cdot S^{-*}_{00} \\ - \sum_{u\neq 0,v\neq 0}\left(\sum_{k=1}^{K} c_k \cdot Q^{real}_{uv,\,k}\right)\cdot P_{uv}\cdot S_{uv} - \sum_{u\neq 0,v\neq 0}\left(\sum_{k=1}^{K} c_k \cdot Q^{twin}_{uv,\,k}\right)\cdot P_{uv}\cdot S^{-*}_{uv} \\ - \sum_{u\neq 0,v\neq 0}\left(\sum_{k=1}^{K} c_k \cdot Q^{artifact}_{uv,\,k}\right)\cdot P_{uv}\cdot \delta_{uv} - \sum_{u,v}\left(\sum_{k=1}^{K} c_k \cdot Q^{artifact}_{uv,\,k}\cdot SS_{uv,\,k}\right)\cdot P_{uv}\end{aligned} \tag{5.11}$$

By finding a set of weighting factors $\{c_k\}$ that satisfy $\sum_{k=1}^{K} c_k \cdot Q^{twin}_{uv,k} = 0$ ($u, v = 0, \pm 1, \pm 2.$); $\sum_{k=1}^{K} c_k \cdot Q^{real}_{uv,k} = 0$ ($u \neq 0, v \neq 0$); $\sum_{k=1}^{K} c_k \cdot Q^{artifact}_{uv,\,k} = 0$ ($u \neq 0, v \neq 0$); and $\sum_{k=1}^{K} c_k \neq 0$, we can have "*complete elimination"* of the twin image noise, aliasing signals and upsampling related spatial artifacts, while still maintaining the target object function, $(\delta_{00}+S_{00})\cdot P_{00}$. However, considering the fact that $Q^{twin}_{uv,\,k}$, $Q^{real}_{uv,\,k}$ and $Q^{artifact}_{uv,\,k}$ are also functions of spatial frequencies (f_x, f_y), it is

computationally expensive to obtain a set of ideal $\{c_k\}$ values. Therefore we adopt an alternative strategy as shown in Fig. 5. 2 to create our initial object guess and set all $\{c_k\}$ values to 1, and directly sum up the upsampled and back-propagated holograms, $T^*_{00,k} \cdot e^{j\phi_{shift,00,k}} \cdot I_{sampled,k}$. After this summation, the left side of Eq. (5.11) becomes $K \cdot (\delta_{00} + S_{00}) \cdot P_{00}$, while on the right side, the summations of the phasors $Q^{twin}_{uv,k}$, $Q^{real}_{uv,k}$ and $Q^{artifact}_{uv,k}$ follow:

$$\left|\sum_{k=1}^{K} Q^{twin}_{uv,k}\right| \le K, \quad \left|\sum_{k=1}^{K} Q^{real}_{uv,k}\right| \le K, \quad \left|\sum_{k=1}^{K} Q^{artifact}_{uv,k}\right| \le K \tag{5.12}$$

In fact, as illustrated in Fig. 5. 3, with proper selection of the imaging configuration, the summations of these phasors can be significantly smaller than *K*. This implies that, by simply summing up Eq. (5.11) for all *K* imaging configurations, the twin image noise (S^{-*}_{00}), aliasing signals ($S_{uv,k}$ and $S^{-*}_{uv,k}$, $u \neq 0, v \neq 0$) and upsampling related artifacts ($Q^{artifact}_{uv,k}$) can be significantly suppressed in comparison with the target signal $(\delta_{00} + S_{00}) \cdot P_{00}$. Therefore, we consider a simple summation as a good *initial guess* of the specimen at this Stage I of our propagation phasor based holographic reconstruction approach, i.e.,

$$(\delta_{00} + S_{00,initial}) \cdot P_{00} \equiv \frac{1}{K} \sum_{k=1}^{K} T^*_{00,k} \cdot e^{j\phi_{shift,00,k}} \cdot I_{sampled,k} \tag{5.13}$$

This initial guess is then used as the input to an iterative algorithm (*Stage II*) to reconstruct and refine the object function/image, which will be detailed in the next sub-section.

Stage II of Propagation Phasor based Holographic Reconstruction: Iterative Image Reconstruction

Using the initial guess defined by Eq. (5.13), we next implement an iterative process as the second stage of our propagation phasor based holographic reconstruction algorithm to eliminate the remaining twin image noise, aliasing signal, and the upsampling related artifacts. Each iteration of *Stage II* is comprised of four steps (i.e., Steps 4 through 7 - see Fig. 5. 2):

- Step 4: Based on the parameters of each illumination condition, (i.e., z_k, λ_k, θ_k, φ_k), we apply a phase modulation on the initial guess of the specimen, defined by Eq. (5.13), and propagate the field from the object plane to the image sensor using the angular spectrum approach[66]. For this wave propagation, we use the free space transfer function:

$$H_k(f_x, f_y) = \begin{cases} \exp\left[j2\pi \frac{n_k \cdot z_k}{\lambda_k} \sqrt{1 - \left(\frac{\lambda_k}{n_k} f_x\right)^2 - \left(\frac{\lambda_k}{n_k} f_y\right)^2} \right] & (f_x^2 + f_y^2 \le \left(\frac{n_k}{\lambda_k}\right)^2) \\ 0 & \text{else} \end{cases} \quad (5.14)$$

We term the wave propagation from the object plane to the image sensor as forward-propagation, and denote the spatial form of the forward-propagated field as $g_{forward,\ k}(x,\ y)$. Note that the Fresnel transform based digital wave propagation can also be used at this step, although for high-resolution imaging applications the angular spectrum approach is more suitable without any low NA approximations.

- Step 5: On the image sensor plane, we use the raw measurements (i.e., the low-resolution, undersampled holograms) to update the amplitude of the high-resolution, forward-propagated field $g_{forward,\ k}(x,\ y)$. To do so, we first convolve the intensity of the field, $|\ g_{forward,\ k}(x,\ y)|^2$, with the pixel function of the image sensor[98], and shift the convolved intensity by an amount of ($x_{shift,\ k}$, $y_{shift,\ k}$) to compensate the corresponding lateral displacement. Next, this shifted intensity is downsampled to the same resolution as the raw measurement, and the difference between this downsampled intensity and the raw measurement is considered as a low-resolution correction

map. In order to apply this low-resolution correction map to each shifted intensity, we upsample this correction map by taking its Kronecker product with the pixel function, and add the upsampled correction map to the shifted intensity with a relaxation factor (typically ~0.5). Then this 'corrected' intensity is deconvolved with the pixel function using Wiener deconvolution, and shifted back in place by the amount of ($-x_{shift,\,k}$, $-y_{shift,\,k}$). The Wiener filter takes into account the measured noise level of the image sensor to avoid over-amplification of noise during each iteration. We then use the square root of the deconvolved and shifted intensity to replace the amplitude of $g_{forward,\,k}(x, y)$, while keeping its phase *unaltered*.

- Step 6: Back-propagate the amplitude-updated, high-resolution field to the object plane, and remove the phase modulation caused by the illumination angle.

- Step 7: The back-propagated field is then used to update the transmitted field on the object plane. Different from Step 6, this update on the object plane is carried out in the spatial frequency domain. The spatial frequency region for this update is a circular area centered at $f_{x,\,k} = n_k \cdot \sin\theta_k \cdot \cos\varphi_k / \lambda_k$, $f_{y,\,k} = n_k \cdot \sin\theta_k \cdot \sin\varphi_k / \lambda_k$, and we choose the radius of the circle so that all the spatial frequencies within it experience less than 3dB amplitude attenuation during wave propagation. This update in the spatial frequency domain is also smoothened using a relaxation factor of ~0.5. In other words, the updated frequency region is the weighted sum of the old transmitted field and the back-propagated field, and the weighting factor (i.e., relaxation factor) for the back-propagated field is ~0.5. After this update, we convert the phase of the field into an optical path length map of the object, and the amplitude of the field gives us the object's final transmission image, i.e., reconstruction. Note that for relatively thick specimen, phase unwrapping needs to be performed before converting the reconstructed phase into an optical path length[184].

These above outlined steps (Steps 4 to 7) are performed for every imaging configuration. It is considered as one iteration cycle when all the K raw measurements are used for once. Similar to the convergence condition defined in Ref. [157], we determine the convergence of our iterations and the reconstruction when the sum-squared error (SSE_{avg}^{itr}) between the raw measurement and the downsampled intensity map satisfies the following criterion:

$$\left| SSE_{avg}^{itr} - SSE_{avg}^{itr-1} \right| < \varepsilon \tag{5.15}$$

where '*itr*' is the index of the iteration cycle, and ε is the convergence constant, empirically defined as ~0.2% of SSE_{avg}^{itr}.

Computation platform used for propagation phasor based holographic reconstructions

For proof-of-concept implementation, our propagation phasor approach based reconstruction algorithm has been implemented using MATLAB (Version R2012a, MathWorks, Massachusetts, USA) on a desktop computer with 3.60-GHz central processing unit (Intel Xeon E5-1620) and 16 GB random-access memory. Using an upsampling factor of seven, the computation time of one iteration in reconstruction *Stage II* (detailed in the previous sub-section) is ~1.2 seconds for a region-of-interest of ~1×1 mm^2. As for the total computation time including *Stages I* and *II*, assuming that the number of intensity distribution updates is ~8-10 per iteration (see e.g. Figs. 5b,d and Figs. 6b,d), and that the convergence can be reached within ~6-7 iteration cycles, the total image reconstruction time ranges between ~1-1.5 minutes per 1 mm^2. More than 85% of this computation time is spent on wave propagation between the sample and the image sensor planes, which heavily relies on Fast Fourier Transforms (FFTs). Therefore, the adoption of graphic processing units (GPUs) or other parallel computing architectures could significantly reduce the total computation time[90].

5.4 Results and discussion

The main challenges of wide field-of-view, high-resolution holographic imaging include: (1) phase retrieval, and (2) mitigating the undersampling caused by an image sensor chip. *The propagation phasor approach of this manuscript relies on the fact that in the digital hologram of a specimen, the twin image noise and spatial aliasing signals vary under different imaging configurations*. Such variations enable us to eliminate these unwanted noise terms (twin image noise and aliasing signal) and obtain phase-retrieved and high-resolution (i.e., super-resolved) reconstructions of the object. The imaging configuration in a holographic microscope can in general be changed by varying different parameters: (1) the lateral displacements between the holograms and the sensor-array (i.e., lateral relative shifts $x_{shift,\,k}$ and $y_{shift,\,k}$), (2) the sample-to-sensor distance (z_k), (3) the illumination wavelength (λ_k), and (4) the angle of incidence (θ_k, φ_k). In this section, to better illustrate the inner workings of our propagation phasor approach, we will first demonstrate the dependencies of the twin image noise and the aliasing signal on these controllable imaging parameters and then explore and summarize the combinations of these imaging parameters that can create phase-retrieved and high-resolution reconstructions while also improving the data efficiency of holographic imaging.

Dependency of Twin Image Noise and Aliasing Signal on Imaging Parameters

From Eq. (5.10), we can see that all the terms which need to be eliminated from an upsampled and back-propagated hologram $T^{*}_{00,\,k} \cdot e^{j\phi_{shift,\,00,\,k}} \cdot I_{sampled,\,k}$ are modulated by phasors, including: (1) the twin image term, modulated by $Q^{twin}_{00,\,k}$; (2) aliasing signals, modulated by $Q^{real}_{uv,\,k}$ and $Q^{twin}_{uv,\,k}$, $u\neq 0$, $v\neq 0$); (3) upsampling artifacts (δ_{uv} terms modulated by $Q^{artifact}_{uv,\,k}$, $u\neq 0$, $v\neq 0$); and (4) self-

interference patterns ($SS_{uv,\,k}$ terms modulated by $Q_{uv,\,k}^{artifact}$). From the perspective of our propagation phasor approach, we desire that the phasors that modulate these unwanted noise terms or artifacts exhibit sufficient variations across [0, 2π], so that they can be significantly suppressed during the initial summation in the reconstruction Stage I (detailed in the Methods Section). In this manuscript, we focus our discussion on twin image phasor $Q_{00,\,k}^{twin}$ and aliasing related phasors $Q_{uv,\,k}^{real}$, $Q_{uv,\,k}^{twin}$, ($u\neq0$, $v\neq0$), where the conclusions would be broadly applicable to a wide range of holographic imaging systems (lens-based or lensfree). Meanwhile, the self-interference patterns/artifacts are much weaker in signal strength compared to the holographic interference terms and can be easily suppressed by the iterative reconstruction algorithm (Stage II) that is detailed in the Methods Section.

To illustrate the dependencies of the twin image noise and the aliasing signal on the holographic imaging parameters, we choose the twin image phasor $e^{j\phi_{twin}} \equiv Q_{00,\,k}^{twin}$ and one of the spatial aliasing phasors, i.e., $e^{j\phi_{alias}} \equiv Q_{uv,\,k}^{real}$ (u=1, v=1), as examples and visualize them as a function of the imaging parameters ($x_{shift,\,k}$, $y_{shift,\,k}$, z_k, λ_k, θ_k, and φ_k) as shown in Fig. 5. 3. In each sub-figure of Fig. 5. 3, we only change one of the imaging parameters while keeping all the others constant. For instance, in Fig. 5. 3b that shows $e^{j\phi_{twin}}$, we only change the lateral shift $x_{shift,\,k}$ from 0 μm to 1.12 μm (i.e., the pixel pitch of the image sensor chip used in our experiments) with a step size of ~0.11 μm, while the other parameters are fixed at z_k=150 μm, λ_k=500 nm, θ_k=0°, and φ_k=0°. Similarly, Fig. 5. 3c through Fig. 5. 3e depict $e^{j\phi_{twin}}$ as a function of z_k, λ_k, and θ_k separately, while Fig. 5. 3g through Fig. 5. 3i show $e^{j\phi_{alias}}$ as a function of $x_{shift,\,k}$, z_k, λ_k, and θ_k, respectively.

From Figs. 3b-i we can see that, except the twin image phasor's *insensitivity* to lateral shifts, the diversity of all the other imaging parameters can cause both the twin image phasor and the aliasing phasors to be modulated. To better illustrate these phasors' sensitivities to various imaging parameters, we calculated in Fig. 5. 4 the partial derivatives of ϕ_{twin} and ϕ_{alias} with respect to $x_{shift,\,k}$, $x_{shift,\,k}$, z_k, λ_k, θ_k, and φ_k. Next we will analyze the values of these partial derivatives along the f_x axis (i.e., f_y=0), and summarize each imaging parameter's effect on ϕ_{alias} and ϕ_{alias} (see Figs. 4a-h).

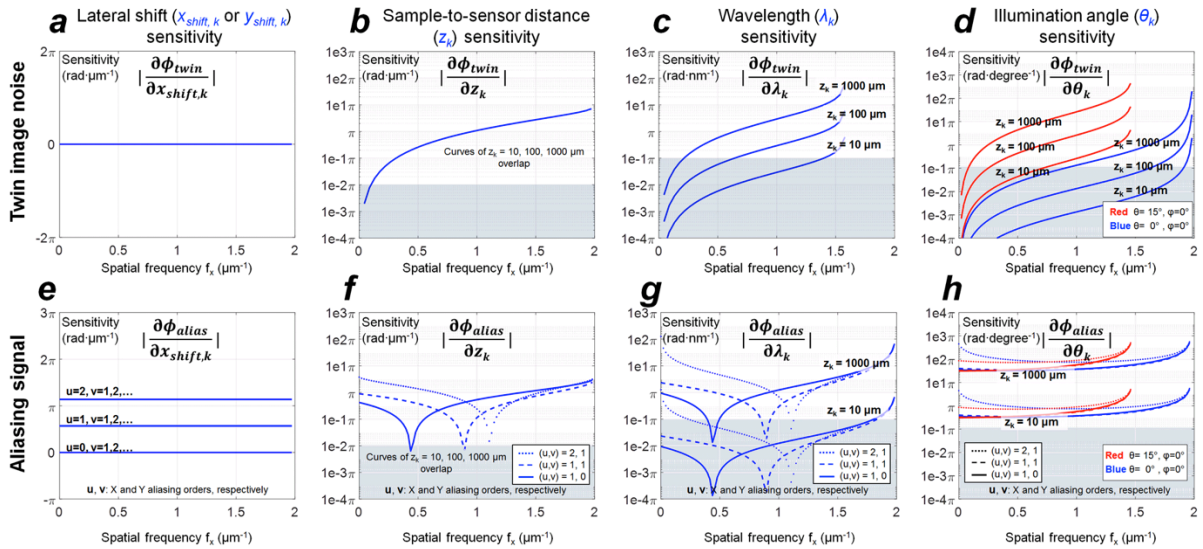

Figure 5.4. Sensitivity of propagation phasors to various imaging parameters. The first row: the partial derivatives of the twin image phasor's angle (Φ_{twin}) with respect to **(a)** the lateral shifts $x_{shift,\,k}$ and $y_{shift,\,k}$, **(b)** the sample-to-sensor distance z_k, **(c)** the illumination wavelength λ_k, and **(d)** the illumination angle θ_k. The second row: the partial derivatives of the twin image phasor's angle (Φ_{alias}) with respect to **(e)** $x_{shift,\,k}$ and $y_{shift,\,k}$, **(f)** z_k, **(g)** λ_k, and **(h)** θ_k.

- Lateral shifts* ($x_{shift,\,k}$, $y_{shift,\,k}$):** Since the twin image phasor $e^{j\phi_{twin}} \equiv Q_{00,\,k}^{twin} \equiv T_{00,\,k}^{*} \cdot T_{00,\,k}^{-*}$ (see Eq. 4) does not contain variables $x_{shift,\,k}$ or $y_{shift,\,k}$, the absolute value of its partial derivatives with respect to $x_{shift,\,k}$ and $y_{shift,\,k}$ is zero, i.e., $\left|\partial\phi_{twin}/\partial x_{shift,\,k}\right| = 0$ and $\left|\partial\phi_{twin}/\partial y_{shift,\,k}\right| = 0$ (Fig. 5. 4a). In other words, lateral shifts do *not* introduce any variations in the twin image noise term as a result of which they are not directly useful for twin image elimination or phase retrieval. On the other hand, as illustrated in Fig. 5. 4e, when spatial aliasing exists in either x or y direction (i.e., $u \neq 0$, $v \neq 0$), we then have $\left|\partial\phi_{alias}/\partial x_{shift,\,k}\right| > 0$ and $\left|\partial\phi_{alias}/\partial y_{shift,\,k}\right| > 0$, which suggests that $x_{shift,\,k}$ and $y_{shift,\,k}$ introduce linear phase modulations (see Eq. 7) in the spatial aliasing phasor term. This linear relationship between ϕ_{alias} and ($x_{shift,\,k}$, $y_{shift,\,k}$) makes the lateral shifts ideal choice for aliasing signal elimination. As shown in the Supplementary Materials, if we set the lateral shifts to be *evenly* distributed within one pixel pitch, where $x_{shift,\,k} \in \{m/(M \cdot \Delta x) \,|\, m = 1, 2, \quad M\}$ and $y_{shift,\,k} \in \{n/(N \cdot \Delta y) \,|\, n = 1, 2, \quad N\}$, summing up the upsampled and back-propagated holograms (i.e., Stage I of the reconstruction algorithm detailed in the Methods Section) can lead to *complete elimination of the aliasing signals*. This summation is mathematically equivalent to back-propagating the *pixel super-resolved* holograms[98,182,121,57,127,62,69,70,97,94,56,128,129]. ***To conclude, the diversity of the lateral shifts can only contribute to the aliasing signal elimination, i.e., pixel super-resolution.

***- Sample-to-sensor distance* (z_k):** Using the diversity of the sample-to-sensor distance (z_k) to eliminate the twin image noise has been one of the most widely-used phase retrieval techniques in holographic image reconstruction[96,100,101,128,129,172,185,186]. For completeness of our discussion, here we analyze the effect of z_k on the twin image noise from the perspective of the propagation

phasor approach. As shown in Fig. 5. 4b, $\left|\partial\phi_{twin}/\partial z_k\right|$ rises as spatial frequency f_x increases. Except at very low spatial frequencies (e.g., $|f_x|$<0.1 μm^{-1}), ϕ_{twin} exhibits strong sensitivity to z_k. For example, even at $|f_x|$≈0.1 μm^{-1}, changing the sample-to-sensor distance by ~100 μm can make the twin image phasor $e^{j\phi_{twin}}$ *reverse* its polarity. This sensitivity makes z_k a *very useful variable* for twin image noise elimination. For aliasing signal elimination, as depicted in Fig. 5. 4f, we can see that ϕ_{alias} also shows a good sensitivity to z_k, i.e. $\left|\partial\phi_{alias}/\partial z_k\right| \geq 0.01\pi \cdot \mu m$ except for a very limited number of spatial frequency points. ***Therefore, besides twin image elimination, the diversity of z_k can also be used for aliasing signal elimination.***

- *Wavelength* (λ_k): The diversity of illumination wavelength can be used for twin image elimination (i.e., phase retrieval) [189,191]. We have previously reported that it can also be used for eliminating the spatial aliasing signals[184]. As shown in Fig. 5. 4c and Fig. 5. 4g, one important property of $\left|\partial\phi_{twin}/\partial\lambda_k\right|$ and $\left|\partial\phi_{alias}/\partial\lambda_k\right|$ is that they show strong dependencies on the illumination wavelength *only when* the sample-to-sensor distance z_k is large enough (e.g., z_k>~100 μm). Stated differently, by changing the illumination wavelength λ_k, the holographic interference patterns at the sensor-array will surely vary, but such variations become more pronounced and useful at larger distances, z_k. ***Therefore, in a point-to-point focused imaging system (using e.g., a lens-based imaging set-up), the diversity of wavelength is of no use for phase retrieval or resolution enhancement unless a slight defocus (i.e., z_k) is introduced in the imaging system***.

- *Angle of incidence* (θ_k, φ_k): We have previously reported the use of the diversity of illumination angles (θ_k and φ_k) for phase retrieval[94,97,182,190] as well as for expanding/improving the frequency bandwidth, i.e., the spatial resolution through a synthetic aperture approach in lensfree on-chip microscopy[182]. As shown in Figs. 4d and 4h, similar to the case of wavelength diversity, to make use of the illumination angle for phase retrieval and elimination of aliasing signal, sufficient sample-to-sensor distance (e.g., $z_k > 100$ μm) is needed. Fig. 5. 4d also suggests that, for phase retrieval, relatively large angular variations (e.g., $\Delta\theta$>10°) are preferred since $\left|\partial\phi_{alias}/\partial\theta_k\right| > 0.1\pi \cdot \text{degree}^{-1}$. Another important observation from Fig. 5. 4h is that at different illumination angles θ_k, $\left|\partial\phi_{alias}/\partial\theta_k\right|$ remains non-zero in most of the spatial frequencies, which is similar in behavior to $\left|\partial\phi_{alias}/\partial x_{shift,\,k}\right|$ as shown in Fig. 5. 4e. Intuitively, this implies that slight perturbations on the illumination angle will introduce lateral shifts of the interference patterns on the image sensor plane, which can be considered as one method of generating $x_{shift,\,k}$, and $y_{shift,\,k}$. In fact, shifting the light source by small amounts has been proven as an effective way of performing lateral shift-based pixel super-resolution in lensfree holography[90,94,97].

Therefore, both θ_k and φ_k can be used for the elimination of twin image noise and spatial aliasing signal.

The above-described contributions of various imaging parameters to eliminate twin image noise and spatial aliasing signal terms are summarized in Table 1. From Table 1 we can see that the propagation phasor approach of this manuscript: (***1***) *provides a unique mathematical formalism that combines/merges various existing phase retrieval and pixel super-resolution techniques used in digital holography into the same unified framework*, and (***2***) *creates two new techniques to eliminate the aliasing signal in digital holography, namely using the diversity of*

the sample-to-sensor distance, and the diversity of the illumination angle. For consistency with the previous used terminology, we name these two new methods as *multi-height based pixel super-resolution* and *multi-angle based pixel super-resolution*, respectively. Next, we will experimentally demonstrate the imaging results and the advantages of these two new methods.

Propagation Phasor Approach Using Multi-height and Multi-angle Holographic Data

Using this new propagation phasor based reconstruction framework, the diversities of sample-to-sensor distance or illumination angle can enable not only twin image elimination, but also resolution enhancement, i.e., super-resolution. To demonstrate the resolution enhancement brought by the diversity of z_k (i.e., multi-height based pixel super-resolution – Table 1), we captured the holograms of a standard resolution test target at eight different heights, where the values of z_k are evenly distributed between 200 μm and 305 μm with a spacing of ~ 15 μm. For comparison, we first reconstructed the specimen using a previous technique: multi-height based phase retrieval algorithm[96,128,129] (see Fig. 5a). For the same set of raw data, compared to this previous technique our propagation phasor based reconstruction delivers a half-pitch resolution improvement from ~0.87 μm to 0.69 μm, corresponding to a numerical aperture (NA) improvement from 0.3 to 0.4 (wavelength: 530 nm), see Fig. 5b.

In addition to multi-height based pixel super-resolution, a similar resolution enhancement can also be achieved using the diversity of illumination angles (i.e., multi-angle based pixel super-resolution – Table 1). As shown in Figs. 5c and 5d, we demonstrated multi-angle pixel super-resolution using the data captured from 9 different illumination angles, where one of them is vertical (0°), and rest of the angles are placed at ±15° and ±30° along two axes above the

specimen (see Fig. 1b). The half-pitch resolution improvement brought by the diversity of illumination angle is also similar: from ~0.87 μm down to 0.69 μm.

In the next sub-section we will demonstrate that much higher resolution images can be reconstructed using our propagation phasor approach by simply adding lateral shift based pixel super resolution to ***only one*** of the measurement heights or angles, which is used as an initial guess at Stage I of our reconstruction algorithm detailed in the Methods Section. As will be presented next, this approach is also quite efficient in terms its data requirement compared to existing approaches.

Improving the Data Efficiency in High-resolution Holographic Reconstructions Using the Propagation Phasor Approach

Using the multi-height imaging configuration outlined earlier, we performed 4×4 lateral shift-based pixel super-resolution at *only one* sample-to-sensor distance (i.e., ~190 μm), which added 15 extra raw measurements/holograms to the original data set that is composed of measurements at 8 heights. In our propagation phasor based reconstruction, we directly used the back-propagation of this super-resolved hologram at this height (190 μm) as our initial guess (Stage I of our algorithm – see the Methods Section). The resolution improvement that we have got by using these additional 15 raw measurements in our propagation phasor approach is significant: we achieved a half-pitch resolution of ~0.55 μm (corresponding to an NA of ~0.48 at 530 nm illumination), which is the same level of resolution that is achieved by performing lateral shift-based super-resolution *at every height* (see Fig. 6a and 6b). In other words, to achieve the same resolution level, the propagation phasor approach utilized ***5.5-fold*** less number of raw

measurements (i.e., 23 vs. 128) compared to the conventional lateral shift-based multi-height method[96,128,129].

A similar level of improvement in data efficiency of our propagation phasor approach is also observed in the multi-angle imaging configuration: by simply performing 6×6 pixel super-resolution at *only* the vertical illumination, the propagation phasor based reconstruction can achieve a half-pitch resolution of ~0.49 μm (corresponding to an NA of ~0.53 at 530 nm illumination). As a comparison, the synthetic aperture approach[182] achieves a half-pitch resolution of ~0.44 μm; however it uses 6×6 pixel super-resolution *at every* illumination angle (Fig. 6c), and therefore our propagation phasor approach (Fig. 6d) has ***7-fold*** improvement in its data efficiency (i.e., 44 vs. 324 raw measurements). This improvement and significant reduction in the number of raw measurements/holograms are especially important to make wide-field, high-resolution holographic imaging suitable for high speed applications.

Imaging Biological Samples Using the Propagation Phasor Approach

To demonstrate the success of our propagation phasor approach in imaging biological specimen, we imaged unstained Papanicolaou (Pap) smears (see Fig. 7a-d) and stained blood smears (see Fig. 7e-h). For Pap smear imaging, we captured the holograms of the specimen at multiple sample-to-sensor distances, and at each z_k, only one raw measurement is recorded. For comparison, we first reconstructed the Pap smear using a previously reported multi-height phase retrieval algorithm[96,128,129] (Fig. 7a). Using the same holographic data set and raw measurements, the reconstructions created by our propagation phasor approach (Fig. 7b) show resolution improvements compared to the previously reported method. To further improve the resolution without significantly increasing the burden of data acquisition, we added eight extra raw

measurements for shift-based pixel super-resolution (with a super-resolution factor of 3×3) at *only one* of the heights, which is used as an initial guess (in Stage I) of our reconstruction algorithm. As shown in Fig. 7c, our propagation phasor approach based reconstruction shows a good agreement with the images captured using a conventional phase contrast microscope (40× objective lens, NA = 0.6). For imaging of stained blood smears, we captured the lensfree holograms at multiple illumination angles. The comparison between Fig. 7e and Fig. 7f also confirms the resolution improvement brought by our propagation phasor based reconstruction algorithm. By adding lateral shift-based pixel super-resolution (with a super-resolution factor of 3×3) at only the vertical illumination angle (i.e., θ_k=0), we further improved the resolution of our reconstructed image (Fig. 7g), which shows comparable performance against a bright-field microscope with a 40× objective lens (NA = 0.6), Fig. 7h.

Based on these results, we confirm that our propagation phasor approach would greatly increase the speed of high-resolution and wide-field holographic microscopy tools. In previously reported holographic imaging modalities, multiple laterally shifted images are captured to achieve pixel super-resolution at every one of the sample-to-sensor distances[96,128,129] or illumination angles[182]. As demonstrated in Figs. 6 and 7, the propagation phasor approach can reduce the number of required raw holograms by five to seven fold while also achieving a competitive resolution. This reduction in raw data also lowers the need for data transmission and storage, which could further improve the cost-effectiveness of holographic imaging modalities such as handheld lensfree microscopy tools[94,96,183] for telemedicine applications.

Although our experimental demonstrations in this manuscript utilized a lensfree on-chip imaging set-up, we would like to once again emphasize that this propagation phasor approach is broadly applicable to a wide range of holographic imaging modalities, including lens-based

holographic microscopy techniques. For instance, in a lens-based undersampled holographic imaging system, multi-height pixel super-resolution can simply be achieved by capturing a series of defocused images at different heights. Considering the fact that the depth focusing operation is naturally required and performed every time a sample is loaded onto a lens-based traditional microscope, this propagation phasor approach provides a unique method to enlarge the space-bandwidth-product of the final image without compromising the image acquisition time.

5.5 Conclusions

This chapter demonstrated a propagation phasor approach for high-resolution, wide-field holographic imaging with significantly improved data efficiency. Different from previous holographic reconstruction methods, our propagation phasor approach merges phase retrieval and pixel super-resolution techniques into a unified mathematical framework, where the twin image noise, spatial aliasing signals and other digital artifacts are all interpreted as noise terms that are modulated by phasors. These propagation phasors analytically depend on and can be controlled by various imaging parameters such as the lateral displacement between the hologram and the sensor-array, sample-to-sensor distance, illumination wavelength, and the angle of incidence. We systematically investigated and summarized the sensitivities of both the twin image noise and the aliasing signal to these imaging parameters, which enabled us to establish two new super-resolution methods that utilize the diversity of the sample-to-sensor distance and the diversity of the illumination angle. Compared to previous reconstruction algorithms, this propagation phasor framework can deliver phase-retrieved reconstructions with a competitive resolution using five- to seven-fold reduced number of raw measurements/holograms, which makes it especially appealing for high speed and cost effective microscopy applications. We

further confirmed the success of this approach by imaging biological samples including unstained Papanicolaou smears and stained blood smears.

Chapter 6 Conclusions

Parts of this chapter have been previous published as journal articles including

- Greenbaum, A. W. Luo, B. Khademhosseinieh, T-W. Su, A.F. Coskun, and A. Ozcan. Increased space-bandwidth product in pixel super-resolved lensfree on-chip microscopy. Sci. Rep. 3, 1717 (2013).
- Luo W, Greenbaum A, Zhang Y, Ozcan A. Synthetic aperture-based on-chip microscopy. Light Sci Appl 2015; 4: e261.
- Luo W, Zhang Y, Feizi A, Göröcs Z, Greenbaum A, Ozcan A. Pixel super-resolution using wavelength scanning. Light Sci Appl 2015. doi:10.1038/lsa.2016.60.
- W. Luo, A. Greenbaum, Y. Zhang, and A. Ozcan, Propagation phasor approach for holographic image reconstruction, Scientific Reports (2016).

Lensfree holographic microscopy is a potent solution for high-resolution, wide-field imaging. In the pursuit of large space-bandwidth products and high data efficiency in lensfree holographic microscopy, my work can be summarized into four stages:

First, I **improved the lateral resolution by incorporating the light responsivity distribution within a single pixel into the pixel super-resolution technique**. As demonstrated in Chapter 2, this pixel super-resolution can improve the numerical aperture (NA) of the reconstructed image by a factor of ~3 compared to a raw lensfree image. This improvement factor was confirmed using two different image sensors that significantly vary in their pixel sizes, circuit architectures and digital/optical readout mechanisms. Besides the resolution improvement, such pixel count increase immediately renders our lensfree on-chip microscope into a Giga-pixel

throughput imaging platform without sacrifice in FOVs: with the 6.8 μm-pitch CCD sensor we obtained an effective pixel count of up to 2.52 Giga pixels; with the 1.12 μm-pitch CMOS sensor the effective pixel count reached up to 1.64 Giga pixels. I also demonstrated that this pixel super-resolution-based lensfree microscope, when combined with an UV LED, is capable of resolving 225 nm line-width gratings and is useful for wide-field on-chip imaging of nano-scale objects such as helical multi-walled carbon nanotubes (MWCNTs).

Second, I developed lensfree imaging using synthetic aperture (LISA) to expand the bandwidth of the imaging modality, and enables high resolution (e.g., 250 nm), across the visible spectrum. As detailed in Chapter 3, this was the first time implementation of synthetic aperture technique in lensfree on-chip imaging, and I was able to reach a record high NA of 1.4. This synthetic imaging technique also performs phase retrieval, enabling lensfree microscope to image breast cancer tissue samples stained with hematoxylin and eosin (H&E) over a very large field-of-view (>20 mm^2).

Third, I devised a fundamentally new pixel super-resolution technique using the diversity of illumination wavelength (Chapter 4). I developed an iterative algorithm to generate high-resolution reconstructions of the specimen using undersampled diffraction patterns recorded at a few wavelengths, covering a narrow spectrum (~10-30 nm). When combined with a synthetic aperture technique, this wavelength scanning super-resolution approach can achieve a half-pitch resolution of 250 nm, corresponding to a numerical aperture of ~1.0, across a large field-of-view (>20 mm^2). Compared to displacement-based super-resolution, wavelength scanning brings uniform resolution improvement in all directions across the sensor array and requires significantly less number of measurements.

Finally, I developed a propagation phasor approach. This phasor approach combines phase retrieval and pixel super-resolution into a unified mathematical framework, which enables novel holographic image reconstruction methods with significantly improved data efficiency. In this approach, twin-image and spatial aliasing signals, along with other digital artifacts, are interpreted as noise terms that are modulated by phasors that analytically depend on the lateral displacement between hologram and sensor planes, the sample-to-sensor distance, the wavelength, and the illumination angle. I systematically investigated and summarized the sensitivities of both the twin-image noise and the aliasing signal to these imaging parameters, which enabled the establishment of two new super-resolution methods that utilize the diversity of the sample-to-sensor distance and the diversity of the illumination angle. Compared to previous reconstruction algorithms, this propagation phasor framework can deliver phase-retrieved reconstructions with a competitive resolution using five- to seven-fold reduced number of raw measurements/holograms, which makes it especially appealing for high speed and cost effective microscopy applications. These technological advances could greatly help future developments of high-resolution, wide-field computational imaging modalities with compactness, cost-effectiveness and superior data efficiency.

References

1. Garcia-Sucerquia, J., Xu, W., Jericho, M. H. & Kreuzer, H. J. Immersion digital in-line holographic microscopy. *Opt. Lett.* **31,** 1211–1213 (2006).
2. Garcia-Sucerquia, J. *et al*. Digital in-line holographic microscopy. *Appl. Opt.* **45,** 836–850 (2006).
3. Kanka, M., Riesenberg, R. & Kreuzer, H. J. Reconstruction of high-resolution holographic microscopic images. *Opt. Lett.* **34,** 1162–1164 (2009).
4. Kanka, M., Riesenberg, R., Petruck, P. & Graulig, C. High resolution (NA=0.8) in lensless in-line holographic microscopy with glass sample carriers. *Opt. Lett.* **36,** 3651–3653 (2011).
5. Seo, S. *et al*. High-Throughput Lens-Free Blood Analysis on a Chip. *Anal Chem* **82,** 4621–4627 (2010).
6. Mudanyali, O. *et al*. Compact, light-weight and cost-effective microscope based on lensless incoherent holography for telemedicine applications. *Lab Chip* **10,** 1417–1428 (2010).
7. Bishara, W., Su, T.-W., Coskun, A. F. & Ozcan, A. Lensfree on-chip microscopy over a wide field-of-view using pixel super-resolution. *Opt. Express* **18,** 11181–11191 (2010).
8. Bishara, W. *et al*. Holographic pixel super-resolution in portable lensless on-chip microscopy using a fiber-optic array. *Lab Chip* **11,** 1276–1279 (2011).
9. Bishara, W., Zhu, H. & Ozcan, A. Holographic opto-fluidic microscopy. *Opt. Express* **18,** 27499–27510 (2010).
10. Mudanyali, O., Bishara, W. & Ozcan, A. Lensfree super-resolution holographic microscopy using wetting films on a chip. *Opt. Express* **19,** 17378–17389 (2011).

11. Greenbaum, A., Sikora, U. & Ozcan, A. Field-portable wide-field microscopy of dense samples using multi-height pixel super-resolution based lensfree imaging. *Lab Chip* (2012). doi:10.1039/C2LC21072J

12. Seo, S., Su, T.-W., Tseng, D. K., Erlinger, A. & Ozcan, A. Lensfree holographic imaging for on-chip cytometry and diagnostics. *Lab Chip* **9,** 777–787 (2009).

13. Greenbaum, A. & Ozcan, A. Maskless imaging of dense samples using pixel super-resolution based multi-height lensfree on-chip microscopy. *Opt. Express* **20,** 3129–3143 (2012).

14. Stybayeva, G. *et al*. Lensfree Holographic Imaging of Antibody Microarrays for High-Throughput Detection of Leukocyte Numbers and Function. *Anal Chem* **82,** 3736–3744 (2010).

15. Su, T.-W., Erlinger, A., Tseng, D. & Ozcan, A. Compact and Light-Weight Automated Semen Analysis Platform Using Lensfree on-Chip Microscopy. *Anal Chem* **82,** 8307–8312 (2010).

16. Isikman, S. O., Bishara, W., Zhu, H. & Ozcan, A. Optofluidic Tomography on a Chip. *Appl. Phys. Lett.* **98,** 161109–161109–3 (2011).

17. Isikman, S. O. *et al*. Lens-free optical tomographic microscope with a large imaging volume on a chip. *Proc. Natl. Acad. Sci.* (2011). doi:10.1073/pnas.1015638108

18. Isikman, S. O. *et al*. Field-portable lensfree tomographic microscope. *Lab Chip* **11,** 2222–2230 (2011).

19. Brady, D. J., Choi, K., Marks, D. L., Horisaki, R. & Lim, S. Compressive Holography. *Opt. Express* **17,** 13040–13049 (2009).

20. Hahn, J., Lim, S., Choi, K., Horisaki, R. & Brady, D. J. Video-rate compressive holographic microscopic tomography. *Opt. Express* **19,** 7289–7298 (2011).

21. Lee, M., Yaglidere, O. & Ozcan, A. Field-portable reflection and transmission microscopy based on lensless holography. *Biomed. Opt. Express* **2,** 2721–2730 (2011).

22. Cui, X. *et al*. Lensless high-resolution on-chip optofluidic microscopes for Caenorhabditis elegans and cell imaging. *Proc. Natl. Acad. Sci.* **105,** 10670–10675 (2008).

23. Pang, S. *et al*. Implementation of a color-capable optofluidic microscope on a RGB CMOS color sensor chip substrate. *Lab. Chip* **10,** 411–414 (2010).

24. Zheng, G., Lee, S. A., Antebi, Y., Elowitz, M. B. & Yang, C. The ePetri dish, an on-chip cell imaging platform based on subpixel perspective sweeping microscopy (SPSM). *Proc. Natl. Acad. Sci.* **108,** 16889–16894 (2011).

25. Lee, S. A. *et al*. Color Capable Sub-Pixel Resolving Optofluidic Microscope and Its Application to Blood Cell Imaging for Malaria Diagnosis. *PLoS ONE* **6,** e26127 (2011).

26. Repetto, L., Piano, E. & Pontiggia, C. Lensless digital holographic microscope with light-emitting diode illumination. *Opt. Lett.* **29,** 1132–1134 (2004).

27. Dubois, F., Joannes, L. & Legros, J.-C. Improved Three-Dimensional Imaging with a Digital Holography Microscope With a Source of Partial Spatial Coherence. *Appl. Opt.* **38,** 7085–7094 (1999).

28. Nokia Europe - Nokia 808 PureView with 41 MP camera – Specifications. *Nokia.com* Available at: http://europe.nokia.com/find-products/devices/nokia-808-pureview/specifications. (Accessed: 21st March 2012)

29. Fienup, J. R. Phase retrieval algorithms: a comparison. *Appl. Opt.* **21,** 2758–2769 (1982).

30. Denis, L., Fournier, C., Fournel, T. & Ducottet, C. Numerical suppression of the twin image in in-line holography of a volume of micro-objects. *Meas. Sci. Technol.* **19,** 074004 (2008).

31. HTC Launches Tegra-Powered One X Phone on Eve of MWC. Available at: http://blogs.nvidia.com/2012/02/htc-launches-tegra-powered-one-x-phone-on-eve-of-mwc/. (Accessed: 22nd March 2012)

32. The employed 40MP CCD imager (KODAK KAF-39000) is still cost-effective compared to a scanning optical microscopy set-up, with a cost of <5000 USD per sensor chip.

33. Coskun, A. F., Sencan, I., Su, T.-W. & Ozcan, A. Lensless wide-field fluorescent imaging on a chip using compressive decoding of sparse objects. *Opt. Express* **18,** 10510–10523 (2010).

34. Schnars, U. & Jüptner, W. P. O. Digital recording and numerical reconstruction of holograms. *Meas. Sci. Technol.* **13,** R85–R101 (2002).

35. Allen, L. J. & Oxley, M. P. Phase retrieval from series of images obtained by defocus variation. *Opt. Commun.* **199,** 65–75 (2001).

36. Coskun, A. F., Sencan, I., Su, T.-W. & Ozcan, A. Lensfree Fluorescent On-Chip Imaging of Transgenic Caenorhabditis elegans Over an Ultra-Wide Field-of-View. *PLoS ONE* **6,** e15955 (2011).

37. Coskun, A. F., Sencan, I., Su, T.-W. & Ozcan, A. Wide-field lensless fluorescent microscopy using a tapered fiber-optic faceplate on a chip. *Analyst* **136,** 3512–3518 (2011).

38. Khademhosseinieh, B. *et al.* Lensfree on-chip imaging using nanostructured surfaces. *Appl. Phys. Lett.* **96,** 171106–171106–3 (2010).

39. Xu, W. Digital in-line holography for biological applications. *Proc. Natl. Acad. Sci.* **98,** 11301–11305 (2001).

40. Maiden, A. M., Rodenburg, J. M. & Humphry, M. J. Optical ptychography: a practical implementation with useful resolution. *Opt. Lett.* **35,** 2585–2587 (2010).

41. Garcia-Sucerquia, J. Color lensless digital holographic microscopy with micrometer resolution. *Opt Lett* **37,** 1724–1726 (2012).

42. Maiden, A. M., Humphry, M. J., Zhang, F. & Rodenburg, J. M. Superresolution imaging via ptychography. *J. Opt. Soc. Am. A* **28,** 604–612 (2011).

43. Yamaguchi, I., Matsumura, T. & Kato, J. Phase-shifting color digital holography. *Opt. Lett.* **27,** 1108–1110 (2002).

44. Cuche, E., Bevilacqua, F. & Depeursinge, C. Digital holography for quantitative phase-contrast imaging. *Opt. Lett.* **24,** 291 (1999).

45. Martínez-León, L., Pedrini, G. & Osten, W. Applications of short-coherence digital holography in microscopy. *Appl. Opt.* **44,** 3977 (2005).

46. Almoro, P., Pedrini, G. & Osten, W. Complete wavefront reconstruction using sequential intensity measurements of a volume speckle field. *Appl. Opt.* **45,** 8596–8605 (2006).

47. Zheng, G., Lee, S. A., Antebi, Y., Elowitz, M. B. & Yang, C. The ePetri dish, an on-chip cell imaging platform based on subpixel perspective sweeping microscopy (SPSM). *Proc. Natl. Acad. Sci.* **108,** 16889–16894 (2011).

48. Pang, S. *et al*. Implementation of a color-capable optofluidic microscope on a RGB CMOS color sensor chip substrate. *Lab. Chip* **10,** 411–414 (2010).

49. Pang, S., Han, C., Kato, M., Sternberg, P. W. & Yang, C. Wide and scalable field-of-view Talbot-grid-based fluorescence microscopy. *Opt. Lett.* **37,** 5018 (2012).

50. Jin, G. *et al*. Lens-free shadow image based high-throughput continuous cell monitoring technique. *Biosens. Bioelectron.* **38,** 126–131 (2012).

51. Tanaka, T., Saeki, T., Sunaga, Y. & Matsunaga, T. High-content analysis of single cells directly assembled on CMOS sensor based on color imaging. *Biosens. Bioelectron.* **26,** 1460–1465 (2010).

52. Li, W., Knoll, T., Sossalla, A., Bueth, H. & Thielecke, H. On-chip integrated lensless fluorescence microscopy/spectroscopy module for cell-based sensors. in (ed. Gannot, I.) 78940Q (2011). doi:10.1117/12.875417

53. Isikman, S. O. *et al.* Lens-free optical tomographic microscope with a large imaging volume on a chip. *Proc. Natl. Acad. Sci.* **108,** 7296–7301 (2011).

54. Seo, S., Su, T.-W., Tseng, D. K., Erlinger, A. & Ozcan, A. Lensfree holographic imaging for on-chip cytometry and diagnostics. *Lab. Chip* **9,** 777–787 (2009).

55. Allier, C. P., Hiernard, G., Poher, V. & Dinten, J. M. Bacteria detection with thin wetting film lensless imaging. *Biomed. Opt. Express* **1,** 762–770 (2010).

56. Greenbaum, A. *et al.* Imaging without lenses: achievements and remaining challenges of wide-field on-chip microscopy. *Nat. Methods* **9,** 889–895 (2012).

57. Mudanyali, O. *et al.* Wide-field optical detection of nanoparticles using on-chip microscopy and self-assembled nanolenses. *Nat. Photonics* **7,** 254–254 (2013).

58. Gorocs, Z. & Ozcan, A. On-Chip Biomedical Imaging. *IEEE Rev. Biomed. Eng.* **6,** 29–46 (2013).

59. Isikman, S. O. *et al.* Lensfree On-Chip Microscopy and Tomography for Biomedical Applications. *IEEE J. Sel. Top. Quantum Electron.* **18,** 1059–1072 (2012).

60. Mudanyali, O. *et al.* Compact, light-weight and cost-effective microscope based on lensless incoherent holography for telemedicine applications. *Lab. Chip* **10,** 1417–1428 (2010).

61. Mudanyali, O., Oztoprak, C., Tseng, D., Erlinger, A. & Ozcan, A. Detection of waterborne parasites using field-portable and cost-effective lensfree microscopy. *Lab. Chip* **10,** 2419 (2010).

62. Hardie, R. C. High-resolution image reconstruction from a sequence of rotated and translated frames and its application to an infrared imaging system. *Opt. Eng.* **37,** 247 (1998).

63. Biggs, D. S. C. & Andrews, M. Acceleration of iterative image restoration algorithms. *Appl. Opt.* **36,** 1766 (1997).

64. Holmes, T. J. *et al.* in *Handbook of Biological Confocal Microscopy* (ed. Pawley, J. B.) 389–402 (Springer US, 1995).

65. Gonzalez, R. C. *Digital image processing*. (Prentice Hall, 2008).

66. Goodman, J. *Introduction to Fourier Optics*. (Roberts and Company Publishers, 2004).

67. Sung Cheol Park, Min Kyu Park & Moon Gi Kang. Super-resolution image reconstruction: a technical overview. *IEEE Signal Process. Mag.* **20,** 21– 36 (2003).

68. Elad, M. & Hel-Or, Y. A fast super-resolution reconstruction algorithm for pure translational motion and common space-invariant blur. *IEEE Trans. Image Process.* **10,** 1187–1193 (2001).

69. Elad, M. & Hel-Or, Y. A fast super-resolution reconstruction algorithm for pure translational motion and common space-invariant blur. *IEEE Trans. Image Process.* **10,** 1187–1193 (2001).

70. Farsiu, S., Elad, M. & Milanfar, P. Multiframe demosaicing and super-resolution of color images. *IEEE Trans. Image Process.* **15,** 141–159 (2006).

71. Isikman, S. O., Greenbaum, A., Luo, W., Coskun, A. F. & Ozcan, A. Giga-Pixel Lensfree Holographic Microscopy and Tomography Using Color Image Sensors. *PLoS ONE* **7,** e45044 (2012).

72. Greenbaum, A. & Ozcan, A. Maskless imaging of dense samples using pixel super-resolution based multi-height lensfree on-chip microscopy. *Opt Express* **20,** 3129–3143 (2012).

73. Greenbaum, A., Sikora, U. & Ozcan, A. Field-portable wide-field microscopy of dense samples using multi-height pixel super-resolution based lensfree imaging. *Lab. Chip* **12,** 1242–1245 (2012).

74. Pawley, J. B. *Handbook of Biological Confocal Microscopy*. (Springer US, 1995).

75. Holmes, T. J. Blind deconvolution of quantum-limited incoherent imagery: maximum-likelihood approach. *J. Opt. Soc. Am. A* **9,** 1052 (1992).

76. Levin, A., Weiss, Y., Durand, F. & Freeman, W. T. Understanding and evaluating blind deconvolution algorithms. in 1964–1971 (IEEE, 2009). doi:10.1109/CVPR.2009.5206815

77. Meisenzahl, E. J. *et al*. 31 Mp and 39 Mp full-frame CCD image sensors with improved charge capacity and angle response. in (eds. Sampat, N., DiCarlo, J. M. & Martin, R. A.) 606902–606902–9 (2006). doi:10.1117/12.651672

78. Meisenzahl, E. J. *et al*. 3.2-million-pixel full-frame true 2-phase CCD image sensor incorporating transparent gate technology. in (eds. Blouke, M. M., Sampat, N., Williams, Jr., G. M. & Yeh, T.) 92–100 (2000). doi:10.1117/12.385464

79. Fontaine, R. Recent innovations in CMOS image sensors. in 1–5 (IEEE, 2011). doi:10.1109/ASMC.2011.5898219

80. Brady, D. J. & Optical Society of America. *Optical imaging and spectroscopy*. (Wiley ; Optical Society of America, 2009).

81. Javidi, B. *et al*. Three-dimensional image fusion by use of multiwavelength digital holography. *Opt. Lett.* **30,** 144–146 (2005).

82. Ferraro, P. *et al*. Full Color 3-D Imaging by Digital Holography and Removal of Chromatic Aberrations. *J. Disp. Technol.* **4,** 97–100 (2008).

83. Rosen, J. & Brooker, G. Non-scanning motionless fluorescence three-dimensional holographic microscopy. *Nat. Photonics* **2,** 190–195 (2008).

84. Choi, K. *et al*. Compressive holography of diffuse objects. *Appl. Opt.* **49,** H1–H10 (2010).

85. Paturzo, M., Merola, F. & Ferraro, P. Multi-imaging capabilities of a 2D diffraction grating in combination with digital holography. *Opt. Lett.* **35,** 1010–1012 (2010).

86. Hahn, J., Lim, S., Choi, K., Horisaki, R. & Brady, D. J. Video-rate compressive holographic microscopic tomography. *Opt. Express* **19,** 7289–7298 (2011).

87. Memmolo, P. *et al*. On the holographic 3D tracking of in vitro cells characterized by a highly-morphological change. *Opt. Express* **20,** 28485–28493 (2012).

88. Zhu, H., Mavandadi, S., Coskun, A. F., Yaglidere, O. & Ozcan, A. Optofluidic Fluorescent Imaging Cytometry on a Cell Phone. *Anal. Chem.* 110802145633047 (2011). doi:10.1021/ac201587a

89. Su, T.-W., Xue, L. & Ozcan, A. High-throughput lensfree 3D tracking of human sperms reveals rare statistics of helical trajectories. *Proc. Natl. Acad. Sci.* **109,** 16018–16022 (2012).

90. Isikman, S. O. *et al*. Lens-free optical tomographic microscope with a large imaging volume on a chip. *Proc. Natl. Acad. Sci.* **108,** 7296–7301 (2011).

91. Khademhosseinieh, B. *et al*. Lensfree sensing on a microfluidic chip using plasmonic nanoapertures. *Appl*. *Phys*. *Lett*. **97,** 221107 (2010).

92. Coskun, A. F., Sencan, I., Su, T.-W. & Ozcan, A. Lensless wide-field fluorescent imaging on a chip using compressive decoding of sparse objects. *Opt*. *Express* **18,** 10510–10523 (2010).

93. Zheng, G., Lee, S. A., Antebi, Y., Elowitz, M. B. & Yang, C. The ePetri dish, an on-chip cell imaging platform based on subpixel perspective sweeping microscopy (SPSM). *Proc*. *Natl*. *Acad*. *Sci*. (2011). doi:10.1073/pnas.1110681108

94. Bishara, W. *et al*. Holographic pixel super-resolution in portable lensless on-chip microscopy using a fiber-optic array. *Lab*. *Chip* **11,** 1276 (2011).

95. Isikman, S. O. *et al*. Field-portable lensfree tomographic microscope. *Lab*. *Chip* **11,** 2222–2230 (2011).

96. Greenbaum, A., Sikora, U. & Ozcan, A. Field-portable wide-field microscopy of dense samples using multi-height pixel super-resolution based lensfree imaging. *Lab*. *Chip* **12,** 1242 (2012).

97. Bishara, W., Su, T.-W., Coskun, A. F. & Ozcan, A. Lensfree on-chip microscopy over a wide field-of-view using pixel super-resolution. *Opt*. *Express* **18,** 11181 (2010).

98. Greenbaum, A. *et al*. Increased space-bandwidth product in pixel super-resolved lensfree on-chip microscopy. *Sci*. *Rep*. **3,** (2013).

99. McLeod, E., Luo, W., Mudanyali, O., Greenbaum, A. & Ozcan, A. Toward giga-pixel nanoscopy on a chip: a computational wide-field look at the nano-scale without the use of lenses. *Lab*. *Chip* **13,** 2028–2035 (2013).

100. Fienup, J. R. Reconstruction of an object from the modulus of its Fourier transform. *Opt. Lett.* **3,** 27–29 (1978).

101. Fienup, J. R. Phase retrieval algorithms: a comparison. *Appl. Opt.* **21,** 2758–2769 (1982).

102. Allen, L. J. & Oxley, M. P. Phase retrieval from series of images obtained by defocus variation. *Opt. Commun.* **199,** 65–75 (2001).

103. Zhang, Y., Pedrini, G., Osten, W. & Tiziani, H. Whole optical wave field reconstruction from double or multi in-line holograms by phase retrieval algorithm. *Opt. Express* **11,** 3234–3241 (2003).

104. Kanka, M., Riesenberg, R., Petruck, P. & Graulig, C. High resolution (NA=0.8) in lensless in-line holographic microscopy with glass sample carriers. *Opt. Lett.* **36,** 3651–3653 (2011).

105. Schwarz, C. J., Kuznetsova, Y. & Brueck, S. R. J. Imaging interferometric microscopy. *Opt. Lett.* **28,** 1424–1426 (2003).

106. Mico, V., Zalevsky, Z., Garcia-Martinez, P. & Garcia, J. Single-step superresolution by interferometric imaging. *Opt. Express* **12,** 2589–2596 (2004).

107. Alexandrov, S., Hillman, T., Gutzler, T. & Sampson, D. Synthetic Aperture Fourier Holographic Optical Microscopy. *Phys. Rev. Lett.* **97,** 168102 (2006).

108. Mico, V., Zalevsky, Z. & García, J. Superresolution optical system by common-path interferometry. *Opt. Express* **14,** 5168–5177 (2006).

109. Mico, V., Zalevsky, Z., García-Martínez, P. & García, J. Superresolved imaging in digital holography by superposition of tilted wavefronts. *Appl. Opt.* **45,** 822–828 (2006).

110. Mico, V., Zalevsky, Z., García-Martínez, P. & García, J. Synthetic aperture superresolution with multiple off-axis holograms. *J. Opt. Soc. Am. A* **23,** 3162–3170 (2006).

111. Ralston, T. S., Marks, D. L., Scott Carney, P. & Boppart, S. A. Interferometric synthetic aperture microscopy. *Nat. Phys.* **3,** 129–134 (2007).

112. Martínez-León, L. & Javidi, B. Synthetic aperture single-exposure on-axis digital holography. *Opt. Express* **16,** 161–169 (2008).

113. Granero, L., Micó, V., Zalevsky, Z. & García, J. Synthetic aperture superresolved microscopy in digital lensless Fourier holography by time and angular multiplexing of the object information. *Appl. Opt.* **49,** 845–857 (2010).

114. Micó, V. & Zalevsky, Z. Superresolved digital in-line holographic microscopy for high-resolution lensless biological imaging. *J. Biomed. Opt.* **15,** 046027–046027–5 (2010).

115. Rodrigo, J. A., Alieva, T., Cristóbal, G. & Calvo, M. L. Wavefield imaging via iterative retrieval based on phase modulation diversity. *Opt. Express* **19,** 18621–18635 (2011).

116. Tippie, A. E., Kumar, A. & Fienup, J. R. High-resolution synthetic-aperture digital holography with digital phase and pupil correction. *Opt. Express* **19,** 12027–12038 (2011).

117. Pelagotti, A. *et al.* An automatic method for assembling a large synthetic aperture digital hologram. *Opt. Express* **20,** 4830–4839 (2012).

118. Zheng, G., Horstmeyer, R. & Yang, C. Wide-field, high-resolution Fourier ptychographic microscopy. *Nat. Photonics* (2013). doi:10.1038/nphoton.2013.187

119. Tian, L., Li, X., Ramchandran, K. & Waller, L. Multiplexed coded illumination for Fourier Ptychography with an LED array microscope. *Biomed. Opt. Express* **5,** 2376–2389 (2014).

120. Fienup, J. R. Reconstruction of a complex-valued object from the modulus of its Fourier transform using a support constraint. *J. Opt. Soc. Am. A* **4,** 118–123 (1987).

121. Sung Cheol Park, Min Kyu Park & Moon Gi Kang. Super-resolution image reconstruction: a technical overview. *IEEE Signal Process. Mag.* **20,** 21–36 (2003).

122. Pech-Pacheco, J. L., Cristobal, G., Chamorro-Martinez, J. & Fernandez-Valdivia, J. Diatom autofocusing in brightfield microscopy: a comparative study. in *15 Th International Conference On Pattern Recognition* **3,** 314–317 (IEEE Comput. Soc, 2000).

123. Levin, A., Lischinski, D. & Weiss, Y. Colorization using optimization. *ACM Trans. Graph.* **23,** 689–694 (2004).

124. Gonzalez, R. C. *Digital image processing*. (Prentice Hall, 2008).

125. Zernike, F. Phase contrast, a new method for the microscopic observation of transparent objects. *Physica* **9,** 686–698 (1942).

126. Chen, T., Catrysse, P. B., El Gamal, A. & Wandell, B. A. How small should pixel size be? *Proc. SPIE* **3965,** 451–459 (2000).

127. Tsai, R. Y. & Huang, T. S. Multiframe Image Restoration and Registration. *Adv. Comput. Vis. Image Process.* **1,** 317–339 (1984).

128. Greenbaum, A. & Ozcan, A. Maskless imaging of dense samples using pixel super-resolution based multi-height lensfree on-chip microscopy. *Opt. Express* **20,** 3129 (2012).

129. Greenbaum, A. *et al.* Wide-field computational imaging of pathology slides using lens-free on-chip microscopy. *Sci. Transl. Med.* **6,** 267ra175–267ra175 (2014).

130. Luo, W., Greenbaum, A., Zhang, Y. & Ozcan, A. Synthetic aperture-based on-chip microscopy. *Light Sci. Appl.* **4,** e261 (2015).

131. Celebi, M. E. & Schaefer, G. *Color Medical Image Analysis*. (Springer, 2013).

132. Yamaguchi, I., Matsumura, T. & Kato, J. Phase-shifting color digital holography. *Opt. Lett.* **27,** 1108 (2002).

133. Kato, J., Yamaguchi, I. & Matsumura, T. Multicolor digital holography with an achromatic phase shifter. *Opt. Lett.* **27,** 1403–1405 (2002).

134. Picart, P., Tankam, P., Mounier, D., Peng, Z. & Li, J. Spatial bandwidth extended reconstruction for digital color Fresnel holograms. *Opt. Express* **17,** 9145–9156 (2009).

135. Kakue, T. *et al*. Parallel phase-shifting color digital holography using two phase shifts. *Appl. Opt.* **48,** H244–H250 (2009).

136. Isikman, S. O. *et al*. Color and monochrome lensless on-chip imaging of Caenorhabditis elegans over a wide field-of-view. *Lab. Chip* **10,** 1109 (2010).

137. Garcia-Sucerquia, J. Color lensless digital holographic microscopy with micrometer resolution. *Opt. Lett.* **37,** 1724–1726 (2012).

138. Ito, Y. *et al*. Four-Wavelength Color Digital Holography. *J. Disp. Technol.* **8,** 570–576 (2012).

139. Greenbaum, A., Feizi, A., Akbari, N. & Ozcan, A. Wide-field computational color imaging using pixel super-resolved on-chip microscopy. *Opt. Express* **21,** 12469–12483 (2013).

140. Mendoza-Yero, O., Tajahuerce, E., Lancis, J. & Garcia-Sucerquia, J. Diffractive digital lensless holographic microscopy with fine spectral tuning. *Opt. Lett.* **38,** 2107–2109 (2013).

141. Kiss, M. Z. *et al*. Special multicolor illumination and numerical tilt correction in volumetric digital holographic microscopy. *Opt. Express* **22,** 7559–7573 (2014).

142. Dohet-Eraly, J., Yourassowsky, C. & Dubois, F. Color imaging-in-flow by digital holographic microscopy with permanent defect and aberration corrections. *Opt. Lett.* **39,** 6070–6073 (2014).

143. Bao, P., Zhang, F., Pedrini, G. & Osten, W. Phase retrieval using multiple illumination wavelengths. *Opt. Lett.* **33,** 309–311 (2008).

144. Bao, P., Situ, G., Pedrini, G. & Osten, W. Lensless phase microscopy using phase retrieval with multiple illumination wavelengths. *Appl. Opt.* **51,** 5486 (2012).

145. Noom, D. W. E., Boonzajer Flaes, D. E., Labordus, E., Eikema, K. S. E. & Witte, S. High-speed multi-wavelength Fresnel diffraction imaging. *Opt. Express* **22,** 30504 (2014).

146. Sanz, M., Picazo-Bueno, J. A., García, J. & Micó, V. Improved quantitative phase imaging in lensless microscopy by single-shot multi-wavelength illumination using a fast convergence algorithm. *Opt. Express* **23,** 21352–21365 (2015).

147. Kazemzadeh, F. *et al*. Lens-free spectral light-field fusion microscopy for contrast- and resolution-enhanced imaging of biological specimens. *Opt. Lett*. **40,** 3862 (2015).

148. Kühn, J. *et al*. Real-time dual-wavelength digital holographic microscopy with a single hologram acquisition. *Opt. Express* **15,** 7231–7242 (2007).

149. Desse, J.-M., Picart, P. & Tankam, P. Digital three-color holographic interferometry for flow analysis. *Opt. Express* **16,** 5471 (2008).

150. Khmaladze, A., Kim, M. & Lo, C.-M. Phase imaging of cells by simultaneous dual-wavelength reflection digital holography. *Opt. Express* **16,** 10900–10911 (2008).

151. Itoh, K. Analysis of the phase unwrapping algorithm. *Appl. Opt*. **21,** 2470 (1982).

152. Takeda, M., Gu, Q., Kinoshita, M., Takai, H. & Takahashi, Y. Frequency-multiplex Fourier-transform profilometry: a single-shot three-dimensional shape measurement of objects with large height discontinuities and/or surface isolations. *Appl. Opt*. **36,** 5347 (1997).

153. Costantini, M. A novel phase unwrapping method based on network programming. *IEEE Trans. Geosci. Remote Sens*. **36,** 813–821 (1998).

154. Volkov, V. V. & Zhu, Y. Deterministic phase unwrapping in the presence of noise. *Opt. Lett*. **28,** 2156 (2003).

155. Shen, P. F. & Patterson, L. T. A Simplified Wright's Stain Technique for Routine Avian Blood Smear Staining. *Poult. Sci.* **62,** 923–924 (1983).

156. Oppenheim, A. V., Willsky, A. S. & Nawab, S. H. *Signals and systems*. (Prentice Hall, 1997).

157. Allen, L. J., McBride, W., O'Leary, N. L. & Oxley, M. P. Exit wave reconstruction at atomic resolution. *Ultramicroscopy* **100,** 91–104 (2004).

158. Boyd, S. P. & Vandenberghe, L. *Convex optimization*. (Cambridge University Press, 2004).

159. Gass, J., Dakoff, A. & Kim, M. K. Phase imaging without 2π ambiguity by multiwavelength digital holography. *Opt. Lett.* **28,** 1141 (2003).

160. Gabor, D. A New Microscopic Principle. *Nature* **161,** 777–778 (1948).

161. Ozcan, A. Mobile phones democratize and cultivate next-generation imaging, diagnostics and measurement tools. *Lab Chip* **14,** 3187–3194 (2014).

162. Garcia-Sucerquia, J. *et al*. Digital in-line holographic microscopy. *Appl. Opt.* **45,** 836–850 (2006).

163. Stern, A. & Javidi, B. Theoretical analysis of three-dimensional imaging and recognition of micro-organisms with a single-exposure on-line holographic microscope. *JOSA A* **24,** 163–168 (2007).

164. Ferraro, P. *et al*. Full Color 3-D Imaging by Digital Holography and Removal of Chromatic Aberrations. *J. Disp. Technol.* **4,** 97–100 (2008).

165. Martínez-León, L. & Javidi, B. Synthetic aperture single-exposure on-axis digital holography. *Opt. Express* **16,** 161–169 (2008).

166. Kanka, M., Riesenberg, R. & Kreuzer, H. J. Reconstruction of high-resolution holographic microscopic images. *Opt. Lett.* **34,** 1162–1164 (2009).

167. Brady, D. J., Choi, K., Marks, D. L., Horisaki, R. & Lim, S. Compressive Holography. *Opt. Express* **17,** 13040–13049 (2009).

168. Rosen, J. & Brooker, G. Non-scanning motionless fluorescence three-dimensional holographic microscopy. *Nat. Photonics* **2,** 190–195 (2008).

169. Barsi, C., Wan, W. & Fleischer, J. W. Imaging through nonlinear media using digital holography. *Nat. Photonics* **3,** 211–215 (2009).

170. Rivenson, Y., Stern, A. & Javidi, B. Compressive Fresnel Holography. *J. Disp. Technol.* **6,** 506–509 (2010).

171. Xu, Q. *et al*. Inline holographic coherent anti-Stokes Raman microscopy. *Opt. Express* **18,** 8213–8219 (2010).

172. Waller, L., Tian, L. & Barbastathis, G. Transport of Intensity imaging with higher order derivatives. *Opt. Express* **18,** 12552 (2010).

173. Shaked, N. T., Newpher, T. M., Ehlers, M. D. & Wax, A. Parallel on-axis holographic phase microscopy of biological cells and unicellular microorganism dynamics. *Appl. Opt.* **49,** 2872–2878 (2010).

174. Wang, Z. *et al*. Spatial light interference microscopy (SLIM). *Opt. Express* **19,** 1016–1026 (2011).

175. Hahn, J., Lim, S., Choi, K., Horisaki, R. & Brady, D. J. Video-rate compressive holographic microscopic tomography. *Opt. Express* **19,** 7289–7298 (2011).

176. Hahn, J., Marks, D. L., Choi, K., Lim, S. & Brady, D. J. Thin holographic camera with integrated reference distribution. *Appl. Opt.* **50,** 4848–4854 (2011).

177. Waller, L., Tsang, M., Ponda, S., Yang, S. Y. & Barbastathis, G. Phase and amplitude imaging from noisy images by Kalman filtering. *Opt. Express* **19,** 2805–2815 (2011).

178. Pelagotti, A. *et al*. An automatic method for assembling a large synthetic aperture digital hologram. *Opt. Express* **20,** 4830–4839 (2012).

179. Liu, Y. *et al*. Scanning-free compressive holography for object localization with subpixel accuracy. *Opt. Lett*. **37,** 3357–3359 (2012).

180. Barsi, C. & Fleischer, J. W. Nonlinear Abbe theory. *Nat. Photonics* **7,** 639–643 (2013).

181. Rivenson, Y., Stern, A. & Javidi, B. Overview of compressive sensing techniques applied in holography [Invited]. *Appl. Opt*. **52,** A423–A432 (2013).

182. Luo, W., Greenbaum, A., Zhang, Y. & Ozcan, A. Synthetic aperture-based on-chip microscopy. *Light Sci. Appl*. **4,** e261 (2015).

183. McLeod, E. *et al*. High-Throughput and Label-Free Single Nanoparticle Sizing Based on Time-Resolved On-Chip Microscopy. *ACS Nano* **9,** 3265–3273 (2015).

184. Luo, W. *et al*. Pixel super-resolution using wavelength scanning. *Light Sci. Appl*. (2015). doi:10.1038/lsa.2016.60

185. Allen, L. J. & Oxley, M. P. Phase retrieval from series of images obtained by defocus variation. *Opt. Commun*. **199,** 65–75 (2001).

186. Zhang, Y., Pedrini, G., Osten, W. & Tiziani, H. Whole optical wave field reconstruction from double or multi in-line holograms by phase retrieval algorithm. *Opt. Express* **11,** 3234–3241 (2003).

187. Cañas, A. Advances in Computer Vision and Image Processing.Volume 1, 1984, Image Reconstruction from Incomplete Observations. *Opt. Acta Int. J. Opt*. **33,** 685–685 (1986).

188. Bao, P., Zhang, F., Pedrini, G. & Osten, W. Phase retrieval using multiple illumination wavelengths. *Opt. Lett*. **33,** 309–311 (2008).

189. Bao, P., Situ, G., Pedrini, G. & Osten, W. Lensless phase microscopy using phase retrieval with multiple illumination wavelengths. *Appl. Opt.* **51,** 5486–5494 (2012).

190. Greenbaum, A. *et al.* Imaging without lenses: achievements and remaining challenges of wide-field on-chip microscopy. *Nat. Methods* **9,** 889–895 (2012).

191. Min, J. *et al.* Phase retrieval without unwrapping by single-shot dual-wavelength digital holography. *J. Opt.* **16,** 125409 (2014).